Tesis Doctoral

Fenómenos cinéticos de plasma en el medio interplanetario

Andrés, Nahuel

2015-11-30

UNIVERSIDAD DE BUENOS AIRES

Facultad de Ciencias Exactas y Naturales

Departamento de Física

Fenómenos cinéticos de plasma en el medio interplanetario

Tesis presentada para optar al título de Doctor de la Universidad de Buenos Aires en el área de Física

Nahuel Andrés

Directores de Tesis:

Daniel Gómez y Cesar Bertucci

Consejero de Estudios: Pablo Minnini

Lugar de trabajo: Instituto de Astronomía y Física del Espacio, UBA-CONICET.

Ciudad Autónoma de Buenos Aires, 2015

Resumen

Si bien la dinámica macroscópica de los plasmas en el medio interplanetario se estudia adecuadamente a través de una descripción magnetohidrodinámica (MHD), a escalas más pequeñas comienzan a manifestarse efectos cinéticos que producen consecuencias observables. La presente Tesis propone investigar y entender algunos fenómenos físicos que requieren apartarse de la descripción MHD tradicional, tales como el efecto Hall y la inercia electrónica. En particular, se estudiará la generación y distribución de ondas de ultra-baja frecuencia asociadas a las magnetosferas planetarias, la importancia de la inercia electrónica en procesos de reconexión magnética no-colisional y el estudio del espectro de energía electromagnética en las pequeñas escalas en el viento solar. El estudio teórico-numérico de estos fenómenos se complementará con el análisis de mediciones in-situ de satélites orbitando alrededor de planetas con campo magnético intrínseco, como la Tierra o Saturno.

Palabras claves: magnetohidrodinámica, efectos cinéticos, turbulencia, reconexión magnética, ondas de ultra-baja frequencia

Plasma kinetic effects in the interplanetary medium

Abstract

The one-fluid magnetohydrodynamics (MHD) describes space plasma phenomena at macroscopic temporal and spatial scales. However, this description is no adequate when small-scale processes become significant. In this Thesis, we theoretically describe small-scale plasma processes observed in different regions of the interplanetary medium. In particular, we focus our attention on the turbulent nature of the solar wind, collisionless magnetic reconnection, and the generation and distribution of ultra-low frequency waves in planetary foreshocks. The theoretical and numerical study will be complemented with the analysis of in-situ measurements provided by Cassini and Cluster spacecrafts.

Keywords: magnetohydrodynamics, kinetic effects, turbulence, magnetic reconnection, ultra-low frequency waves

Agradecimientos

En primer lugar, al sistema de educación pública, el cual me ha formado desde los tres años. A la Universidad de Buenos Aires y al Consejo Nacional de Investigaciones Científicas y Técnicas. En particular, agradezco al Instituto de Astronomía y Física del Espacio, y al Departamento de Física de la Facultad de Ciencias Exactas y Naturales. A la vez, agradezco al Estado Argentino por sostener estas instituciones.

En segundo lugar, a Daniel, quien me ha formado, guiado y acompañado durante todo el Doctorado. Nunca se desmotivó (totalmente...) y siempre estuvo cuando lo necesité. Agradezco mucho su buena predisposición y seriedad a la hora de trabajar, así como también su buen humor a la hora de distenderse.

En tercer lugar, a Cesar, quien me ha acompañado con charlas, consejos y recomendaciones en cada etapa del Doctorado. Su experiencia y puntos de vista me han permitido formarme y aprender mucho de él.

En cuarto lugar, al Grupo de Flujos Astrofísicos. La dinámica grupal y cada uno de sus integrantes me han permitido aprender y formar una visión crítica de lo que es hacer ciencia. Una mención especial para Pablo Mininni y Pablo Dmitruk, quienes me han formado y aconsejado extensamente lo largo de estos años.

En quinto lugar, a mi familia y amigos, quienes han estado a mi lado y me han ayudado inmensamente en cada instante. Sería un error dar nombres, por las razón más evidente: de manera irremediable olvidaré algún nombre. Cada uno de ellos sabrán cuan agradecido le estoy.

Finalmente, a Valeria. Mi compañera *siempre*.

Nahuel Andrés.

Ciudad Autónoma de Buenos Aires, Septiembre 2015.

A mis hermanos...

Contents

List of Figures

List of Tables

Chapter 1

Introduction

The electron is a theory we use;
it is so useful in understanding the way
nature works that we can almost call it real.
Surely you're joking, Mr. Feynman! Richard P. Feynman

1.1 Interplanetary medium

The interplanetary medium fills the space between planets, comets and other objects of the solar system. Far from being empty, this space is filled with plasma from the solar corona, electromagnetic radiation, cosmic rays, dust particles and magnetic fields. The term *solar wind* was coined by Eugene Parker [Parker, 1958] to describe this supersonic (and supermagnetosonic) expansion of the solar corona into the solar system. This expansion is a consequence of a pressure difference between the solar corona and the interplanetary space that surrounds it. The pressure difference drives the solar wind outward from the solar corona, despite of the solar gravity influence [e.g. Kivelson and Russell, 1995].

The dynamics of space plasmas such as the solar wind, can display huge differences in their physical properties with respect to the plasmas present in the laboratory. For instance, collisions between ions or electrons can be quite frequent in the solar coronal plasma, but are extremely rare in the interplanetary medium at 1 astronomical unit (1 AU = 1.49×10^{11} m). Since some of these conditions can be impossible to reproduce in terrestrial laboratories, the interplanetary medium offers a unique opportunity to investigate a wide variety of plasma process. In particular, at 1 AU the mean number density is 7 cm^{-3}, the flow speed (nearly radial) is 450 km/s, the mean temperature is 1.2×10^5 K and the mean magnetic field (absolute value) is about 10 nT [values extracted from Kivelson and Russell, 1995].

The solar wind is significantly modified by the activity of the Sun through changes in the solar magnetic field, that end up contributing to the interplanetary magnetic field (IMF) and plasma overall dynamics. During its expansion, the solar wind develops a strongly turbulent regime, which can be studied through in-situ measurements [Matthaeus and Goldstein, 1982]. Turbulence appears as a very complex state of motion, and strongly irregular in space and time. However, at any given time, a turbulent flow shows the presence of organized structures of different sizes and different lifetimes which interact among themselves as they are convected by the flow. Thanks to the in-situ observations provided by different spacecrafts, the solar wind flow offers the best opportunity to study directly the non-linear dynamics in space plasmas [e.g. Bruno and Carbone, 2013].

The plasma of the solar wind is threaded with the interplanetary magnetic field lines. When the solar wind encounters the Earth's intrinsic magnetic field, under some particular IMF conditions, the magnetic reconnection process can take place [Dungey, 1961]. Magnetic reconnection involves a topology change of a set of field lines, while converts magnetic free energy into heat and kinetic energy. Magnetic

reconnection can occur in a variety of scenarios, from the evolution of solar flares, coronal mass ejections to the formation of stars [Biskamp, 2000, Priest and Forbes, 2000].

When the supersonic and supermagnetosonic solar wind plasma encounters an obstacle such as a planetary magnetosphere, a bow shock is formed. The bow shock slows down the incoming solar wind plasma from supersonic to subsonic velocity in order that information about the obstacle can propagate upstream within the shocked region and let the plasma adjust and flow around it [Thomsen et al., 1983]. Upstream from the shock, however, the solar wind is unaware that it is approaching to an obstacle. The region upstream from the shock and magnetically connected to it, is known as the foreshock. At the bow shock, a small fraction of the solar wind particles are accelerated and propagate backstreaming into the upstream foreshock region. These backstreaming particles can drive a number of plasma instabilities, leading to the generation of ultra low-frequency (ULF) waves, which are detected by spacecrafts [e.g. Tsurutani and Rodriguez, 1981].

These three outcomes from the solar wind dynamics, i.e. its turbulent regime, the magnetic reconnection process and the generation and spatial distribution of ULF waves, are the main subject of the present Thesis.

1.2 Space plasmas

Space plasmas are quasi-neutral gases composed mostly of protons and electrons (i.e. a fully ionized hydrogen plasma) which are subjected to electric, magnetic and probably other types of forces. At the same time, these free charges act as sources for electric and magnetic forces. Due to the long-range nature of the electromagnetic forces, each charged particle in the plasma interacts simultaneously

with a large number of other charged particles. This process results in a collective behavior of the plasma.

There are at least three levels of description to model the dynamics of space plasmas. The main difference between them are the physical variables used to describe the state of the plasma. Which one is to be chosen depends on the kind of phenomenon one is interested in. The three approaches are:

(1) The motion of individual charged particles and their interaction with electric and magnetic field.

(2) The kinetic description of a collection of particles.

(3) The fluid description.

The most comprehensive way to specify the state of a plasma, is to give the positions and velocities of all the particles and the value of the fields at each point in space. For a system of N particles, this particle description implies a phase space of $6N$ dimensions, which becomes prohibitively large as N is increased (for instance, $N \sim 10^{15}$ for a cube of 1 km^3 in the interplanetary medium!). One possible way-out to this problem, is to use kinetic theory. In this statistical approach, we define the velocity distribution function $f_s(\mathbf{x}, \mathbf{v}, t)$, for each species s, so that $d^3\mathrm{x}d^3\mathrm{v}f_s(\mathbf{x}, \mathbf{v}, t)$ is the number of particles in the d^3x around $\mathbf{x}$, within velocities d^3v around $\mathbf{v}$ at time t. The distribution functions f_s satisfy kinetic equations such as the Vlasov equation (in the collisionless limit). These equations couple with Maxwell's equations because of the self-consistent electric and magnetic fields. Even though it is possible to integrate this set of equations numerically, to be able to cover a realistic range of values of $(\mathbf{x}, \mathbf{v}, t)$ becomes computationally very demanding. A comparatively simpler approach is to consider a fluid description for the plasma based on the lower moments of f_s (such as the particle density,

the bulk velocity of the flow and its pressure). To consider the fact that the charged particles interact with the electric and magnetic fields, causes the fluid equations to couple with Maxwell's equations. Within this framework, the simplest approximation is the so-called one-fluid magnetohydrodynamics (MHD) model.

The one-fluid MHD description adequately describes phenomena at large temporal and spatial scales (see Chapter 2). However, at spatial and/or temporal scales that are becoming accessible to current spatial instruments, there are physical phenomena that cannot be reproduced with the traditional one-fluid MHD description. For instance, to adequately describe the solar wind energy spectrum derived from recent observations [Sahraoui et al., 2009], or to study magnetic reconnection in the collisionless limit, a theoretical framework extending beyond one-fluid MHD is required. Throughout this Thesis we show how some kinetic effects can be incorporated in a theoretical description of the interplanetary medium, using a multi-fluid approach.

More specifically we focused on three main problems where kinetic effects play a role, as sketched in Figure 1.1. The solar wind is characterized by a very large Reynolds number, which is the ratio of the convective to the viscous term in the equation of motion. This high Reynolds number explain to some extent it turbulent nature. Therefore, we first focus our attention on the turbulent nature of the solar wind. Turbulent features can be recognized in natural turbulent systems like, for example, water flows on the ocean, the atmosphere of Jupiter or magnetic field fluctuations in the solar wind. A common aspect of all these flows are their extremely large Reynolds numbers. Our first task is to study (both theoretically and numerically) the solar wind turbulence and the implications of kinetic effects added through a full two-fluid MHD description. The results will be compared with in-situ solar wind measurements.

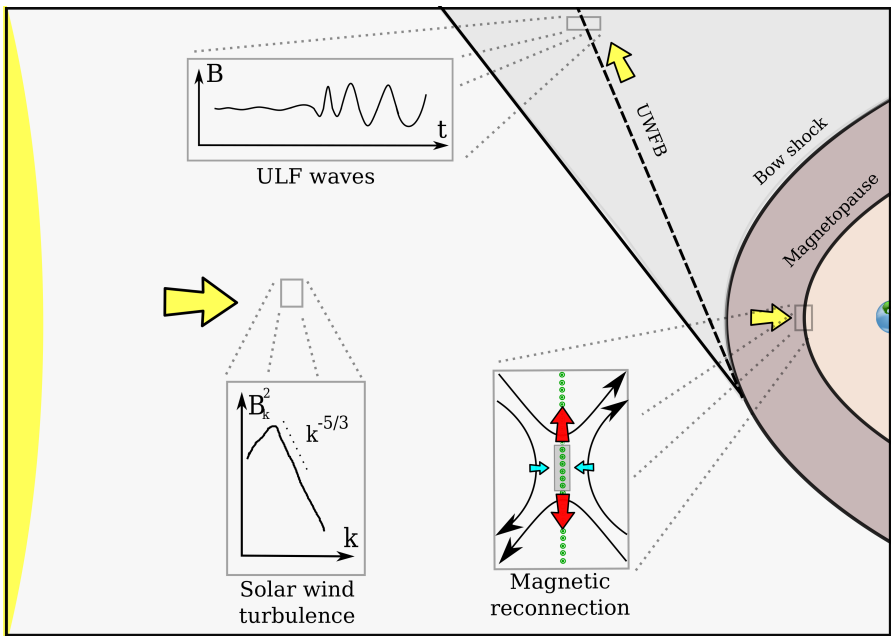

FIGURE 1.1: Three main problems where kinetic effects play a role: the solar wind turbulence, the collisionless magnetic reconnection process and the generation of ULF waves.

The second task is to address collisionless magnetic reconnection, which is present in various space physics environments such as planetary magnetospheres [e.g. Dungey, 2000]. The idea that collisionless magnetic reconnection is present in the Earth's magnetosphere was first introduced by Dungey [1961]. In Dungey's model, magnetic reconnection occurs at the day-side magnetopause and also at the magnetotail. Empirical evidence of magnetic reconnection in the magnetosphere can be found elsewhere [e.g. Yamada, 2011]. The first theoretical model of magnetic reconnection was developed within the framework of resistive one-fluid MHD [Sweet, 1958, Parker, 1957]. However, this resistive model leads to exceedingly low reconnection rates [Petschek, 1964, Edwards et al., 1986, Bhattacharjee, 2004]. In this Thesis we show that when electron-inertia effects become more important than collisions, a fast reconnection regime (driven by electron inertia) becomes possible. Moreover, we show that this collisionless magnetic reconnection can be studied within the framework of a full two-fluid MHD description.

Our third task, is to investigate the generation and distribution of ULF waves

in the foreshock of planetary magnetospheres. As mentioned, the ULF waves observed in the foreshocks of magnetized planets, cannot be described within the framework of one-fluid MHD. Even though the ULF waves can be regarded as normal modes of two-fluid MHD (the two fluids being the solar wind electrons and protons), we show that three-fluid description is needed to produce the instability (we model the backstreaming ion beam as the third fluid) from which they grow. Furthermore, we also investigate the ULF wave activity and their spatial distribution in both the Earth's and Saturn's foreshocks using in-situ measurements from Cluster and Cassini spacecraft missions, respectively.

In summary, the topics treated in this Thesis can be divided into three parts. In the first one, we study the turbulent character of the solar wind. When the solar wind magnetic field lines impact the relatively stationary dipole of the Earth, a collisionless magnetic reconnection process might take place depending the orientation of the IMF. This mechanism is the subject of the second part of the Thesis. In the third and last part, we study the spatial location of ULF waves both in Saturn's and the Earth's foreshocks, using in-situ data gathered by the Cassini and Cluster missions, respectively. This part of our work is expected to shed light on the acceleration mechanisms (present at planetary bow shocks) that generate the backstreaming ions responsible for the wave instabilities. In the next 3 sections of this Chapter we briefly introduce to each of these different plasma processes.

1.3 Solar wind turbulence

Nature routinely produces MHD turbulence. It can be found in several space environments, like the solar corona, planetary atmospheres or the interplanetary medium. As we discussed previously, the solar wind expands from the Sun and pervades the regions between planets. An important feature to characterize a

stationary and isotropic turbulent regime of a plasma is its energy power spectrum E_k, which provides the energy per unit wavenumber. Just as for the paradigmatic case of hydrodynamic turbulence, the nonlinear interactions in MHD turbulence produce an energy flow in wavenumber space that is predominantly from large scales to small-scales. As it is indicated schematically in Figure 1.2, the energy spectrum can be divided into three ranges: (a) the large-scale in which the energy is injected into the system (or energy containing) range, (b) an inertial range where the nonlinear terms dominate over the dissipative terms and energy cascades from large to small scales, and (c) the small-scale (or dissipative) range, where the energy being cascaded from the larger scales is converted into heat. Since the total energy (and other ideal invariants as well) is not directly modified by the nonlinear interactions [e.g. Frisch, 1995], its spectrum gives important information about the state and dynamics of the turbulent plasma.

If the plasma is described by the one-fluid MHD approximation, its inertial range is characterized by an energy spectrum following a $E_k \sim k^{-5/3}$ power law, i.e. the Kolmogorov spectrum for isotropic, stationary and incompressible turbulence. This power-law dependence was predicted by Kolmogorov [1941] for hydrodynamic turbulence using dimensional analysis. Using measurements of the solar wind at 1, 2.8 and 5 AU and assuming the Taylor hypothesis [Taylor, 1938], Matthaeus and Goldstein [1982] obtained energy spectra consistent with the Kolmogorov spectrum.

However, in-situ solar wind observations have shown that the $k^{-5/3}$ inertial range breaks down at some scale, presumably corresponding to the ion inertial length [Leamon et al., 2000]. At wavenumbers larger than this break, the magnetic spectra exhibit slightly steeper power laws [Goldstein et al., 1994, Ghosh et al., 1996, Leamon et al., 1998]. assuming to be at scales smaller than the ion inertial length, Biskamp et al. [1999] found that the energy spectrum follows a $k^{-7/3}$ power

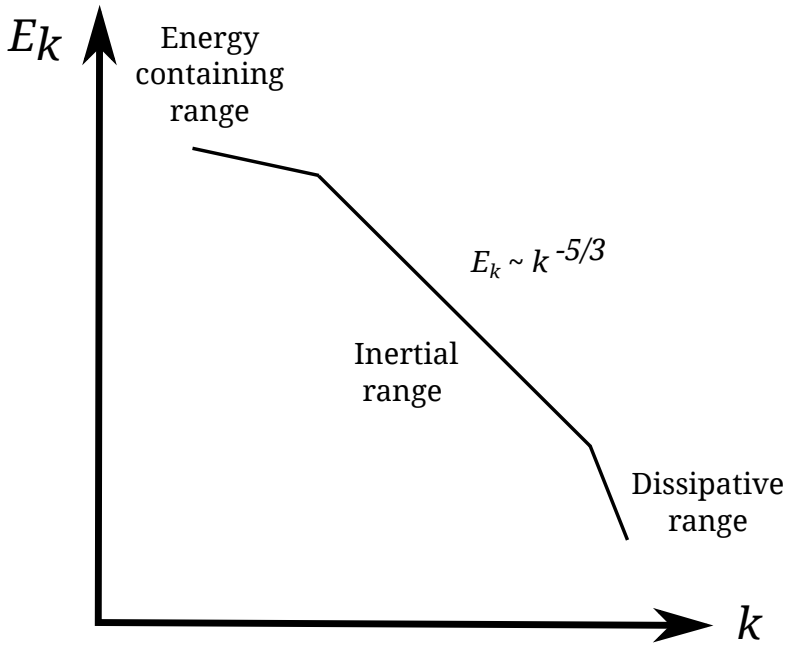

FIGURE 1.2: Schematic representation of the power cascade of hydrodynamic turbulence.

law. This prediction was later confirmed by numerical simulations [Galtier, 2006, Gómez et al., 2008]. The traditional explanation for this turbulence regime is that it is associated with an energy cascade process involving dispersive waves, such as ion-cyclotron and/or whistler modes [Ghosh et al., 1996].

Recently, Sahraoui et al. [2009] reported evidence of a new breakpoint (at even smaller scales) in the magnetic energy spectrum from solar wind observations obtained with the multi-spacecraft Cluster mission. These results confirm the break at a wavenumber presumably consistent with the inverse ion inertial length [Leamon et al., 2000, Smith et al., 2001], and find a second break at larger wavenumbers. In the solar wind plasma at 1 AU, the electron gyro-scale is very close to the electron inertial length ($\sim$ 12 km) and therefore it is not clear to which of these scales it corresponds. The authors confirmed the Kolmogorov spectrum at the largest scales, a second power law $k^{-7/3}$ at intermediate scale and a steeper power law $k^{-4.1}$ at the smallest scales (beyond the second break).

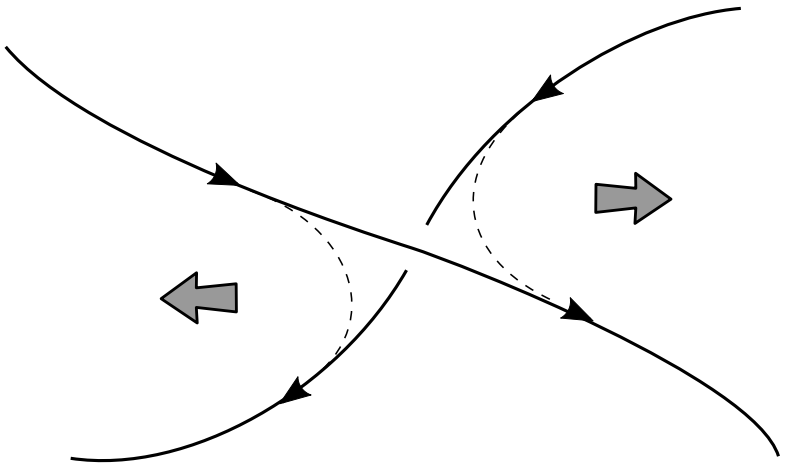

FIGURE 1.3: Basic picture of magnetic reconnection: plasma acceleration by a local change of magnetic field lines topology.

These spectral breaks are probably caused by kinetic effects and cannot be described by the one-fluid MHD description. One possible way to include some kinetic effects within a fluidistic framework, is to adopt a multi-fluid approach to acknowledge the presence of various particle species in a plasma. In particular, we study the solar wind turbulence within the framework of a full two-fluid MHD description, retaining the effects of the Hall current, electron pressure and electron inertia. The main purpose of Chapter 3 is to explore the physics of a complete two-fluid model and compare it with in-situ solar wind measurements.

1.4 Collisionless magnetic reconnection

Magnetic reconnection is a process which converts magnetic free energy into heat and kinetic energy. Through this process, two magnetic field lines with opposite orientations *reconnect* into two new magnetic field lines (see Figure 1.3). The energy difference between these two magnetic configurations, is transferred to the plasma particles. To understand the physics behind the magnetic reconnection process, it is important first to understand the magnetic field topology.

Let us suppose that we have a plasma-fluid element moving as sketched in Figure 1.4. To study the magnetic field topology, we analyze the magnetic flux changes. This change, for any arbitrary closed loop moving with the fluid (see Figure 1.4) can be written as

$$\frac{d}{dt}\int \mathbf{B}\cdot\mathbf{dS} = \int \frac{\partial \mathbf{B}}{\partial t}\cdot\mathbf{dS} - \oint (\mathbf{u}\times\mathbf{B})\cdot\mathbf{dl}, \tag{1.1}$$

where we have separated the change due time variation of $\mathbf{B}$ (on the first term right hand side) and the change due the motion of the loop (on the second term right hand side). Using Faraday's law and Stokes's theorem, we can write this equation as

$$\frac{d}{dt}\int \mathbf{B}\cdot\mathbf{dS} = -c\oint \mathbf{E}\cdot\mathbf{dl} - \oint (\mathbf{u}\times\mathbf{B})\cdot\mathbf{dl}. \tag{1.2}$$

In the ideal one-fluid MHD limit, the electric field in a reference frame moving with the fluid is identically zero, i.e.

$$\mathbf{E} + \frac{\mathbf{u}}{c}\times\mathbf{B} = 0. \tag{1.3}$$

Therefore, in this case, the right hand of equation (1.2) is identically zero. As a result, in the ideal MHD the magnetic flux trapped into any closed loop moving with the fluid, is conserved. In other words, we say that the magnetic field is *frozen-in* to the plasma. A consequence of the frozen-in condition is that two magnetic field lines cannot pass through each other, and therefore no topological change in the magnetic field lines can occur in ideal MHD.

The first model of magnetic reconnection was developed within the framework of resistive one-fluid MHD, the so-called Sweet-Parker model [Sweet, 1958, Parker, 1957]. In the Sweet-Parker regime, the magnetic resistivity can in principle break

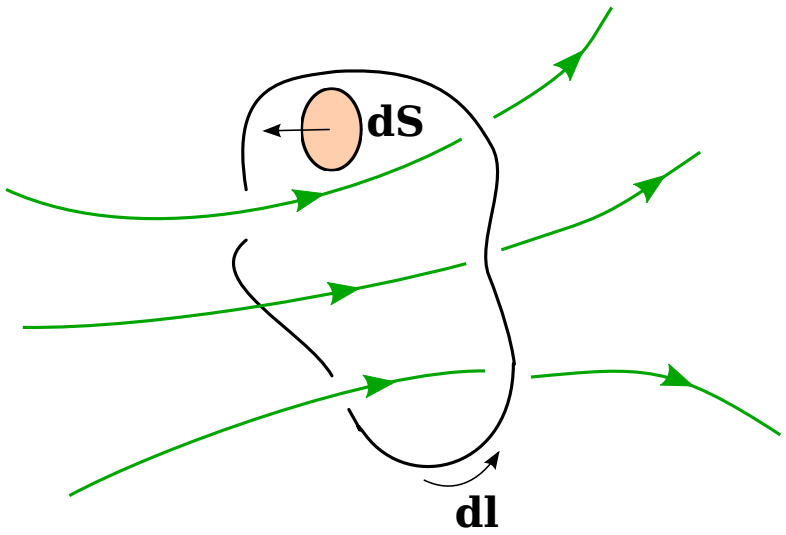

FIGURE 1.4: Schematic plasma-fluid element (black) with magnetic field lines (green) passing through it.

the frozen-in condition. In the resistive-MHD approximation

$$\mathbf{E} + \frac{\mathbf{u}}{c} \times \mathbf{B} = \frac{\eta}{c} \boldsymbol{\nabla} \times \mathbf{B} \tag{1.4}$$

where η is the magnetic resistivity. The right hand side of equation (1.4) does not vanish (it becomes proportional to η), and therefore the magnetic flux enclosed by loops moving with the fluid is in general not conserved. The frozen-in condition is no longer valid, thus allowing magnetic reconnection to occur. In space plasma, the resistivity is usually negligible. The right hand side of equation (1.4) can then be dropped, except in regions with extremely large current densities ($\mathbf{J} = (c/4\pi)\boldsymbol{\nabla} \times \mathbf{B}$). In Chapter 4, we show that the reconnection rate, which measures the efficiency of the reconnection process scales as $\eta^{1/2}$.

This result, derived by Parker in the late 1950s, seemed to be the answer to the magnetic reconnection process. However, using typical values for the solar corona, a solar flare would take tens of days to grow, rather than a few minutes as it is observed [Yamada, 2011]. Moreover, and because η is very small, the $\eta^{1/2}$ scaling leads to exceedingly low reconnection rates for most space physics environments

[Bhattacharjee, 2004, Øieroset et al., 2007, Fujisawa et al., 2007]. In the earlies 1960s, Petschek [1964] reported a possible solution to the slow reconnection rates, giving rise to the concept of fast magnetic reconnection, i.e. reconnection rates that are not proportional to a power of the resistivity. In contrast to the $\eta^{1/2}$ scaling, the Petschek solution shows a weak logarithmic dependence on magnetic resistivity. However, numerical simulations showed that the typical Petschek configuration cannot be attained in a model with a spatially uniform resistivity [e.g. Biskamp, 1986].

Kinetic plasma effects, such as the Hall effect and electron inertia, introduce new spatial and temporal scales into the theoretical fluid description, represented by new terms on the right hand side of equation (1.4). In Chapter 4, we study (both theoretically and numerically) the collisionless magnetic reconnection process using a full two-fluid model for a completely ionized hydrogen plasma. In particular, we run simulations with zero magnetic resistivity and check that we are not spuriously adding numerical resistivity. Therefore, we are certain that reconnection in our simulations arises exclusively as a result of finite electron inertia, and not because of the presence of physical or numerical resistivity.

1.5 ULF waves foreshock boundary (UWFB)

A collisionless bow shock is the result of the interactions between the supersonic (and supermagnetosonic) solar wind and planetary magnetospheres. The inflow of matter into the bow shock is so fast that the time scales on which dissipation would take place are too long to dissipate the excess of energy and lowering the inflow velocity [Turner, 1986]. To help maintain a stationary shock transition, a small amount of the incoming flow is reflected backstreaming in the upstream direction. However, this particle reflection process is not a direct dissipation mechanism.

Instead, it is an emergency act of the shock to reduce the inflow momentum and energy [see Treumann, 2009].

The backstreaming particles are subjected to the solar wind's $\mathbf{E}\times\mathbf{B}$ drift. The $\mathbf{E}\times\mathbf{B}$ drift velocity (which is the constant motion of the guiding center of charges immersed in uniform $\mathbf{E}$ and $\mathbf{B}$ fields) is the same for all backstreaming particles (i.e. regardless of their mass and charge), and perpendicular to the IMF. As a result, the guiding centers of all backstreaming particles move within the $\mathbf{v}_{\mathrm{sw}}$-$\mathbf{B}$ plane, gradually drifting away from the field line tangent to the bow shock toward the inner part of the foreshock and being segregated according to their parallel velocities. Figure 1.5 shows the schematic structure of a foreshock region, for a particular IMF configuration. The tangent field line marks the points at which the solar wind becomes magnetically connected to the bow shock. Behind this line, protons (and electrons) through different acceleration mechanisms can escape from the bow shock back to the upstream region (see Chapter 2). The electrons, because of their much smaller inertia, are much less affected by the $\mathbf{E}\times\mathbf{B}$ drift and their presence can be detected right next to the tangent field line [Fuselier et al., 1985, Sigsbee et al., 2004a,b]. On the other hand, the backstreaming ions which are ejected with velocity $\mathbf{u}_{\mathrm{FAB}}$ (FAB: field-aligned beam) are subjected to the drift and therefore the upstream ion foreshock boundary is in general not aligned to the IMF.

Since ULF waves are presumably generated by instabilities driven by backstreaming ions, the region of ULF wave activity is embedded in the ion foreshock. Because of the finite growth rate of these instabilities combined with convection, these waves can reach significant amplitudes away from the source region. Therefore, the onset of waves is spatially localized in an extended surface in the ion foreshock known as the ULF wave foreshock boundary (UWFB). For a precise identification

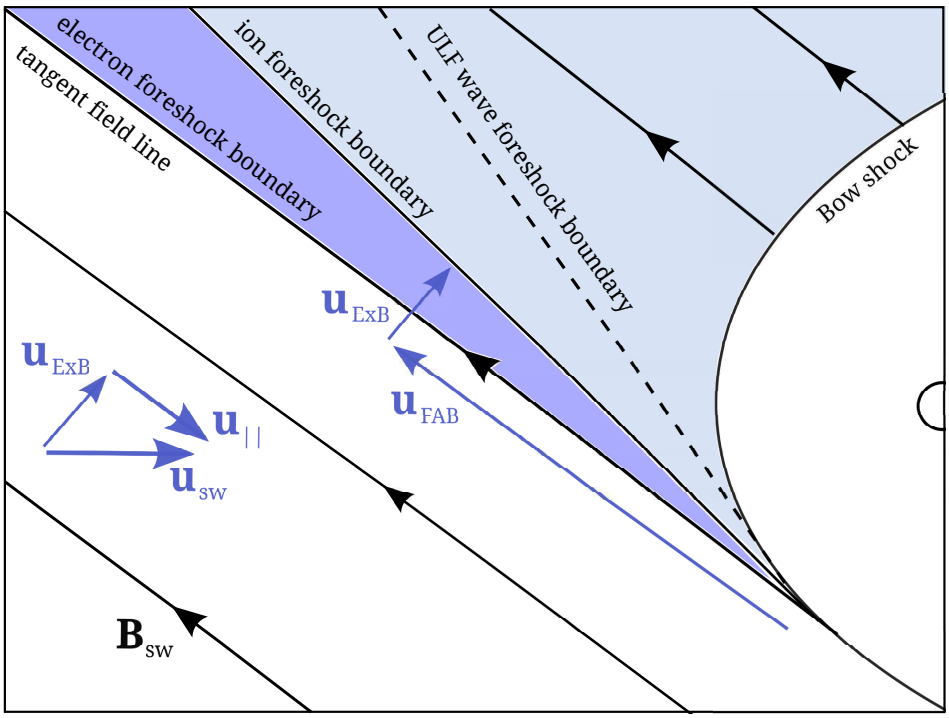

FIGURE 1.5: Schematic structure of a foreshock region for a particular IMF configuration.

of the UWFB, the IMF is expected to perform a very slow and monotonic rotation as the spacecraft crosses this boundary.

In Chapter 5 we study spatial distribution of ULF waves at the foreshocks of Saturn and the Earth. As we describe in Chapter 2, these foreshock ULF waves can arise in a three-fluid description. Then, using in-situ measurements from Cassini (at Saturn) and Cluster (at the Earth), we investigate the relations between the ULF wave foreshock boundary and the acceleration mechanisms for the backstreaming ions responsible for the ULF waves generation.

1.6 Resumen en castellano

En la sección 1.1, introducimos el concepto de viento solar. Éste es el escenario para los fenomenos de plasma estudiados. En particular, presentamos los tres principales procesos de pequeña-escala estudiados en la Tesis. Es decir,

- Turbulencia: las interacciones no-lineales, la cascada de energía, el espectro de Kolmogorov, y el espectro de energía magnética en las pequeñas-escalas.
- Reconexión magnética no-colisional: el cambio de topología de las líneas de campo magnético y el modelo de Sweet-Parker.
- Generación y distribución de ondas de ultra-baja frequencia (ULF): la presencia de una onda de choque en planetas magnetizados, la morfología del *foreshock*, la existencia de ondas de ondas ULF, la frontera para las ondas ULF y los modelos de aceleración en la onda de choque.

En la sección 1.2, introducimos la necesidad de una descripción de multi-fluidos mas allá de la tradicional magnetohidrodinámica (MHD).

Finalmente, en las siguiente tres secciones 3-1.5, introducimos brevemente cada uno de los problemas estudiados en la Tesis.

Chapter 2

Theoretical descriptions of space plasmas

Give me another theory that would fit the facts.
'I could very easily give you half a dozen' said Holmes.
'Here, for example, is a very possible and even probable one.'
The Adventure of the Norwood Builder. Sir Arthur Conan Doyle.

One-fluid MHD is an appropriate theoretical framework to describe the dynamics of plasmas at their largest temporal and spatial scales. Examples of this are models of magnetic dynamo, MHD turbulence or magnetic reconnection. However, as we move progressively toward smaller scales, the one-fluid MHD description might no longer be completely adequate. For instance, in a truly collisionless regime, magnetic reconnection should be driven solely by electron inertia, which is absent in the traditional one-fluid MHD. In order to capture these and other non ideal effects, in this Chapter we consider a multi-species theoretical description for a plasma. In particular, here we present a full two-fluid MHD model and a three-fluid description for a plasma. In the first case, we calculate the normal modes

of oscillation, while the three-fluid description is used to simulate a beam of ions traveling along magnetic field lines and exciting low-frequency plasma waves. The latter study aims at understanding the onset of ULF waves observed in planetary foreshocks, which can not be achieved from the one- or even two-fluid descriptions. Finally, we briefly study theoretical mechanisms of particle acceleration emission at planetary bow shocks, where the ion beams presumably originate.

2.1 Multi-species description of plasmas

In this section, we consider a multi-species theoretical description of a plasma. More specifically, we consider a fluid description for N species of particles. For each particle species s (with $s = 1, \ldots, N$), the continuity equation is

$$\frac{\partial n_s}{\partial t} + \boldsymbol{\nabla} \cdot (n_s \mathbf{u}_s) = 0 \tag{2.1}$$

where n_s is the number density and $\mathbf{u}_s$ the velocity of the species s, respectively. The equation of motion for each species s is

$$m_s n_s \left[\frac{\partial \mathbf{u}_s}{\partial t} + (\mathbf{u}_s \cdot \boldsymbol{\nabla}) \mathbf{u}_s \right] = q_s n_s (\mathbf{E} + \frac{1}{c} \mathbf{u}_s \times \mathbf{B}) - \boldsymbol{\nabla} p_s + \mu_s \nabla^2 \mathbf{u}_s + \sum_p \mathbf{R}_{sp} \tag{2.2}$$

Here $\mathbf{B}$ and $\mathbf{E}$ are the magnetic and electric fields, q_s is the particle electric charge, c is the speed of light, p_s is the isotropic-scalar pressure, μ_s is the viscosity and $\mathbf{R}_{sp}$ ($\mathbf{R}_{sp} = -\mathbf{R}_{ps}$) is the rate of momentum gained by the species s due to collisions with the species p. This momentum exchange rate is assumed to be proportional to the relative speed between species, i.e.

$$\mathbf{R}_{sp} = -n_s m_s \nu_{sp} (\mathbf{u}_s - \mathbf{u}_p) \tag{2.3}$$

where ν_{sp} is the collisional frequency of species s against species p.

Together with equations (2.1) and (2.2), we consider Maxwell's equations, which describe the generation of electric and magnetic fields as a result of the charges and electric currents contained in the plasma. Maxwell's equations in the non-relativistic limit are

$$\boldsymbol{\nabla} \cdot \mathbf{E} = 4\pi\rho_c \tag{2.4}$$

$$\boldsymbol{\nabla} \cdot \mathbf{B} = 0 \tag{2.5}$$

$$\boldsymbol{\nabla} \times \mathbf{E} = -\frac{1}{c}\frac{\partial \mathbf{B}}{\partial t} \tag{2.6}$$

$$\boldsymbol{\nabla} \times \mathbf{B} = \frac{4\pi}{c}\mathbf{j} \tag{2.7}$$

where the electric current density is given by the contribution of all species

$$\mathbf{J} = \frac{c}{4\pi}\boldsymbol{\nabla} \times \mathbf{B} = \sum_{s=1}^{N} q_s n_s \mathbf{u}_s. \tag{2.8}$$

and the charge density is

$$\rho_c = \sum_{s=1}^{N} q_s n_s \tag{2.9}$$

Note that the displacement current in equation (2.7) has been neglected, which is a good approximation for non-relativistic plasmas (i.e. $u^2 << c^2$).

In the ideal collisionless limit, i.e., the dissipation terms in equation (2.2) are neglected and the equation of motion yield

$$m_s n_s \frac{d\mathbf{u}_s}{dt} = q_s n_s (\mathbf{E} + \frac{1}{c}\mathbf{u}_s \times \mathbf{B}) - \boldsymbol{\nabla} p_s. \tag{2.10}$$

where the total derivatives are

$$\frac{d\mathbf{u}_s}{dt} \equiv \frac{\partial \mathbf{u}_s}{\partial t} + (\mathbf{u}_s \cdot \boldsymbol{\nabla})\mathbf{u}_s. \tag{2.11}$$

Assuming that each species is also incompressible (i.e. $n_s = \text{const}$ and $\boldsymbol{\nabla} \cdot \mathbf{u}_s = 0$) and also that quasi-neutrality applies, i.e.

$$\sum_{s=1}^{N} q_s n_s = 0, \tag{2.12}$$

the plasma displays $N + 1$ ideal invariants. As we expected in the absence of dissipation, one of them is the total energy E given by

$$E = \int d^3r \left(\sum_{s=1}^{N} \frac{m_s n_s u_s^2}{2} + \frac{B^2}{8\pi} \right) \tag{2.13}$$

The other N invariants are the helicity for each species, H_s

$$H_s = \int d^3r \left(\mathbf{A} + \frac{cm_s}{q_s} \mathbf{u}_s \right) \cdot \left(\mathbf{B} + \frac{cm_s}{q_s} \boldsymbol{\omega}_s \right) \tag{2.14}$$

where $\boldsymbol{\omega}_s = \boldsymbol{\nabla} \times \mathbf{u}_s$ is the vorticity of the species s. Quasi-neutrality is an excellent approximation for a non-relativistic plasma, basically guaranteed by the very fast electrons due to their negligible inertia. On more theoretical grounds, quasi-neutrality can be regarded as a consistency requirement, to accommodate the Lorentz invariance of Maxwell's equations with the Galilean invariance of the equations of motion.

2.2 Electron inertia Hall-MHD

In this section, we derive the equations for a full two-fluid description of a plasma. In particular, we show how this framework extends the traditional Hall-MHD model including the electron inertia. The equations of motion for an incompressible plasma made of ions and electrons with mass $m_{i,e}$, charge $\pm e$, density $n_i = n_e = n$ (quasi-neutrality), isotropic pressure $p_{i,e}$ and velocity $\mathbf{u}_{i,e}$ respectively,

can be written as

$$m_i n \frac{d\mathbf{u}_i}{dt} = en(\mathbf{E} + \frac{1}{c}\mathbf{u}_i \times \mathbf{B}) - \boldsymbol{\nabla} p_i + \mu_i \nabla^2 \mathbf{u}_i + \mathbf{R}_{ie} \quad (2.15)$$

$$m_e n \frac{d\mathbf{u}_e}{dt} = -en(\mathbf{E} + \frac{1}{c}\mathbf{u}_e \times \mathbf{B}) - \boldsymbol{\nabla} p_e + \mu_e \nabla^2 \mathbf{u}_e + \mathbf{R}_{ei} \quad (2.16)$$

$$\mathbf{J} = \frac{c}{4\pi}\boldsymbol{\nabla} \times \mathbf{B} = en(\mathbf{u}_i - \mathbf{u}_e) \quad (2.17)$$

where $\mathbf{R}_{ie}$ ($\mathbf{R}_{ie} = -\mathbf{R}_{ei}$) is the rate of momentum gained by ions due to collisions with electrons. As we discussed in the previous Section, this momentum exchange rate is assumed to be proportional to the relative speed between species. More specifically,

$$\mathbf{R}_{ie} = -nm_i\nu_{ie}(\mathbf{u}_i - \mathbf{u}_e), \quad (2.18)$$

where ν_{ie} is the collisional frequency of an ion against electrons. In view of equation (2.17), this momentum exchange rate (or friction force between species) becomes proportional to the electric current density $\mathbf{J}$.

The set of equations (2.15, 2.16 and 2.17) can be written in dimensionless form in terms of a typical length scale L_0, the constant particle density n, a value B_0 for the magnetic field, a typical velocity $v_A = B_0/(4\pi nM)^{1/2}$ (the Alfvén velocity) where $M \equiv m_i + m_e$, and the electric field in units of $E_0 = v_A B_0/c$,

$$(1-\mu)\frac{d\mathbf{u}_i}{dt} = \frac{1}{\lambda}(\mathbf{E} + \mathbf{u}_i \times \mathbf{B}) - \boldsymbol{\nabla} p_i + \nu_i \nabla^2 \mathbf{u}_i + \frac{\mathbf{r}}{\lambda} \quad (2.19)$$

$$\mu\frac{d\mathbf{u}_e}{dt} = -\frac{1}{\lambda}(\mathbf{E} + \mathbf{u}_e \times \mathbf{B}) - \boldsymbol{\nabla} p_e + \nu_e \nabla^2 \mathbf{u}_e - \frac{\mathbf{r}}{\lambda} \quad (2.20)$$

$$\mathbf{J} = \frac{1}{\lambda}(\mathbf{u}_i - \mathbf{u}_e) \quad (2.21)$$

Here, we have introduced the dimensionless parameter $\mu \equiv m_e/M$ and $\lambda \equiv c/\omega_{pM}L_0$ (the Hall parameter), and $\omega_{pM} = (4\pi e^2 n/M)^{1/2}$, which has the form

of a plasma frequency for a particle of mass M. The dimensionless momentum exchange rate is $\mathbf{r} = -\eta\mathbf{J}$, and $\eta = m_i c^2 \nu_{ie}/(4\pi e^2 n v_A L_0)$ is the (dimensionless) electric resistivity. The dimensionless ion and electron inertial lengths can be simply defined in terms of their corresponding plasma frequencies $\omega_{pi,e} = (4\pi e^2 n/m_{i,e})^{1/2}$ as $\lambda_{i,e} \equiv c/\omega_{pi,e}L_0$. Note that in the limit of electron inertia equal to zero ($\mu \to 0$), we obtain $\omega_{pM} = \omega_{pi}$, and therefore the Hall parameter $\lambda = \lambda_i = c/\omega_{pi}L_0$ reduces to the ion inertial length. However, throughout this Chapter we retain the effect of electron inertia by setting the parameter $\mu \neq 0$. For a fully ionized hydrogen plasma $\mu \ll 1$ and, as a result, $\lambda \neq \lambda_i \gg \lambda_e$. Nonetheless, the current theoretical description may also be applied to an electron-positron plasma (for which $\mu = 1/2$), since it is actually valid for $0 \leq \mu < 1$. The expressions for the dimensionless ion and electron inertial scales ($\lambda_{i,e}$) in terms of the two dimensionless parameters μ and λ are simply $\lambda_i = (1-\mu)^{1/2}\lambda$ and $\lambda_e = \mu^{1/2}\lambda$.

In order to obtain a hydrodynamic description of this full two-fluid plasma, we replace the velocity field for each species (i.e. $\mathbf{u}_{i,e}$) in terms of two new vector fields. Namely, the hydrodynamic velocity $\mathbf{u}$ given by

$$\mathbf{u} = (1-\mu)\mathbf{u}_i + \mu\mathbf{u}_e \tag{2.22}$$

and the electric current density $\mathbf{J}$ given by (2.21). From equations (2.21)-(2.22), we can readily obtain the velocity of each species as

$$\mathbf{u}_i = \mathbf{u} + \mu\lambda\mathbf{J} \tag{2.23}$$

$$\mathbf{u}_e = \mathbf{u} - (1-\mu)\lambda\mathbf{J} \tag{2.24}$$

The hydrodynamic equation of motion is the sum of the ion and electron equations of motion (2.19) and (2.20),

$$\frac{d\mathbf{u}}{dt} = \mathbf{J} \times \left[\mathbf{B} - \mu(1-\mu)\lambda^2\nabla^2\mathbf{B}\right] - \boldsymbol{\nabla} p + \nu\nabla^2\mathbf{u} + \nu_0\nabla^2\mathbf{J} \tag{2.25}$$

where $p \equiv p_i + p_e$ is the total pressure, $\nu = \nu_i + \nu_e$ and $\nu_0 = \lambda(\mu\nu_i - (1-\mu)\nu_e)$. Following the expressions obtained by Braginskii [1965] and assuming both species share a common temperature, the ratio of viscosities is only a function of the mass ratio, i.e.

$$\frac{\nu_e}{\nu_i} = 0.54\sqrt{\frac{\mu}{1-\mu}} \tag{2.26}$$

which shows that viscosity is predominantly due to ions.

Note that most of the terms in equation (2.25) can easily be identified as a sum of the corresponding terms in equations (2.19)-(2.20), but the convective derivatives in these equations are nonlinear terms that have also been properly taken into account, giving rise to a new nonlinear term (proportional to μ) in equation (2.25). Note also that in the limit of negligible electron inertia, equation (2.25) reduces to the equation of motion for ideal, one-fluid MHD. This is the case for the HMHD description as well, which is a two-fluid theoretical description, but considering massless electrons.

On the other hand, if we use $\mathbf{E} = -\partial_t\mathbf{A} - \nabla\phi$ and $(\mathbf{u}_e \cdot \nabla)\mathbf{u}_e = \boldsymbol{\omega}_e \times \mathbf{u}_e + \nabla(u_e^2/2)$ (with $\boldsymbol{\omega}_e = \nabla \times \mathbf{u}_e$ being the electron vorticity) the equation of motion for electrons (2.20) can be written as

$$\frac{\partial}{\partial t}(\mathbf{A} - \mu\lambda\mathbf{u}_e) = \mathbf{u}_e \times (\mathbf{B} - \mu\lambda\boldsymbol{\omega}_e) + \nabla(\lambda p_e + \mu\lambda\frac{u_e^2}{2} - \phi) - \lambda\nu_e\nabla^2\mathbf{u}_e - \eta\mathbf{J} \tag{2.27}$$

Furthermore, we define

$$\mathbf{B}' \equiv \mathbf{B} - \mu\lambda\boldsymbol{\omega}_e = \mathbf{B} - \mu(1-\mu)\lambda^2\nabla^2\mathbf{B} - \mu\lambda\boldsymbol{\omega}, \tag{2.28}$$

where $\boldsymbol{\omega} = \boldsymbol{\nabla}\times\mathbf{u}$ is the hydrodynamic vorticity, and if we take the curl of equation (2.27) it is possible to obtain a dynamical equation for the magnetic field, namely:

$$\partial_t\,\mathbf{B}' = \boldsymbol{\nabla}\times[\mathbf{u} - (1-\mu)\lambda\mathbf{J}]\times\mathbf{B}' + \eta\nabla^2\mathbf{B} - \lambda\nu_e\nabla^2\boldsymbol{\omega} - (1-\mu)\lambda^2\nu_e\nabla^4\mathbf{B}. \tag{2.29}$$

Equations (2.25) and (2.29) are the Electron Inertia Hall-MHD (EIHMHD) equations. It is interesting to note that the presence of the electron mass (and the corresponding viscosity coefficient ν_e) introduces high-order spatial (short wavelength) derivative terms that play the role of hyperviscosity. This certainly has an impact at large wavenumbers, affecting the distribution of energy at the small scales and the dissipative range of the energy power spectrum. The major source of dissipation of magnetic field in a plasma where the electron mass is not neglected, is the friction between the electrons themselves and not the loss of momentum of the electrons by collision with ions (as in the MHD and HMHD cases). This can be seen in the last term of equation (2.29), which together with the third term (on the right hand side) came from the curl of the dissipative term in the fluid equation of electrons, a term that cannot be neglected if we consider electron inertia (and the resulting momentum and energy transport due to the electrons).

It is also possible to obtain an equation for the electric field $\mathbf{E}$ by making use of equations (2.25), (2.28), (2.29) and the Maxwell–Faraday equation (2.6) (in dimensionless form),

$$\boldsymbol{\nabla}\times\mathbf{E} = -\frac{\partial\mathbf{B}}{\partial t} \tag{2.30}$$

It is useful to consider this equation in Fourier space to obtain a closed expression

for the electric field. First the partial time derivative of equation (2.28) in Fourier space reads

$$\frac{\partial \hat{\mathbf{B}}'}{\partial t} = \alpha_k \frac{\partial \hat{\mathbf{B}}}{\partial t} - \mu\lambda \frac{\partial \hat{\boldsymbol{\omega}}}{\partial t} \tag{2.31}$$

where $\alpha_k \equiv 1 + (1-\mu)\mu\lambda^2 k^2$ since $\boldsymbol{\nabla} \rightarrow i\mathbf{k}$ and the circumflex represents the Fourier transform. By rearranging terms and using equation (2.30) in Fourier space we get an equation for the electric field in Fourier space:

$$i\mathbf{k} \times \hat{\mathbf{E}} \;=\; \alpha_k^{-1}\left(\frac{\partial \hat{\mathbf{B}}'}{\partial t} + \mu\lambda \frac{\partial \hat{\boldsymbol{\omega}}}{\partial t}\right). \tag{2.32}$$

Here, the two right-hand side terms are calculated from equations (2.25) and (2.29) respectively as,

$$\frac{\partial \hat{\boldsymbol{\omega}}}{\partial t} = i\mathbf{k} \times \widehat{(\mathbf{J} \times \mathbf{B}')} + i\mu\lambda\mathbf{k} \times \widehat{(\mathbf{u}_i \times \boldsymbol{\omega})} - k^2(\nu\hat{\mathbf{u}} + \nu_0\hat{\mathbf{J}}) \tag{2.33}$$

$$\frac{\partial \hat{\mathbf{B}}'}{\partial t} = i\mathbf{k} \times \widehat{(\mathbf{u}_e \times \mathbf{B}')} - k^2(\eta\hat{\mathbf{B}} - \lambda\nu_e\hat{\boldsymbol{\omega}}) - (1-\mu)\lambda^2\nu_e k^4\hat{\mathbf{B}} \tag{2.34}$$

The equation for the electric field is obtained applying $(\boldsymbol{\nabla}\times)^{-1}$ to equation (2.32), which gives rise to the gradient of an undetermined function $g(\mathbf{r}, t)$, which can be associated with the electrostatic potential. This function $g(\mathbf{r}, t)$ can be obtained from the Poisson equation that results from taking the divergence of the equation.

2.3 Normal modes

The linear theory of plasma fluctuations (i.e. waves or instabilities) in an homogeneous plasma under static equilibrium, leads among other results to the dispersion relation $\omega(\mathbf{k})$ between the frequency ω and the wavenumber $\mathbf{k}$ of these fluctuations. The linear EIHMHD equations are therefore subject to a Fourier analysis

in space and time, which yield such a dispersion relation. In the present Thesis, we treat it as an initial value problem, i.e the $\mathbf{k}$ components are given real values and we solve for a complex $\omega = \omega_r + i\gamma$, where the real part ω_r is the proper frequency and the imaginary part γ is the instability growth rate. If one obtains a non-zero γ, then the waves may be exponentially damped (if $\gamma < 0$) or grow (if $\gamma > 0$). In general, if we have a fluid with no external forces, the dispersion relation typically yields non-growing nor damped roots (i.e. $\gamma = 0$) [Gary, 1993]. On the other hand, if there is some free energy source in the system (for instance, a relative drift speed between species) it can be driven unstable and lead to an instability (see next Section 2.4).

In the previous Section, we have derived the two-fluid equations for a plasma. In particular, the dimensionless ideal EIHMHD equations are

$$n\frac{d\mathbf{u}}{dt} = -\frac{\beta}{\Gamma}\boldsymbol{\nabla}p + \mathbf{J}\times\left[\mathbf{B} - \mu(1-\mu)\lambda^2\nabla^2\mathbf{B}\right] \tag{2.35}$$

$$\frac{\partial\mathbf{B}'}{\partial t} = \boldsymbol{\nabla}\times[\mathbf{u} - (1-\mu)\lambda\mathbf{J}]\times\mathbf{B}' \tag{2.36}$$

$$\frac{\partial n}{\partial t} = -\boldsymbol{\nabla}\cdot(n\mathbf{u}) \tag{2.37}$$

$$\frac{p}{n^\Gamma} = \text{const} \tag{2.38}$$

where equations (2.35) and (2.36) are the ideal Navier-Stokes and induction equations, respectively. Equation (2.37) is the continuity equation for a compressible plasma and equation (2.38) is the polytropic equation of state where Γ is the polytropic index (in the incompressible limit, equation (2.37) reduces to $\boldsymbol{\nabla}\cdot\mathbf{u} = 0$ and equation (2.38) is no longer required). We can explore the time-dependent fluctuations around a static equilibrium (i.e. $\mathrm{u}_0 = 0$) given by a homogeneous magnetic field of intensity $\mathrm{B}_0 = 1$ in the $\hat{\mathbf{z}}$ direction, a number density $n_0 = 1$ and pressure $p_0 = 1$. The set of equations (2.35)-(2.38) is non-linear, however as we discussed above we can take into account small-amplitude perturbations and find a

linear set of differential equations that describe the small-amplitude perturbation dynamics.

Therefore, we perturb the static equilibrium (i.e. f_0) introducing a small perturbation (i.e. δf) of all relevant variables

$$\mathbf{u} \rightarrow \delta\mathbf{u} \tag{2.39}$$

$$\mathbf{B} \rightarrow \mathbf{B}_0 + \delta\mathbf{B} \tag{2.40}$$

$$p \rightarrow p_0 + \delta p \tag{2.41}$$

$$n \rightarrow n_0 + \delta n. \tag{2.42}$$

Then, we substitute these expressions into equations (2.35)-(2.38) and obtain,

$$\frac{\partial \delta\mathbf{u}}{\partial t} = -\frac{\beta}{\Gamma}\boldsymbol{\nabla}\delta p + (\boldsymbol{\nabla}\times\delta\mathbf{B})\times\hat{\mathbf{z}} \tag{2.43}$$

$$\frac{\partial \delta\mathbf{B}'}{\partial t} = \boldsymbol{\nabla}\times(\delta\mathbf{u}\times\hat{\mathbf{z}}) - (1-\mu)\lambda\boldsymbol{\nabla}\times\left[(\boldsymbol{\nabla}\times\delta\mathbf{B})\times\hat{\mathbf{z}}\right] \tag{2.44}$$

$$\frac{\partial \delta n}{\partial t} = -\boldsymbol{\nabla}\cdot(\delta\mathbf{u}) \tag{2.45}$$

$$\delta p = \Gamma\delta n. \tag{2.46}$$

This linear set of equations is homogeneous, and with constant coefficients. Therefore the solutions are plane traveling waves,

$$\delta f = f_1 e^{i(\mathbf{k}\cdot\mathbf{x}-\omega t)} \tag{2.47}$$

where f_1 is a complex amplitude, $\mathbf{k}$ is the wave number vector and ω the temporal frequency. In this context, the partial derivative spatial and temporal linear

operators simply correspond to

$$\boldsymbol{\nabla}\cdot \;\rightarrow\; i\mathbf{k}\cdot \tag{2.48}$$

$$\boldsymbol{\nabla}\times \;\rightarrow\; i\mathbf{k}\times \tag{2.49}$$

$$\partial_t \;\rightarrow\; -i\omega \tag{2.50}$$

which transforms the set of equations (2.43)-(2.46) into an eigenvalue-eigenvector problem

$$-\omega\mathbf{u}_1 \;=\; -\beta\mathbf{k}n_1 + (\mathbf{k}\times\mathbf{B}_1)\times\hat{\mathbf{z}} \tag{2.51}$$

$$-\omega\mathbf{B}_1 \;+\; \omega c_1\mathbf{k}\times(\mathbf{k}\times\mathbf{B}_1) + \omega\mu\lambda i\mathbf{k}\times\mathbf{u}_1 = \mathbf{k}\times(\mathbf{u}_1\times\hat{\mathbf{z}}) - c_2\mathbf{k}\times\left[(i\mathbf{k}\times\mathbf{B}_1)\times\hat{\mathbf{z}}\right] \tag{2.52}$$

$$-\omega n_1 \;=\; -\mathbf{k}\cdot\mathbf{u}_1 \tag{2.53}$$

where we have used $p_1 = \Gamma n_1$. We also have introduced two constants $c_1 \equiv \mu(1-\mu)\lambda^2$ and $c_2 \equiv (1-\mu)\lambda$.

Without loss of generality, we assume that the wave number vector has the form,

$$\mathbf{k} = k\sin\theta\hat{\mathbf{x}} + k\cos\theta\hat{\mathbf{z}} \tag{2.54}$$

where $|\mathbf{k}| = k$ and θ is the angle between the wavenumber vector and the equilibrium magnetic field. Then, let us write equations (2.51)-(2.53) in a convenient coordinate system, in which the first component is parallel to $\hat{\mathbf{k}}$ ($\hat{\parallel} = \hat{\mathbf{k}}$), the second one is in the direction $\hat{\mathbf{y}}\times\hat{\mathbf{k}}$ ($\hat{\perp} = \hat{\mathbf{y}}\times\hat{\mathbf{k}}$), and the third component is $\hat{\mathbf{y}}$. From Figure 2.1 is easy to see that the transformation between the Cartesian and the new basis is

$$\begin{pmatrix} \hat{\perp} \\ \hat{\parallel} \end{pmatrix} = \begin{pmatrix} \cos\theta & -\sin\theta \\ \sin\theta & \cos\theta \end{pmatrix} \cdot \begin{pmatrix} \hat{\boldsymbol{x}} \\ \hat{\boldsymbol{z}} \end{pmatrix} \tag{2.55}$$

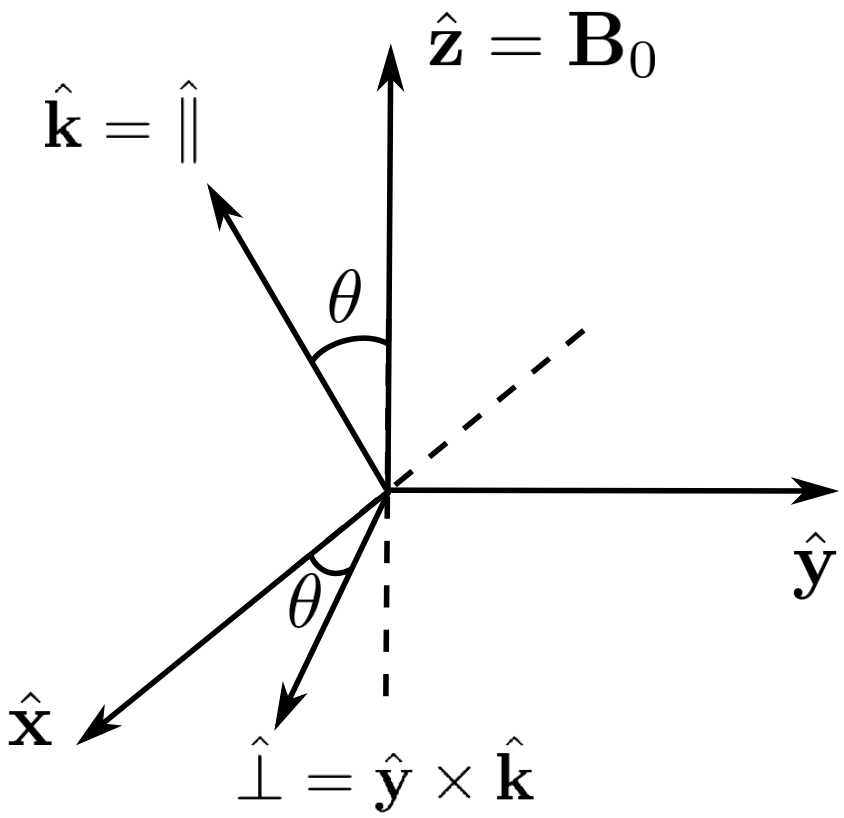

FIGURE 2.1: Definition of mean-field coordinate system ($\hat{\perp}$, $\hat{\parallel}$, $\hat{\mathbf{y}}$).

Using $\boldsymbol{\nabla} \cdot \mathbf{B} = 0$ and relations (2.55) we obtain the magnetic and velocity field in the new basis as

$$\mathbf{B}_1 = b_\perp \cos\theta \hat{\mathbf{x}} + b_y \hat{\mathbf{y}} + b_\perp \sin\theta \hat{\mathbf{z}} \tag{2.56}$$

$$\mathbf{u}_1 = (u_\perp \cos\theta + u_\parallel \sin\theta)\hat{\mathbf{x}} + u_y \hat{\mathbf{y}} + (-u_\perp \sin\theta + u_\parallel \cos\theta)\hat{\mathbf{z}} \tag{2.57}$$

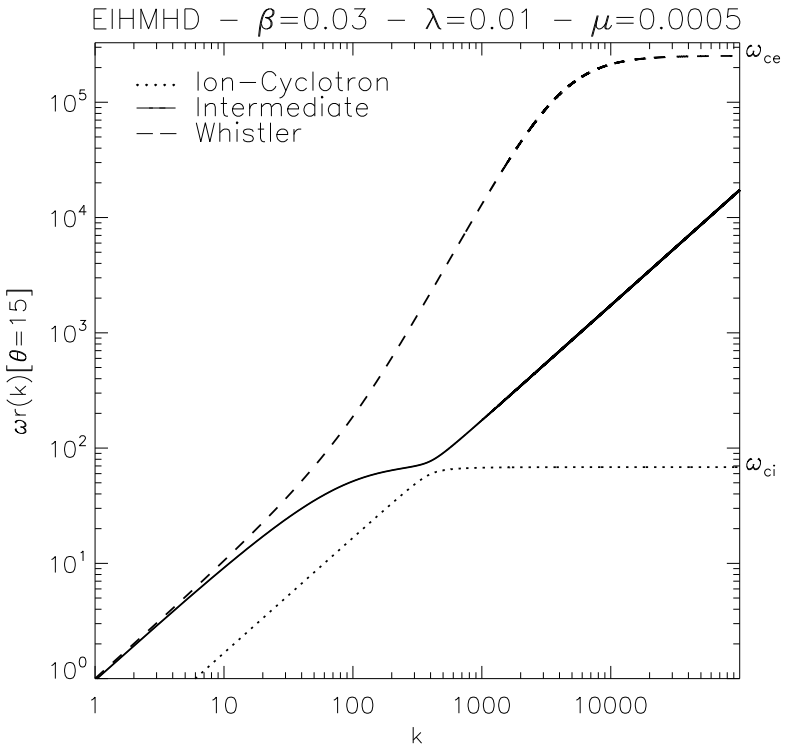

FIGURE 2.2: Linear propagation modes in EIHMHD model for a realistic mass ratio $\mu = 1/1837$, $\lambda = 0.01$ and $\theta = 0$. $\omega_{ce,i}$ are the electron and ion cyclotron frequency, respectively.

where we have defined $b_\perp = B_x/\cos\theta$. Therefore, in the new coordinate system the components of equations (2.51)-(2.53) are

$$\begin{pmatrix} \frac{\omega}{k} & -1 & 0 & 0 & 0 & 0 \\ -\beta & \frac{\omega}{k} & 0 & 0 & 0 & \sin\theta \\ 0 & 0 & \frac{\omega}{k} & \cos\theta & 0 & 0 \\ 0 & 0 & \cos\theta & \frac{\omega}{k}(1+c_1k^2) & -i\mu\lambda k\frac{\omega}{k} & -ic_2k\cos\theta \\ 0 & 0 & 0 & 0 & \frac{\omega}{k} & \cos\theta \\ 0 & \sin\theta & i\mu\lambda k\frac{\omega}{k} & ic_2k\cos\theta & \cos\theta & \frac{\omega}{k}(1+c_1k^2) \end{pmatrix} \cdot \begin{pmatrix} n_1 \\ u_\parallel \\ u_y \\ b_y \\ u_\perp \\ b_\perp \end{pmatrix} = 0 \quad (2.58)$$

Since we are interested in non-trivial solutions of an homogeneous set of equations, then the determinant of the coefficient matrix on the left hand of equation (2.58) needs to be zero. Therefore, setting the determinant equal to zero leads to the

following dispersion relation

$$\left(\frac{\omega}{k}\right)^6(1+c_1k^2)^2-\left(\frac{\omega}{k}\right)^4\left\{\beta(1+c_1k^2)^2+2\cos\theta^2\left[1+\frac{(1-\mu)^2+\mu^2}{2}\lambda^2k^2\right]\right.$$
$$\left.+\sin\theta^2(1+c_1k^2)\right\}+\left(\frac{\omega}{k}\right)^2\left\{\cos\theta^2+2\beta\cos\theta^2\left[1+\frac{(1-\mu)^2+\mu^2}{2}\lambda^2k^2\right]\right\}$$
$$-\beta\cos\theta^4=0 \quad (2.59)$$

which has 3 different modes with 2 different polarizations for each of them.

Figure 2.2 shows the dispersion relation for the 3 waves mode in EIHMHD, for a realistic mass ratio of $m_e/m_i = 1/1836$ (i.e. $\mu = 1/1837$), parallel propagation (i.e. $\theta = 0$) and $\lambda = 0.01$. The solid line corresponds to the Alfvén mode. As in HMHD [Gómez et al., 2008], the bottom branch (dotted line) represents the ion-cyclotron wave mode, which converges to the proton cyclotron frequency (i.e $\omega_{cp} = e\mathrm{B}_0/m_pc$). The top branch (dashed line) corresponds to the whistler branch and, in contrast to HMHD, it reaches a maximum given by the electron cyclotron frequency (i.e. $\omega_{ce} = e\mathrm{B}_0/m_ec$). Finally, for an arbitrary angle θ, we calculated the phase velocity corresponding to each normal mode. Figure 2.3 is a polar diagram, showing the phase velocity for each mode as a function of θ in the $\mathbf{B}_0$-$\mathbf{k}$ plane. In other words, the distance from the origin to the each curve indicates the phase velocity of each mode propagating in that particular direction.

2.4 Beam-driven instabilities

As we have seen, the perturbations of a two-fluid plasma perturbed from a homogeneous state and static equilibrium, does not drive wave instabilities. The reason is that there is no free-energy in the equilibrium state to fuel the instability. An example of a free energy source could be an electric current through a relative drift between species.

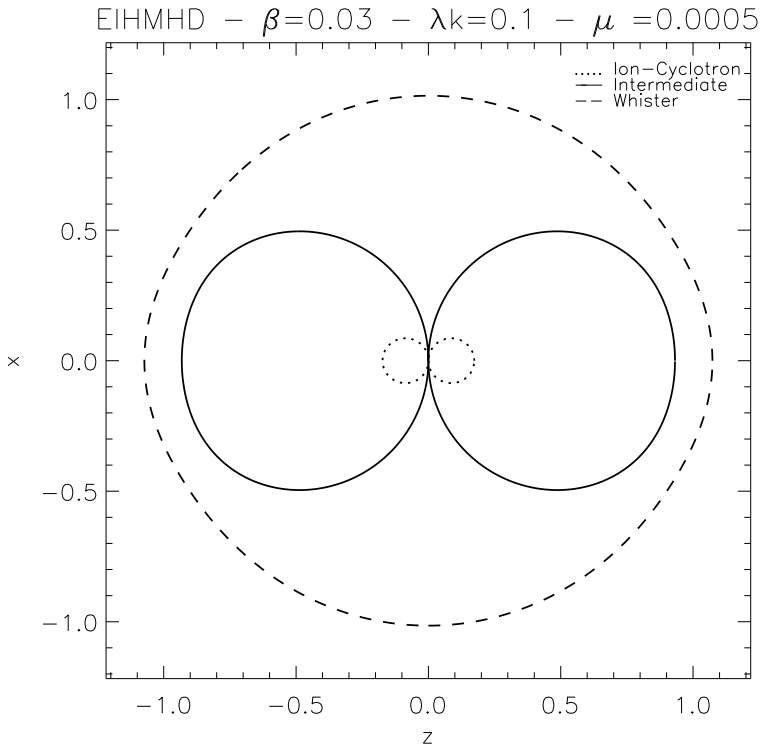

FIGURE 2.3: Polar diagram of velocity for the ion-cyclotron (dotted line), intermediate (solid line) and whistler branch (dashed line). In this case, we use $\mu = 1/1837$ and $\lambda\ k = 0.1$.

In this Section, we will consider the three-fluid description, in which a cold tenuous beam of protons (denoted by subscript b) interacts with a much dense background made of protons (subscript p) and massless electrons (subscript e). As we discuss below, this interaction will lead to plasma instabilities.

Let us consider a background plasma made of protons (with mass $m_p = m$ and charge $q_p = e$) and massless electrons ($m_e = 0$ and $q_e = -e$) and a cold beam of protons (with mass $m_b = m$ and charge $q_b = e$). Following the previous Section, in this case we will linearize a homogeneous equilibrium with a light beam of protons moving at a homogeneous speed with respect to the background to find the dispersion relationship $\omega(k)$. The system has the kinetic energy of the beam which is in principle available to drive the instabilities. The beam speed in general will depend on time, since it corresponds to the motion of charged particles in a homogeneous magnetic field.

We will seek for time-dependent perturbations around an equilibrium with a constant magnetic field of intensity B_0 in the $\hat{\mathbf{z}}$ direction, and a number density of electrons $n_{e0} = n_0$. The quasi-neutrality of the plasma requires

$$n_{0b} = \chi n_0 \tag{2.60}$$

$$n_{0p} = (1-\chi) n_0 \tag{2.61}$$

where $\chi << 1$ is the beam intensity.

Since the background electrons are assumed massless, the equation of motion in equilibrium is $\mathbf{E}_0 + (\mathbf{u}_{e0} \times \mathbf{B}_0) = 0$. If we describe the problem from the electron reference frame is $\mathbf{u}_{e0} = 0$ and therefore $E_0 = 0$. Assuming a time-dependent equilibrium velocity $\mathbf{u}_0$ for the beam and using the Ampere equation (2.8) we obtain

$$\mathbf{u}_{0b} = \mathbf{u}_0(t) \tag{2.62}$$

$$\mathbf{u}_{0p} = -\frac{\chi}{1-\chi}\mathbf{u}_0(t) \tag{2.63}$$

for the protons and the beam, respectively. Note that, as seen from the electron reference frame, also the background protons are moving, although at a small speed since $\chi << 1$.

Let us consider the equation of motion (2.2) for the beam in equilibrium,

$$\frac{\partial \mathbf{u}_0(t)}{\partial t} = \frac{eB_0}{mc}\mathbf{u}_0(t) \times \hat{\mathbf{z}}. \tag{2.64}$$

The equation can be easily integrated as

$$\mathbf{u}_{0b}(t) = u_0^{\parallel}\hat{\mathbf{z}} + \mathbf{u}^+ e^{i\Omega_{ci}t} + \mathbf{u}^- e^{-i\Omega_{ci}t} \tag{2.65}$$

where we have introduced the ion cyclotron frequency $\Omega_{ci} = eB_0/mc$, $\mathbf{u}^{\pm} \equiv u_0^{\perp}/2(\hat{\mathbf{x}} \pm i\hat{\mathbf{y}})e^{\pm i\phi^0}$, ϕ^0 is the phase, and $u_0^{\parallel}$ and $u_0^{\perp}$ are the beam velocities along and perpendicular to the magnetic field direction, respectively. The constants, $u_0^{\parallel}$, $u_0^{\perp}$ ϕ^0 are determined by the initial conditions of the problem.

To calculate the dispersion relation $\omega(k)$, we proceed as in Section 2.3. We perturb the static equilibrium introducing a small perturbation. Since the equilibrium velocities depend explicitly on time, in this case, departures from the equilibrium are expanded Fourier as

$$\delta n_s, \delta u_s^{\parallel} \rightarrow e^{kz}e^{i\mu t} \tag{2.66}$$

$$\delta u_s^{\perp}, \delta\mathbf{E}, \delta\mathbf{B} \rightarrow e^{kz}e^{i\omega t} \tag{2.67}$$

where we are assuming parallel propagation (i.e. $\mathbf{k} \parallel \mathbf{B}_0$), and in general $\mu \neq \omega$. We should note that $\delta\mathbf{E}$ and $\delta\mathbf{B}$ are perpendicular to $\hat{\mathbf{z}}$ since $\boldsymbol{\nabla}\cdot\mathbf{E} = \boldsymbol{\nabla}\cdot\mathbf{B} = 0$. From the continuity and motion equations (2.1)-(2.2) for the electrons and the beam we obtain the follow relations

$$\mu_{\pm} = \omega \pm \Omega_{ci} \tag{2.68}$$

which relate the frequencies in the parallel and perpendicular directions with the ion cyclotron frequency. On the other hand, from the continuity and motion equations (2.1)-(2.2) for the protons and Maxwell's equations (2.4)-(2.7) we obtain the following dispersion relation

$$\frac{c^2k^2}{\omega} + \chi\frac{\omega_{pi}^2}{\omega}\frac{(\omega + ku_0^{\parallel})}{\left(\omega + ku_0^{\parallel} \pm \Omega_{ci}\right)} + (1-\chi)\frac{\omega_p^2}{\omega}\frac{(\omega - \frac{\chi}{1-\chi}ku_0^{\parallel})}{\left(\omega - \frac{\chi}{1-\chi}ku_0^{\parallel} \pm \Omega_{ci}\right)} + \frac{(1+\sigma\sigma')}{2}\chi\frac{\omega_{pi}^2}{\omega}\frac{k^2u_0^{\perp 2}}{2}\left[\frac{1}{(\omega + ku_0^{\parallel} \pm \Omega_{ci})^2} + \frac{\frac{\chi}{1-\chi}}{(\omega - \frac{\chi}{1-\chi}ku_0^{\parallel} \pm \Omega_{ci})^2}\right] = \sigma'\frac{\omega_{pi}^2}{\Omega_{ci}} \tag{2.69}$$

where $\sigma, \sigma' \equiv \pm 1$ take into account the possible polarization of the waves with respect to the mean magnetic field direction and ω_{pi} is the ion plasma frequency.

Equation (2.69) can be written in dimensionless form in terms of a typical length scale $L_0 = c/\omega_{pi}$, a typical time scale $T_0 = 1/\Omega_{ci}$, and the corresponding parallel and perpendicular velocities $m_{\parallel,\perp} = \omega_{pi} u_0^{\parallel,\perp}/\Omega_{ci} c = u_0^{\parallel,\perp}/v_A$, where v_A is the Alfvén velocity. Therefore, the dimensionless dispersion relation in the above units becomes

$$\frac{k^2}{\omega} + \frac{\chi}{\omega}\frac{(\omega + k m_\parallel)}{\left(\omega + k m_\parallel + \sigma'\right)} + \frac{(1-\chi)}{\omega}\frac{(\omega - \frac{\chi}{1-\chi} k m_\parallel)}{\left(\omega - \frac{\chi}{1-\chi} k m_\parallel + \sigma'\right)} + \frac{(1+\sigma\sigma')}{2}\frac{\chi}{\omega}\frac{k^2 m_\perp^2}{2}\left[\frac{1}{(\omega + k m_\parallel + \sigma)^2} + \frac{\frac{\chi}{1-\chi}}{(\omega - \frac{\chi}{1-\chi} k m_\parallel + \sigma)^2}\right] = \sigma' \tag{2.70}$$

Figure 2.4 (upper panel) shows the dispersion relation $\omega_r(k)$ (in the electron reference frame) for $\chi = 0$ and $m_{\parallel,\perp} = 0$. As we expect from the HMHD description, we identify the four branches corresponding to the whistler ($W^{\pm}$) and the ion-cyclotron ($I^{\pm}$) modes. In particular, the $+$ and $-$ signs stand for the forward and backward propagation with respect to the magnetic field direction, respectively. In addition, two other solutions emerge, corresponding to the resonant (Res.) branches of the beam. Lower panel of Figure 2.4 shows the instability growth rate γ. Since $\chi = 0$, the beam instability is zero for all wavenumbers k. To understand the impact of considering a third species in the description, from equation (2.70) we will take two limiting cases: the field-aligned beam case ($m_\parallel \neq 0$ and $m_\perp = 0$) and the gyrating beam ($m_\perp \neq 0$ and $m_\parallel = 0$).

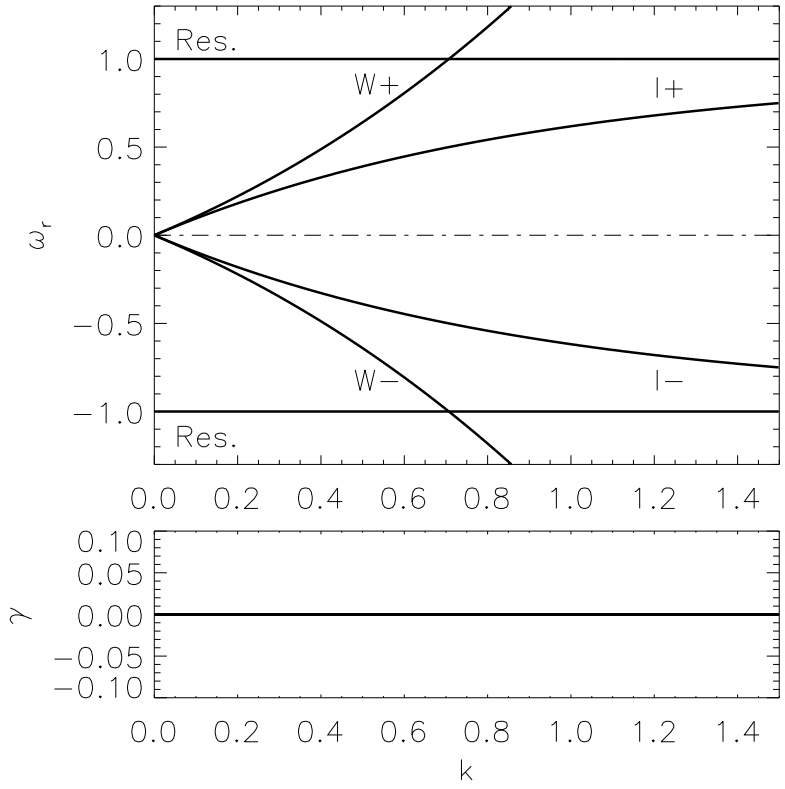

FIGURE 2.4: Upper panel shows the dispersion relation (in the electron frame) for the 6 solutions when $\chi = 0$, $m_\parallel = 0$ and $\sigma = \pm 1$. Four branches correspond to the whistler ($W^\pm$) and the ion-cyclotron ($I^\pm$) modes. The + and − signs stand for the forward and backward propagation to the magnetic field direction. The two linear solutions correspond to the resonant (Res.) branches of the beam. Lower panel shows the instability growth rate γ. Since $\chi = 0$, the beam instability is zero for all the wavenumbers.

2.4.1 Field-aligned beam limit

For the field-aligned beam limit, where $m_\parallel \neq 0$ and $m_\perp = 0$, the dispersion relation yields

$$\frac{k^2}{\omega} + \frac{\chi}{\omega}\frac{(\omega + km_\parallel)}{\left(\omega + km_\parallel + \sigma'\right)} + \frac{(1-\chi)}{\omega}\frac{(\omega - \frac{\chi}{1-\chi}km_\parallel)}{\left(\omega - \frac{\chi}{1-\chi}km_\parallel + \sigma'\right)} = \sigma', \tag{2.71}$$

a polynomial of order 3 for the frequency ω with real coefficients. Therefore, there are two types of possible solutions: either the three frequencies are real (and therefore no instabilities), or one frequency is real and the other two are complex

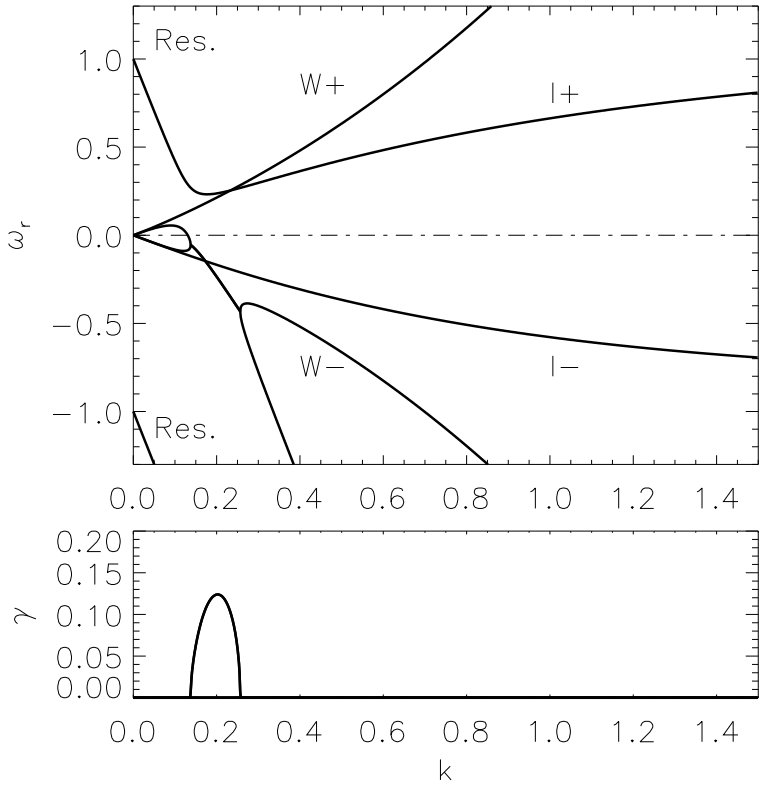

FIGURE 2.5: The dispersion relation (in the electron frame) for the field-aligned beam limit when $\chi = 5 \times 10^{-3}$, $m_{\parallel} = 6$ and $\sigma = \pm 1$. Lower panel shows the instability growth rate γ.

conjugate. In the latter, the complex solution with positive imaginary part corresponds to a growing instability, while the other complex solution corresponds to a damping solution.

Figure 2.5 (upper panel) shows the dispersion relation $\omega_r(k)$ (in the electron frame) for a beam speed of six times the Alfvén velocity, i.e. $m_{\parallel} = 6$, and a typical density at the Earth's foreshock [Narita et al., 2003]: $\chi = 5 \times 10^{-3}$. For those wave numbers where the linear resonant branch overlaps any of the other branches, we obtain a non-zero instability. In particular, in Figure 2.5 the backward whistler branch is the one being excited.

It is important to note that our calculation have been made in the electron frame, i.e. the solar wind frame. However, the observations made by Cluster (or any

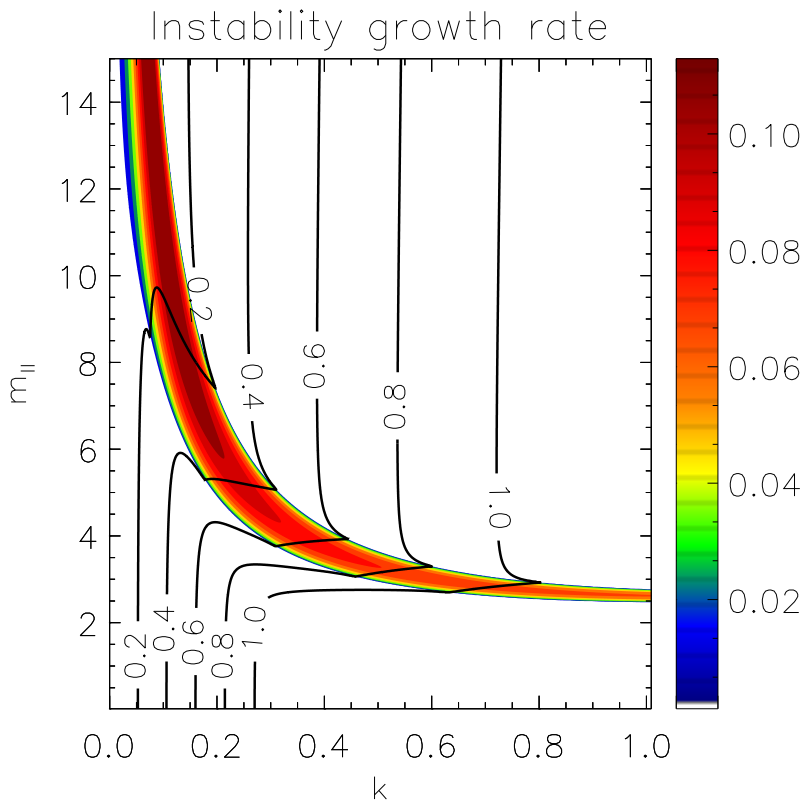

FIGURE 2.6: Colormap of the instabilities for the field-aligned beam limit. Contour levels correspond to different frequencies in the spacecraft frame.

other space mission) are in the spacecraft frame. Then, if we compared our theoretical predictions with the *in-situ* observations, we have to taking into account the transformation between reference frames. Therefore, we use the Doppler shift relation [Jackson, 1999]

$$\omega_{sw} = \omega_{sc} - \mathbf{k} \cdot \mathbf{u}_{sw}, \tag{2.72}$$

where ω_{sw}, ω_{sc}, and $\mathbf{u}_{sw}$ are the frequency in the plasma frame and in the spacecraft frame, and the solar wind flow velocity, respectively. This transformation can lead to a reversal in a wave's polarization in the new frame if $\omega_{sc} < 0$.

We now fix the beam density ($\chi = 5 \times 10^{-3}$) and vary the $m_{\parallel}$ value to study in the k-$m_{\parallel}$ parameter space the region where we expect to observe waves. Figure 2.6 shows a color map of the beam instabilities for different values of k and $m_{\parallel}$. Superimposed, contour levels of several frequencies are shown. Note that these

frequencies have been Doppler shift corrected using the equation (2.72). Then, if Cluster detects ULF waves with frequencies of the order of 0.2 rad/s (corresponding to $\sim$ 30 second period in the spacecraft frame) at long wavenumbers (i.e., $k << 1$), we would expect the beam velocities between ~ 7 and ~ 10 times the Alfvén velocity. In fact, this is the order of magnitude for the beam velocity at the Earth's bow shock [Narita et al., 2003]. We also note that an increment in the beam density χ yields an increment of the region of the beam instability in Figure 2.6.

2.4.2 Gyrating beam limit

The gyrating beam limit correspond to a proton beam with pure cyclotron motion, i.e. $m_\perp \neq 0$ and $m_\parallel = 0$. In this case, we assume that the relevant branches correspond to $\sigma = \pm 1$ and $\sigma' = \sigma$. We can actually do this simply because the case $\sigma' = -\sigma$ cancels the term with $m_\perp$. Therefore, in this limit equation (2.70) yields

$$\frac{k^2}{\omega} + \frac{1}{(\omega+\sigma)} + \frac{\chi}{1-\chi}\frac{m_\perp^2}{2}\frac{k^2}{\omega(\omega+\sigma)^2} = \sigma. \tag{2.73}$$

Once again, equation (2.73) is a polynomial of order 3 for the frequency ω with real coefficients. However, in this limit, the polynomial only depends on the ratio $M \equiv \chi m_\perp^2/2(1-\chi)$. Figure 2.7 shows the dispersion relation for $M = 2$. As we discussed in the previous Section, for those wave numbers where the linear resonant branch overlaps any of the other branches, an unstable branch can arise. In particular, in Figure 2.7 the forward and backward ion cyclotron branches are being excited.

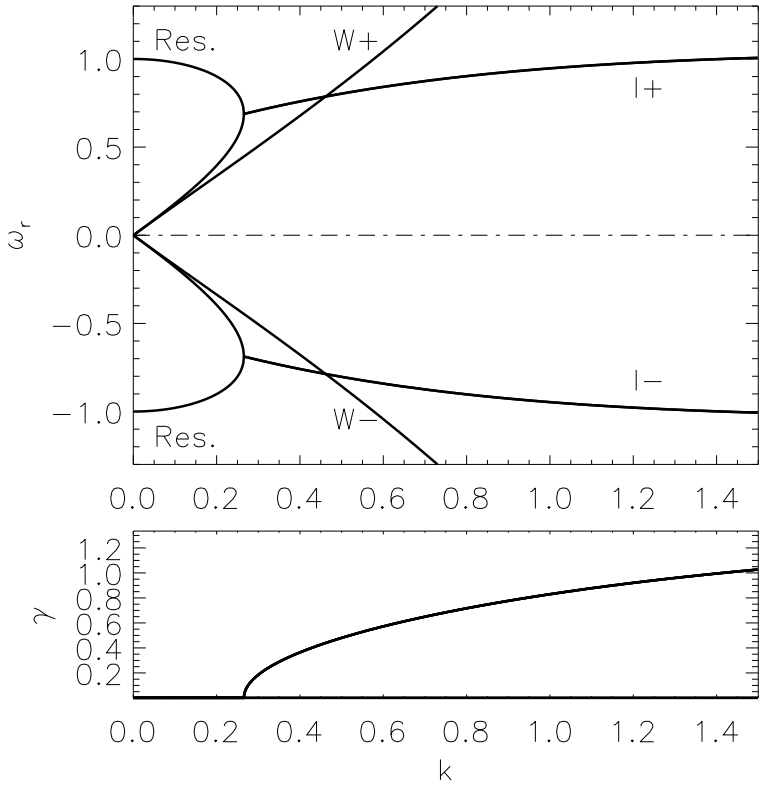

FIGURE 2.7: The dispersion relation (in the electron frame) for the pure cyclotron motion when $M \equiv \chi m_\perp^2/2(1-\chi) = 2$. Lower panel shows the instability growth rate γ.

For a fixed beam density ($\chi = 5\times10^{-3}$), we study the region in the k-M parameter space in which we expect to observe waves. Figure 2.8 shows a color map of the instabilities for different k and M values. As in Figure 2.6, we superimposed contour levels of different frequencies in the spacecraft frame. These contour levels of frequencies have been corrected by the Doppler shift using the equation (2.72). In contrast with the field-aligned beam, the gyrating beam predicts waves with slightly higher frequencies ($\sim$ 1 rad/s) than those observed in the upstream solar wind at 1 AU ($\sim$ 0.1-0.5 rad/s), and perpendicular beam velocity which are not compatible with the results report in the literature ($\sim$ 350 km/s in the electron reference frame, which implies $M \sim 0.03$) [Narita et al., 2003].

In conclusion, in our foreshock scenario, a fraction of the upstream proton population is reflected at the shock (for a discussion of different acceleration mechanisms

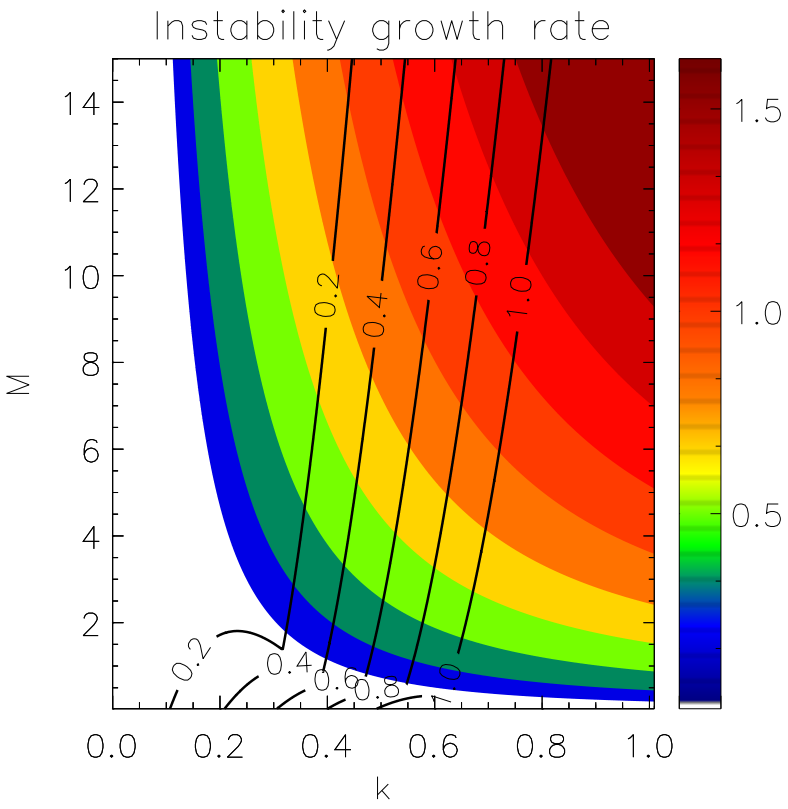

FIGURE 2.8: Colormap of the instabilities for the ring limit. Contour levels correspond to different frequencies in the spacecraft reference frame.

at the shock, see the next Section), generating ULF foreshock waves by means of this beam-driven instabilities. Under parallel propagation of the beam and adequate solar wind conditions, we expect waves to be generated upstream from, for instance, the Earth's bow shock [e.g. Eastwood et al., 2003]. Finally, in a three-fluid description, we show that it is possible to obtain actual physical wave instabilities, which are not present in the one- and two-fluid description. However, a detailed comparison of these theoretical predictions with in-situ measurements is beyond the scope of the present Thesis.

2.5 Acceleration mechanisms at the shock

In the present section, we study the possible ion acceleration mechanisms present at planetary bow shocks. In particular, we are going to focus on three different particle emission mechanisms discussed in the literature, the so-called magnetosheath particle leakage, the adiabatic reflection and the specular reflection model. These acceleration models bear a direct relation with the bow shock geometry [e.g. Thomsen et al., 1983], i.e. the angles θ_{Vn} and θ_{Bn} between the incoming solar wind velocity and the magnetic field, respectively.

For the present calculation, the most convenient frame of reference is the so-called de Hoffman-Teller (HT) frame [de Hoffman and Teller, 1950] (see Figure 2.9). If we consider an upstream bulk solar wind velocity $\mathbf{u}_i$ from the bow shock, a mean upstream magnetic field $\mathbf{B}$ and a shock normal $\hat{\mathbf{n}}$, the transformation velocity from the spacecraft (s/c) frame to the HT frame is

$$\mathbf{v}_{\mathrm{HT}} = \frac{\hat{\mathbf{n}} \times (\mathbf{u}_i \times \mathbf{B})}{\mathbf{B} \cdot \hat{\mathbf{n}}} \tag{2.74}$$

Since the shock is at rest in the HT frame, the induced electric field is equal to zero. Thus, in this particular frame the total energy of the particles is conserve (even when we include an electric potential $\Delta\phi$ across the shock surface). Finally, since in the HT frame the upstream velocity is parallel to the magnetic field, the 3D problem is reduced to a 2D problem in the $\mathbf{B}$-$\hat{\mathbf{n}}$ plane [Schwartz et al., 1983].

For the classification of emission mechanisms, we consider an upstream particle which leaves the shock with a velocity $\mathbf{u}_0'$ in the HT frame. This velocity can be decomposed into a guiding center motion along $\mathbf{B}$, $u_{\parallel} = \mathbf{u}_0' \cdot \hat{\mathbf{b}}$ (where $\hat{\mathbf{b}} \equiv \mathbf{B}/B$ is the magnetic field direction), and a gyromotion about $\mathbf{B}$, $v_g = |\mathbf{u}_0' - u_{\parallel}'\hat{\mathbf{b}}|$ [Schwartz

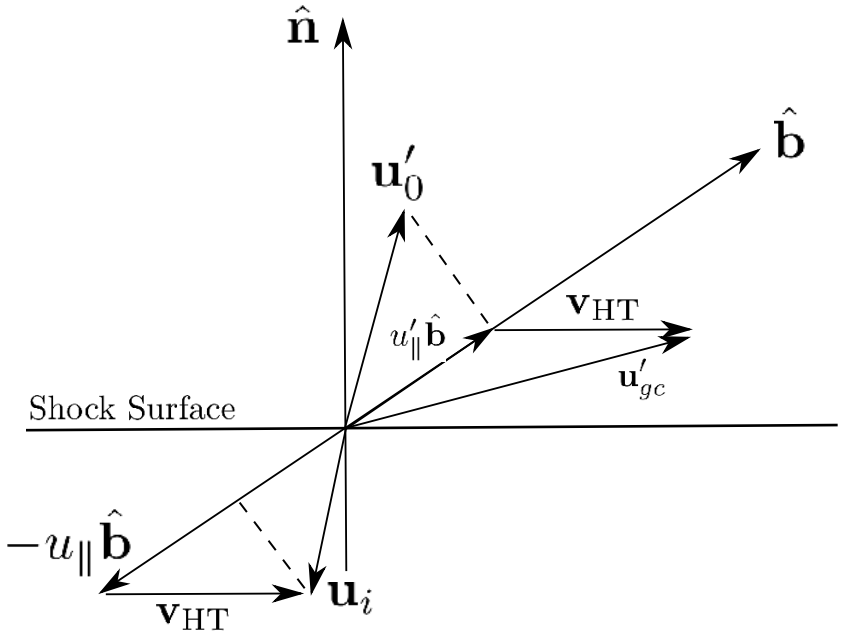

FIGURE 2.9: The de Hoffman-Teller frame.

et al., 1983]. Finally, the particle velocity in the s/c frame is

$$\mathbf{u}_{s/c} = \mathbf{u}'_0 + \mathbf{v}_{\mathrm{HT}} \tag{2.75}$$

where $\mathbf{v}_{\mathrm{HT}}$ was define in equation (2.74). Therefore, according to different hypothesis about the origin of these backstreaming particles, we are going to calculate the respectively exit velocity from the shock in the HT frame, i.e. $\mathbf{u}'_0$. Finally, we can transform the different exit velocities to the s/c or the plasma reference frame and compare them with the measurements. As we discuss above, the main shock acceleration mechanisms to consider are the magnetosheath particle leakage, the adiabatic reflection and the specular reflection.

2.5.1 Magnetosheath particle leakage

Edmiston et al. [1982] studied the presence of upstream distributions which have leaked from the magnetosheath conserving their magnetic moment. In order to escape to the upstream region, these magnetosheath particles must at least reach

the speed of the bow shock, which can be regarded as a threshold. Then, the predicted normalized velocity in the HT frame is

$$u'_{\parallel} = u_i \cos(\theta_{Vn}) \tag{2.76}$$

where $|\mathbf{u}_i| = u_i$ is the incident solar wind velocity. This velocity transforms to the plasma reference frame as

$$\left(\frac{u_{\parallel}}{u_i}\right)_{m.l.} = \frac{\cos(\theta_{Vn})}{\cos(\theta_{Bn})}. \tag{2.77}$$

In particular, this process may explain the observation of low energy ion beams [Edmiston et al., 1982, Tanaka et al., 1983, Thomsen et al., 1983].

2.5.2 Adiabatic reflection

In the adiabatic reflection model, a portion of the incoming solar ions produces an ion beam aligned with the IMF with generally high energies [Sonnerup, 1969, Thomsen et al., 1983]. The reflected ions acquire a speed in the HT frame

$$u'_{\parallel} = u_i \frac{\cos(\theta_{Vn})}{\cos(\theta_{Bn})} \tag{2.78}$$

which transforms to the plasma reference frame as

$$\left(\frac{u_{\parallel}}{u_i}\right)_{a.r.} = 2\frac{\cos(\theta_{Vn})}{\cos(\theta_{Bn})} \tag{2.79}$$

where, again, is $u_{\parallel}$ is normalized to u_i.

2.5.3 Specular reflection

Specular reflection of a portion of the solar wind ions gives birth to an acceleration mechanism in the upstream region only when $\theta_{Bn} < 45°$ [Schwartz et al., 1983]. Incident solar wind ions simply reverse their component of velocity parallel to the shock normal [Thomsen et al., 1983]. In this case the post-encounter parallel velocity in the plasma reference frame (normalized to u_i) is given by

$$\left(\frac{u_{\parallel}}{u_i}\right)_{s.r.} = 2\cos(\theta_{Vn})\cos(\theta_{Bn}) \tag{2.80}$$

In the present Thesis, we compare these normalized velocities with the foreshock boundary properties derived from the analysis of in-situ measurements (see Chapter 5).

2.6 Resumen en castellano

En este Capítulo presentamos las principales herramientas teóricas utilizadas a lo largo de la Tesis.

En la sección 2.1, presentamos las ecuaciones del modelo de multi-fluidos para plasmas y los invariantes ideales de este sistema de ecuaciones.

En la sección 2.2, presentamos una descripción detallada de la derivación de las ecuaciones del modelo de dos fluidos MHD. Considerando un plama formado por protones y electrones (con masa), este modelo contiene tanto el efecto Hall como la inercia electrónica.

En la sección 2.3, presentamos el cálculo detallado para hallar modelos normales de oscilación. En particular, calculamos los modos normales para el modelo de dos fluidos MHD, graficamos la relación de dispersión y el diagrama polar de velocidades.

En la sección 2.4, consideramos un plasma formado por tres especies: un fondo de protones, un fondo de electrones (sin masa) y una tercera especie formada por un haz (*beam*) de protones mucho menos denso. Calculamos los modos normales de oscilación de este sistema de tres fluidos y mostramos la posibilidad de tener inestabilidades de plasma. En particular, estudiamos dos límites para la velocidad del haz: el *field-aligned beam* (haz alineado al campo magnético) y *gyrating beam* (haz con componente de velocidad perpendicular al campo magético).

Finalmente, en la sección 2.5, presentamos tres modelos de aceleración presentes en choques planetarios. Estos tres modelos son los más referidos en la literatura y se presume que son los responsables de generar los haces de protones que se reflejan en los choques planetarios. En particular, presentamos el goteo de partículas

en la magnetofunda (*magnetosheath particle leakage*), la reflexión adiabatica y la reflexioón especular.

Chapter 3

Solar wind turbulence

A Plinio (historia natural, libro octavo) no le basta observar que los dragones atacan en verano a los elefantes: aventura la hipótesis de que lo hacen para beberles toda la sangre que, como nadie ignora, es muy fría.

Las alarmas del doctor Américo Castro. Jorge Luis Borges

According to the EIHMHD description, each plasma species introduces new spatial scales: the ion inertial length λ_i and the electron inertial length λ_e, which are not present in the traditional MHD description. In this Chapter, we seek for possible changes in the energy power spectrum for fully developed turbulent regimes. We are able to reproduce different scaling laws in different spectral ranges, as it has been observed in the solar wind for the magnetic and electric energy spectra. For small wavenumbers, where one-fluid MHD is asymptotically valid, we obtain an inertial range following a Kolmogorov $k^{-5/3}$ law. For intermediate wavenumbers such that $\lambda_i^{-1} << k << \lambda_e^{-1}$, the spectrum is modified to a $k^{-7/3}$ power-law, as observed also in HMHD approaches neglecting electron inertia terms. When electron inertia is retained, a new spectral region given by $k > \lambda_e^{-1}$ arises. The

power spectrum for magnetic energy in this region is given by a $k^{-11/3}$ power law. Finally, in this approaches, we study the self-consistent electric field.

3.1 Energy cascade

As it was discussed, an important feature to characterize a stationary and isotropic turbulent regime of an incompressible plasma is its energy spectrum $E(k)$, which provides the energy per unit wavenumber. At MHD scales, the energy spectrum follows a $k^{-5/3}$ scaling, i.e. a Kolmogorov spectrum, just as for neutral fluids. This power law was predicted by Kolmogorov [1941] for hydrodynamic turbulence (assuming isotropy and using dimensional analysis). However, one fundamental difference between hydrodynamic and plasma turbulence is the presence of different wavenumber regimes with their corresponding power law dependencies. In the present Chapter, we study changes in the energy power spectrum in fully developed turbulent regimes, taking into account the presence of the Hall current and electron inertia. We also compared our numerical results with solar wind in-situ measurements.

In Section 2.3, we calculated the ideal invariants, i.e. the total energy and the electron and proton helicities. In particular, for an EIHMHD description, the dimensionless version of the total energy is

$$E = \int d^3r \Big(\frac{u^2}{2} + \frac{B^2}{2} + (1-\mu)\mu\lambda^2\frac{j^2}{2}\Big). \tag{3.1}$$

This quantity is a quadratic and global ideal invariant. For instance, the energy density

$$E(\mathbf{r},t) = \frac{u^2}{2} + \frac{B^2}{2} + (1-\mu)\mu\lambda^2\frac{j^2}{2}\ , \tag{3.2}$$

satisfies the following evolution equation in the absence of dissipation

$$\frac{\partial}{\partial t}E(\mathbf{r},t) = -\boldsymbol{\nabla}\cdot\mathbf{F}\ , \tag{3.3}$$

where $\mathbf{F}$ is the energy flux. Since the energy density (3.2) is quadratic, an equation equivalent to (3.3) also holds in Fourier space as a result of Parseval's theorem. In a stationary and isotropic turbulent regime, the so-called energy cascade corresponds to a constant energy flux in Fourier space (i.e., $\mathbf{F}_k$ independent of $k = |\mathbf{k}|$).

In the paradigmatic case of incompressible hydrodynamic turbulence, a stationary and isotropy turbulent regime can arise as the result of an isotropic driving force injecting energy at large scales (energy-contain region), the cascade of energy throughout a whole range of intermediate scales (energy inertia region) and the viscous dissipation at sufficiently small spatial scales (dissipative region). The modulus of the energy flux in Fourier space given by

$$F_k \simeq k u_k^3 = \epsilon \tag{3.4}$$

which leads to the well known Kolmogorov's energy power spectrum

$$E_k \simeq \epsilon^{2/3} k^{-5/3} \tag{3.5}$$

for isotropic, stationary and incompressible turbulence. This is obtained using that $E_k \simeq u_k^2/\tau_k$ and $\tau_k \simeq (k u_k)^{-1}$. The Kolmogorov spectrum is valid throughout the energy inertia region, with ϵ being the energy fluxrate. In stationary regime, ϵ is also the energy dissipation rate and the injection rate.

In the more complex case of EIHMHD turbulence, there are many terms contributing to the energy flux in both physical and Fourier spaces. These various contributions are sketched in the following expression for the energy flux in Fourier

space,

$$F_k \simeq k(u_k^3 + u_k B_k B_k' + (1-\mu)\lambda J_k B_k B_k' + (1-\mu)\mu\lambda^2 \partial_t J_k B_k) \tag{3.6}$$

The presence in EIHMHD of the physical lengthscales associated with each species (i.e. $k_{i,e} = \lambda_{i,e}^{-1}$) causes the appearance of three different regions in wavenumber space.

I) The MHD region ($k \lesssim k_i$): In this region we assume $\lambda \approx \mu \approx 0$ and also $u_k \simeq B_k \simeq B_k'$. Therefore $F_k \simeq k B_k^3 = \epsilon$ and $E_k \simeq B_k^2/k \simeq \epsilon^{2/3} k^{-5/3}$.

II) The HMHD region ($k_i \lesssim k \lesssim k_e$): In this region we maintain $\mu \approx 0$ but $\lambda \neq 0$, and $u_k \lesssim B_k \simeq B_k'$. As a result, we now have $F_k \simeq \lambda k^2 B_k^3 = \epsilon$ and therefore $E_k \simeq B_k^2/k \simeq (\epsilon/\lambda)^{2/3} k^{-7/3}$.

III) The EIHMHD region ($k_e \lesssim k$): This large-k region is dominated by the last two terms in equation (3.6), which reduces to $F_k \simeq k\mu\lambda^2 \partial_t J_k B_k = \epsilon$ since $B_k' \sim \mu\lambda^2 k^2 B_k >> B_k$. Since $k\lambda \gtrsim 1/\sqrt{\mu} >> 1$ we assume the ions to remain static because of their much larger mass and the dynamics to be dominated by the electrons, i.e., $\partial_t \simeq k u_{ek} \simeq \lambda k^2 B_k$. Therefore $F_k \simeq \mu\lambda^3 k^4 B_k^3 = \epsilon$. Note that the energy power spectrum in this region is now predominantly electron kinetic energy, and therefore $E_k \simeq \mu\lambda^2 J_k^2/k \simeq (\epsilon^2\mu)^{1/3} k^{-5/3}$. The power spectrum of magnetic energy, however, is equal to $B_k^2/k \simeq (\epsilon/(\mu\lambda^3))^{2/3} k^{-11/3}$.

Therefore, the power spectrum of magnetic energy, i.e. $S_B(k)$, has different slopes according to these different spatial regions. In summary, $S_B(k) \sim k^{-5/3}$ in the MHD region, $S_B(k) \sim k^{-7/3}$ in the HMHD region and, finally, $S_B(k) \sim k^{-11/3}$ in the EIHMHD region.

3.2 2.5D Setup and initial conditions

To study the properties of a fully developed turbulent state in EIHMHD, we consider a 2.5D setup. In this particular setup, the vector fields have all three components, but only depend on two (for instance, the x and y Cartesian coordinates). As we are considering the incompressible case ($\boldsymbol{\nabla} \cdot \mathbf{u} = \mathbf{0}$) we can write the magnetic and velocity fields as

$$\mathbf{B} = \boldsymbol{\nabla} \times [\hat{\mathbf{z}} a(x,y,t)] + \hat{\mathbf{z}} b(x,y,t) \tag{3.7}$$

$$\mathbf{u} = \boldsymbol{\nabla} \times [\hat{\mathbf{z}} \varphi(x,y,t)] + \hat{\mathbf{z}} u(x,y,t) \tag{3.8}$$

where $a(x,y,t)$ and $\varphi(x,y,t)$ are respectively the vector potential and stream function and $b(x,y,t)$ and $u(x,y,t)$ are the $\hat{\mathbf{z}}$-component of the magnetic and velocity field. In terms of these functions, the equations (2.25) and (2.29) become:

$$\begin{aligned} \partial_t\, \omega &= [\varphi, \omega] - [a, j] - (1-\mu)\mu\lambda^2 [b, \nabla^2 b] + \\ &+ \nu \nabla^2 \omega - \nu_0 \lambda \nabla^4 b \end{aligned} \tag{3.9}$$

$$\begin{aligned} \partial_t\, u &= [\varphi, u] - [a, b] - (1-\mu)\mu\lambda^2 [j, b] + \nu \nabla^2 u + \\ &+ \nu_0 \lambda \nabla^2 j \end{aligned} \tag{3.10}$$

$$\begin{aligned} \partial_t\, a' &= [\varphi_e, a'] + \eta \nabla^2 a - (1-\mu)\nu_e \lambda^2 \nabla^4 a - \\ &- \nu_e \lambda \nabla^2 u \end{aligned} \tag{3.11}$$

$$\begin{aligned} \partial_t\, b' &= [\varphi_e, b'] + [u_e, a'] + \eta \nabla^2 b - (1-\mu)\nu_e \lambda^2 \nabla^4 b - \\ &- \nu_e \lambda \nabla^2 \omega \end{aligned} \tag{3.12}$$

where

$$\omega = -\nabla^2\varphi \tag{3.13}$$

$$j = -\nabla^2 a \tag{3.14}$$

$$a' = a + \mu(1-\mu)\lambda^2 j - \mu\lambda u \tag{3.15}$$

$$b' = b - \mu(1-\mu)\lambda^2\nabla^2 b - \mu\lambda\omega \tag{3.16}$$

and the nonlinear terms are all given by the standard Poisson brackets, i.e.

$$[p,q] \equiv \partial_x p \partial_y q - \partial_y p \partial_x q. \tag{3.17}$$

We have also defined the stream function and the velocity component along $\hat{\mathbf{z}}$ for electrons, respectively as

$$\varphi_e = \varphi - (1-\mu)\lambda b \tag{3.18}$$

$$u_e = u - (1-\mu)\lambda j. \tag{3.19}$$

This set of equations describes the dynamical evolution of the magnetic and velocity fields. When $\mu = 0$ (i.e. $m_e = 0$) it reduces to the incompressible 2.5D HMHD equations. Finally, since in the 2.5D setup $\partial_z \equiv 0$ we can ignore the $g(\mathbf{r},t)$ indetermination in equation (2.32) for the computation of E_z.

We use a parallel pseudospectral code to numerically integrate equations (3.9)-(3.12). A second-order Runge-Kutta time-integration scheme is adopted. Periodic boundary conditions are assumed for the $\hat{\mathbf{x}}$ and $\hat{\mathbf{y}}$ directions of a square box of linear side $2\pi L_0$ (where L_0 is the length unit). The simulations performed throughout the present Chapter are run-down, i.e., they do not contain any magnetic or velocity stirring forces. As initial conditions, we excite Fourier modes (for both magnetic and velocity field fluctuations) in a shell in k-space with wavenumbers

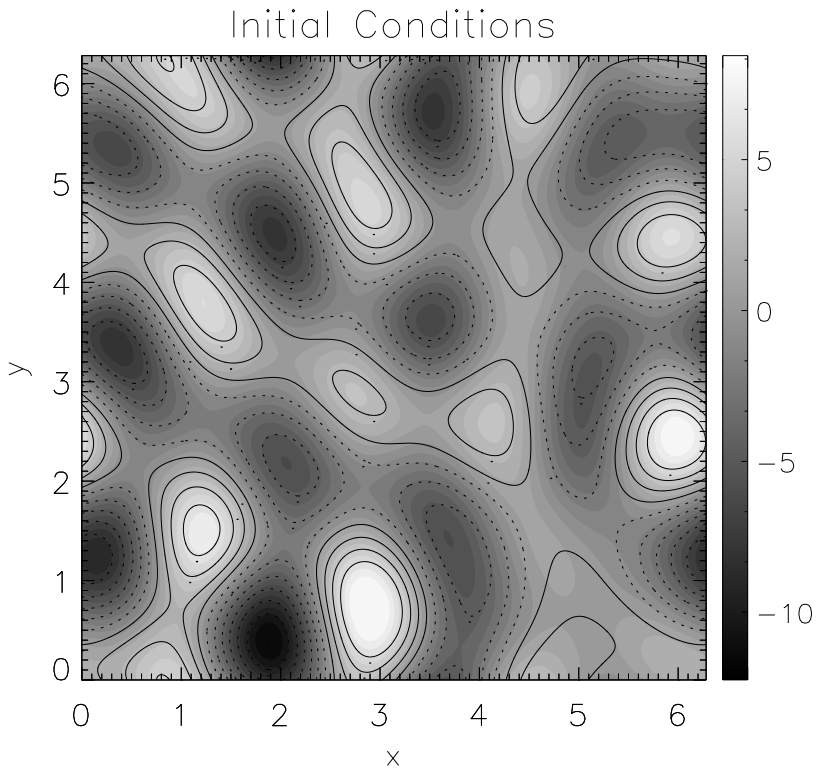

FIGURE 3.1: The images (in redscale) show the spatial distribution of current density $j(x, y)$ at $t = 0$, for the integration box $(2\pi \times 2\pi)$. Contours of $a(x, y)$ are superimposed (solid and dashed black lines for $a > 0$ and $a < 0$, respectively).

$3 \leq k \leq 4$, with the same amplitude and random phases for all modes. Figure 3.1 shows the spatial distribution of current density $j(x, y)$ at $t = 0$ in a red-scale for the integration box. In addition, contours of $a(x, y)$ are superimposed in white lines. For all the simulations of this chapter we used a spatial resolution of 3072^2 grid points with $\nu = 3 \times 10^{-5}$ and $\eta = 1.5 \times 10^{-4}$. To suppress aliasing effects, our spectral code uses a maximum wavenumber $k_{max} = N/3 = 1024$. The ratio between the ion and electron inertial lengths is equal to the square root of the mass ratio. For instance, for the realistic value $m_e/m_p = 1/1836$, which corresponds to $k_e \sim 43k_i$, the dissipation range corresponds to wavenumbers much larger than both characteristic scales. For all simulations, the dissipation wavenumber k_d, computed as $k_d =< j^2 + \omega^2 >^{1/4} /\sqrt{\nu}$, remains in the range of $k_e < k_d < k_{max}$.

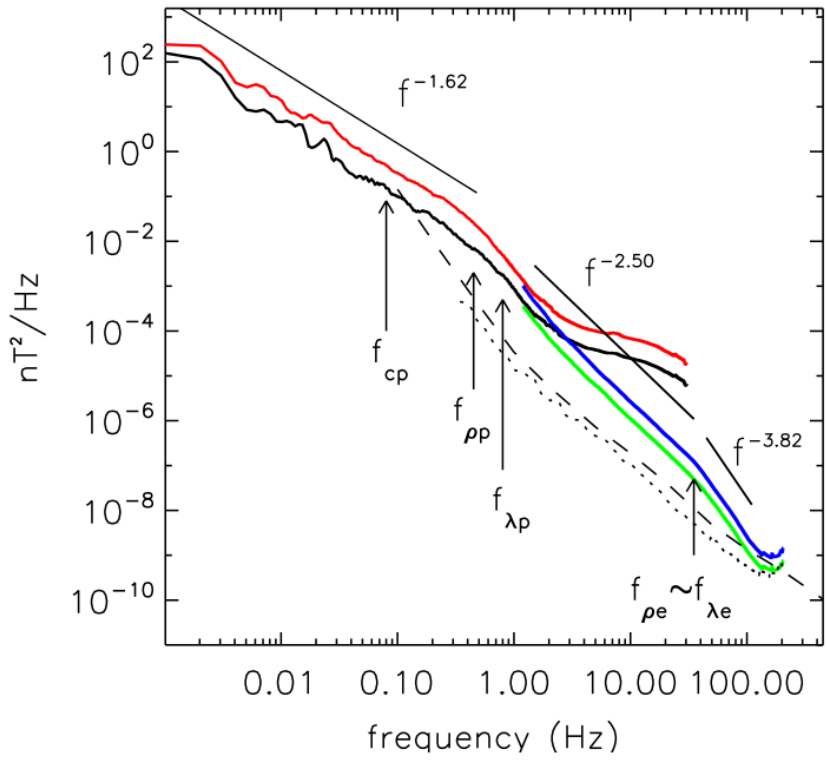

FIGURE 3.2: The parallel (black) and perpendicular (red) magnetic spectra of Cluster data. The noise level measured in the laboratory and in-flight are plotted as dashed and dotted lines, respectively. The straight black lines are power law fits to the spectra. The arrows indicate characteristic frequencies defined in the text [Extracted from Sahraoui et al., 2009].

3.3 Interplanetary magnetic field spectrum

Figure 3.2 shows the parallel (black-green lines) and perpendicular (red-blue lines) magnetic field spectra from in-situ solar wind Cluster measurements [Sahraoui et al., 2009]. The noise level measured in the laboratory and in flight are plotted as dashed and dotted lines, respectively. The solid black lines are power law fits to the spectra. The arrows indicate the characteristic scales of the plasma, namely, the proton and electron gyro-scales ($\rho_{p,e} \equiv v_{th_{p,e}}/\omega_{cp,e}$, where v_{th} and $\omega_{cp,e}$ are the thermal velocity and the proton and electron gyro-frequency).

We ran simulations at high spatial resolution to study the freely evolving turbulence at different scales. In particular, we performed two EIHMHD simulations

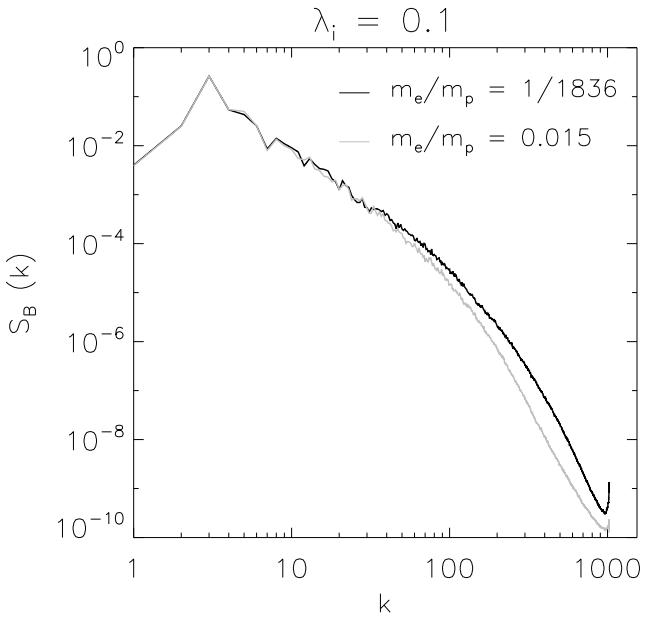

FIGURE 3.3: Magnetic energy spectra for EIHMHD cases with $\lambda_i = 1/10$, $m_e/m_p = 1/1836$ (black) and $m_e/m_p = 0.015$ (gray).

with the same ion inertial length ($\lambda_i = 0.1$) and different electron to proton mass ratios (m_e/m_p). On one hand, we used a fictitious mass ratio, $m_e/m_p = 0.015$ (electrons 27 times heavier), which corresponds to $k_i \sim 10$ and $k_e \sim 82$ to study the development of scales between the electron and the ion inertial lengths. On the other hand, we used the real mass ratio $m_e/m_p = 1/1836$ corresponding to $k_i \sim 10$ and $k_e \sim 428$.

Figure 3.3 shows the magnetic energy spectrum for both runs. The black and gray lines correspond to the real and fictitious electron-to-proton-mass ratio, respectively. As shown by the spectra, the magnetic power spectra explicitly depends on the value of the electron mass, even though asymptotically goes to the HMHD spectrum as $k << k_e$.

The upper panel in Figure 3.4 shows the magnetic energy spectra for the case of fictitious electron to proton mass ratio (gray line). In addition, the dashed black lines show the theoretical power-law scalings (see section 3.1) for the different spectral ranges. The ion, electron and dissipation wavenumbers are indicated as

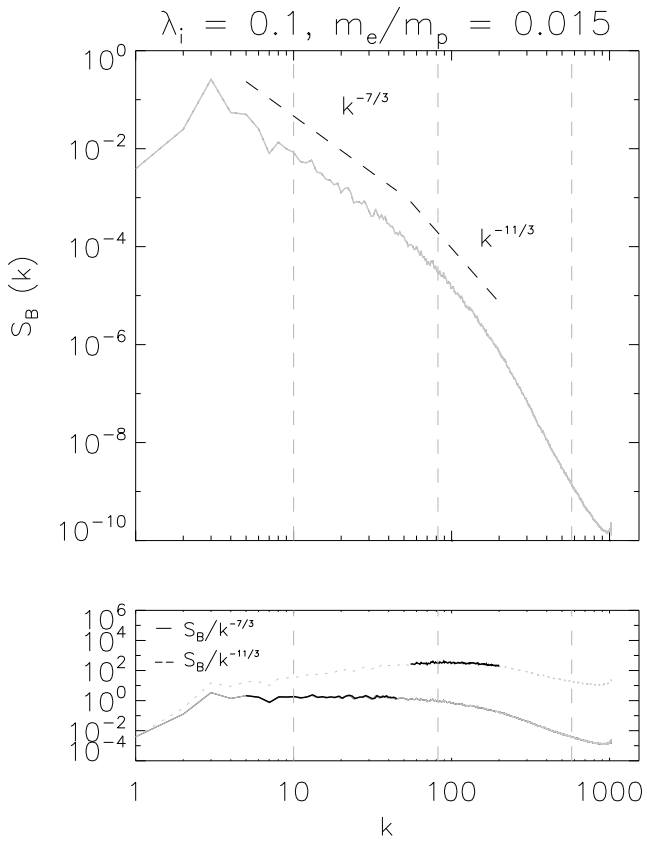

FIGURE 3.4: Magnetic energy spectra for $m_e/m_p = 0.015$. Vertical dashed gray lines correspond to $k_i \sim 10$, $k_e \sim 82$ and $k_\nu \sim 550$. The compensated spectrum for the HMHD (solid line) and EIHMHD (dashed line) regions are shown in the lower panel.

vertical dashed gray lines. The lower panels show the compensated spectrum for the HMHD (solid line) and EIHMHD (dashed line) region. The separation points occur near the kinetic scales k_i and k_e, a feature consistent with solar wind observations [Sahraoui et al., 2009, Alexandrova et al., 2009]. It is also remarkable the very good agreement between he theoretical and numerical slopes for each region. In Figure 3.4, the scale separation between the HMHD and the EIHMHD regions is clearly noticeable. The Hall range shows a scaling of $\sim k^{-7/3}$, in agreement with observations, several theoretical predictions [Galtier, 2006, Biskamp et al., 1999] and previous numerical results [Krishan and Mahajan, 2004, Gómez et al., 2008]. A new range of scaling $\sim k^{-11/3}$ emerges for wavenumbers $k \sim k_e$, i.e. the EIHMHD region, which is also consistent with our prediction described in section

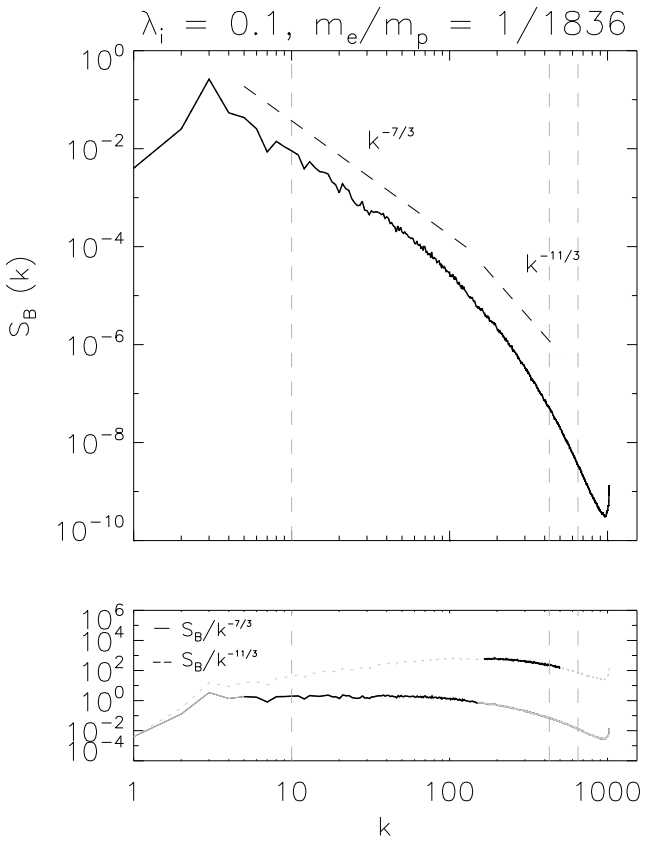

FIGURE 3.5: Magnetic energy spectra for $m_e/m_p = 1/1836$. Vertical dashed gray lines correspond to $k_i \sim 10$, $k_e \sim 430$ and $k_\nu \sim 650$. The compensated spectrum for the HMHD (gray line) and EIHMHD (green line) regions in the same format as Figure 3.4.

3.1, solar wind observations [Sahraoui et al., 2009, Alexandrova et al., 2009] and previous simulations [Sahraoui et al., 2009, Wan et al., 2012]. There is also an indication of an exponential decay for the largest wavenumbers in our simulations, as was suggested by observations [Alexandrova et al., 2009].

Figure 3.5 shows the power spectra for the magnetic energy for $m_e/m_p = 1/1836$ (black line), with the same format as Figure 3.4. In this case, the inverse of the electron inertial length and the dissipation wavenumber are very close to each other. Therefore, there is no clear-cut distinction between the $k^{-11/3}$ power-law and the exponentially decaying dissipative region.

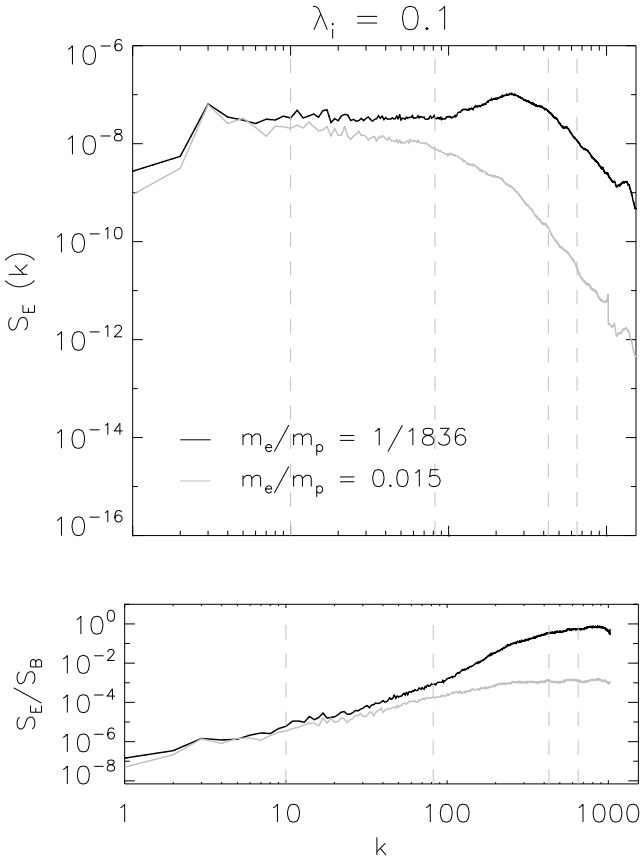

FIGURE 3.6: Power spectrum of electrostatic field for EIHMHD with $m_e/m_p = 1/1836$ and $m_e/m_p = 0.015$ (upper panel). Vertical lines correspond to $k_i \sim 10$, k_e ($\sim$ 82 and $\sim$ 428 for the fictitious and real mass ratio respectively) and $k_\nu \sim 650$. The lower panel, corresponds to the ratio between the electric and magnetic spectra, i.e. S_E/S_B.

3.4 Interplanetary electric field spectrum

As we show in Chapter 2, making use of the Maxwell-Faraday equation in Fourier space we can obtain an expression for the electric field **E**, see (2.32). Figure 3.6 (upper panel) shows the power spectrum of the z component of the electric field for the two EIHMHD cases, $m_e/m_p = 1836$ (black) and $m_e/m_p = 0.015$ (gray). The ion wavenumber ($k_i \sim 10$), the fictitious and real electron wavenumbers ($k_e \sim 82$ and $k_e \sim 482$, respectively) and the dissipation scale ($k_d \sim 650$) wavenumber are indicated as vertical dashed gray lines. The two spectra are clearly different when we consider electrons with different masses. As we expect, the electric field is

much smaller than the magnetic field for all scales($\sim 10^{-8}$ in the large scales and $\sim 10^{-2}$ in the small scales).

The lower panel shows the ratio between the electric field (z component) and the magnetic field spectra. We find that the electric field becomes gradually more important as k increases. This is consistent with observations in the solar wind [Sahraoui et al., 2009].

3.5 Discussion

Within the context of a full two-fluid model in a turbulent regime we numerically obtain the magnetic energy spectrum, which present striking similarity consistent with the one observed in the solar wind. The energy inertia region of the spectrum is split into three subregions as a result of the presence of the new spatial scales λ_i and λ_e. This is explicitly shown in equations (3.9)-(3.12) where it can be seen that the presence of the scales λ_i and λ_e introduces new non-linear terms which are absent in a one-fluid MHD description. It is worth mentioning that these new regions originated by the appearance of two physically meaningful spatial scales (i.e., $\lambda_{i,e}$) are not present in the one-fluid MHD description.

We also present numerical results for the electric field. It is worth mentioning that the interplanetary electric field consists of four different contributions. An inductive part related to the $\mathbf{u} \times \mathbf{B}$ term, a Hall contribution related to $\lambda_i \mathbf{j} \times \mathbf{B}$ term, the dissipative component and a new contribution associated with the non-zero electron mass, which is proportional to μ. As a consequence, these nonlinear contributions affect the energy distribution among scales. If the energy distribution is affected by introducing these two effects (Hall and non-zero electron mass), we can expect also different flow structures and general dynamics on small-scales where the one-fluid MHD description is no longer adequate.

3.6 Resumen en castellano

En este Capítulo presentamos los resultados y discusiones referidos al carácter turbulento del viento solar.

En la sección 3.1, presentamos las predicciones teóricas para el espectro de energía magn ética para cada región en el espacio de número de onda. En particular, hallamos el espectro para grandes escalas temporales y espaciales (MHD), las escalas intermedias (HMHD) y las escalas pequeñas (EIHMHD). Además, presentamos los pricipales resultados de mediciones in-situ del viento solar a una unidad astronómica.

En la sección 3.2, presentamos las condiciones iniciales para estudiar numericamente la turbulencia en el viento solar. Además, introducimos las ecuaciones en 2.5 D, las cuales serán utilizadas también en el Capítulo 4.

En las secciones 3.3 y 3.4 presentamos los resultados numéricos principales y los comparamos con las predicciones teóricas y las mediciones in-situ en el viento solar.

Finalmente, en la sección 3.5, presentamos las discusiones y conclusiones del Capítulo.

Chapter 4

Collisionless Magnetic Reconnection

Los niños debían de recordar por el resto de su vida la augusta solemnidad con que su padre se sentó a la cabecera de la mesa templado de fiebre, devastado por la prolongada vigilia y por el encono de su imaginación, y les revelo su descubrimiento: — La tierra es redonda como una naranja.

Cien años de soledad. Gabriel Garcia Marquez.

In this Chapter, we briefly review the earlier results about magnetic reconnection within the framework of one-fluid resistive MHD. Then, we present a study of collisionless magnetic reconnection within the framework of EIHMHD for a completely ionized hydrogen plasma, retaining the effects of the Hall current, electron pressure and electron inertia. We performed 2.5D simulations using a pseudo-spectral code with no dissipative effects. Our numerical results confirm that the change in the topology of the magnetic field lines is exclusively due to the presence of electron inertia. The computed reconnection rates remain a fair fraction of the Alfvén velocity, which therefore qualifies as fast reconnection. The dimensionless EIHMHD

equations, present two relevant dimensionless constants: the Hall parameter and the mass ratio. We conduct two series of simulations varying each one of these parameters. We find that while the reconnection rate remains independent of the mass ratio, it increases linearly with the Hall parameter.

4.1 Resistive magnetic reconnection: the Sweet-Parker model

Magnetic reconnection is a physical process that converts magnetic free energy into heat and kinetic energy. This important mechanism of energy conversion is present in several space environments, such as solar flares and planetary magnetospheres [Priest and Forbes, 2000]. The first model of magnetic reconnection was developed within the framework of one-fluid resistive MHD, the so-called Sweet-Parker (SP) model [Sweet, 1958, Parker, 1957]. A key ingredient of the SP regime is magnetic resistivity, which breaks the frozen-in condition (see equation 1.2) in the dissipation region thus allowing for magnetic reconnection to occur. For the development of the SP model, we consider a rectangular magnetic reconnection region of width 2δ and length 2Δ as is shown in Figure 4.1.

The upstream plasma carrying frozen-in magnetic field lines of intensity B_{in} with a inflow velocity u_{in}, reconnect at the neutral point O (center of the gray area in Figure 4.1), and then the plasma is ejected downstream from O with an outflow speed u_{out} dragging the reconnected field lines of intensity B_{out} along with it. In Figure 4.1, the green arrow heads correspond to the out-of-plane current. From the incompressible assumption of the plasma (i.e. $\boldsymbol{\nabla} \cdot \mathbf{u} = 0$) we obtain

$$u_{in}\Delta = u_{out}\delta \tag{4.1}$$

which is a direct consequence of the mass conservation. In this 2D setup, the self-consistent electric field points out of the plane (i.e. $\hat{\mathbf{z}}$), and in stationary regime it will satisfy $E_z \sim$ const since

$$\boldsymbol{\nabla} \times \mathbf{E} = -\frac{\partial \mathbf{B}}{\partial t} = 0 \;\rightarrow\; E_z = \text{const.} \tag{4.2}$$

Therefore, we can evaluate the electric field (2.32) in three particular points,

$$E_z(0,\delta) = -u_{in} B_{in} \tag{4.3}$$

$$E_z(0,0) = \eta j_z(0,0) \sim -\eta \, \frac{B_{in}}{\delta} \tag{4.4}$$

$$E_z(\Delta,0) = -u_{out} B_{out} \tag{4.5}$$

where we have used the fact that $B_{out} << B_{in}$ and $\delta < \Delta$ in equation (4.4). Using equation (4.1), matching equations (4.3) with (4.4) and (4.3) with (4.5), we obtain

$$u_{in} = \frac{\eta}{\delta} \tag{4.6}$$

$$B_{in}\delta = B_{out}\Delta \tag{4.7}$$

respectively. The equation (4.7) is also consistent with $\boldsymbol{\nabla} \cdot \mathbf{B} = 0$.

Next, we consider the inviscid and stationary equation of motion (2.22) for this one-fluid plasma

$$(\mathbf{u} \cdot \boldsymbol{\nabla})\mathbf{u} = -\boldsymbol{\nabla}\left(p + \frac{B^2}{2}\right) + (\mathbf{B} \cdot \boldsymbol{\nabla})\mathbf{B} \tag{4.8}$$

along the x and y directions. In the equation of motion along the y (inflow) direction the inertial term ($u_{in} << B_{in}$) and the magnetic tension (large curvature radius of incoming field lines) can be neglected, and this equation reduces to the total pressure balance across the reconnection layer,

$$\frac{\partial}{\partial x}\left(p + \frac{B^2}{2}\right) = 0 \;\rightarrow\; p(0,0) = p(0,\delta) + \frac{B_{in}^2}{2} \tag{4.9}$$

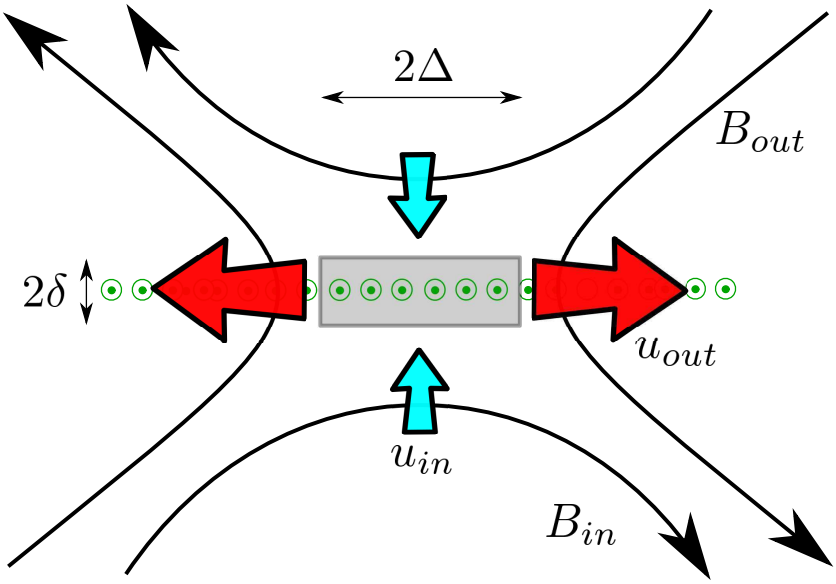

FIGURE 4.1: Schematic 2D Sweet-Parker magnetic reconnection region.

Along the x (outflow) direction, we find that the outgoing jet is powered by a combination of pressure gradient and magnetic tension. As a result

$$\frac{u_{out}^2}{2} \sim -\left(p(\Delta,0) - p(0,0)\right) + B_{in}^2. \tag{4.10}$$

Combining equations (4.9) and (4.10) we obtain

$$u_{out}^2 = B_{in}^2 - 2\left(p(\Delta,0) - p(0,0)\right) \tag{4.11}$$

where B_{in} is the Alfvén velocity in dimensionless form. In a simple terms, the pressure and magnetic tension forces accelerate the plasma along the reconnection layer up to velocities of the order of v_A. It is straightforward to show that the inflow reconnection velocity scales as

$$u_{in} = B_{in}\frac{\delta}{\Delta} = \sqrt{\frac{B_{in}\eta}{\Delta}} \tag{4.12}$$

where we have used equation (4.6) and the fact that the δ does not depend on Δ. Defining the dimensionless reconnection rate as $r \equiv |E_z(0,0)| = u_{in}/B_{in}$ we

obtain

$$r = \sqrt{\frac{\eta}{B_{in}\Delta}} = S^{-1/2} \tag{4.13}$$

where we have defined the Lundquist number as $S \equiv B_{in}\Delta/\eta$. In summary, the reconnection rate (4.13) scales as the square root of the magnetic resistivity, which leads to exceedingly low reconnection rates with respect to observations for most space physics environments [Edwards et al., 1986, Bhattacharjee, 2004, Øieroset et al., 2007, Yamada, 2011].

To check the scaling (4.13), we have performed 2D resistive MHD simulations using a pseudo-spectral code. Our initial condition for the simulation of a thin current sheet is given by (assuming periodic boundary conditions in a $2\pi \times 2\pi$ box)

$$\mathbf{B}(x, y, t = 0) = \mathrm{B}_0 \left[\tanh\left(\frac{y - \frac{3\pi}{2}}{2\pi l}\right) - \tanh\left(\frac{y - \frac{\pi}{2}}{2\pi l}\right) + 1 \right] \hat{\mathbf{x}} \tag{4.14}$$

where, in normalized units, we have $\mathrm{B}_0 = 1$ and $l = 0.02$. Figure 4.2 shows the B_x as a function of the y coordinate for the entire integration box. To drive the reconnection process, a spatial monochromatic perturbation $\delta\mathbf{B} = \boldsymbol{\nabla} \times [\hat{\mathbf{z}}\, \delta a(x, y)]$ with $\delta a(x, y) = a_0 \cos(k_x x)$, $k_x = 1$ and an amplitude of $a_0 = 0.02\mathrm{B}_0$ is added to the initial condition (4.14). In Figure 4.3 we show the onset of magnetic reconnection. Contour levels of magnetic flux $a(x, y)$ are in white lines, superimposed to the electric current density component along the z direction, $j(x, y)$, at time $t = 0.0$ (in grayscale). The brightest regions correspond to the current sheets. We only show half a box of integration for each case, of size $2\pi \times \pi$.

Using the initial conditions described above we have performed numerical simulations with high spatial resolution of 2048^2 grid points, for the two particular magnetic resistivities, $\eta_1 = 0.015$ and $\eta_2 = 0.03$ (noted that $\eta_2 = 2\eta_1$). To quantitatively measure the efficiency of the magnetic reconnection process, we study the

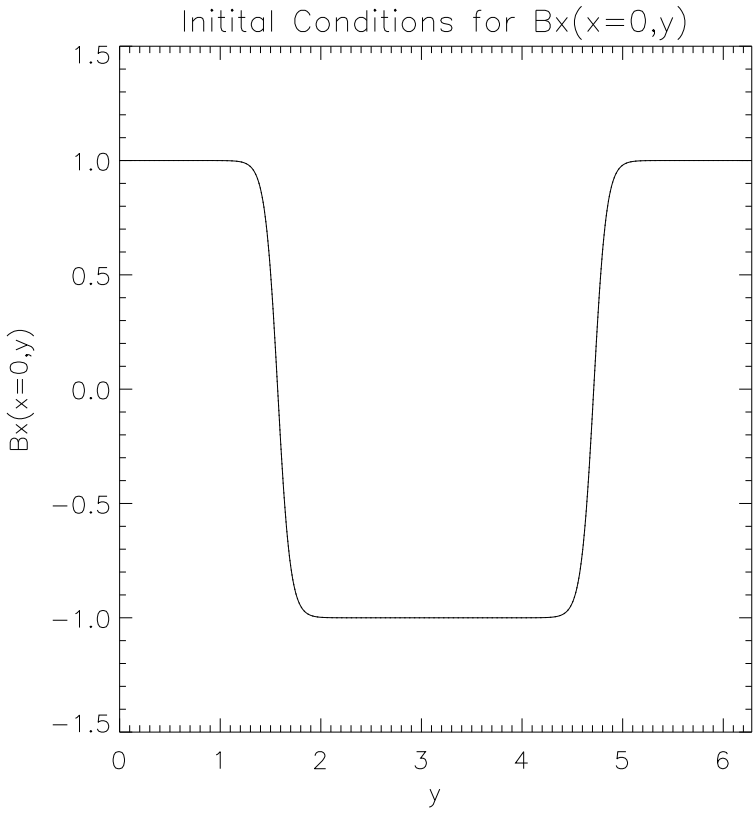

FIGURE 4.2: Initial profile for $B_x(x = 0, y)$ as a function of y.

dimensionless magnetic reconnection rate $r(t)$, which is the rate at which magnetic flux flows into the central neutral point (the X-point). Near the neutral point, magnetic flux enters at a relatively slow plasma inflow velocity u_{in} and is expelled at speeds of the order of the Alfvén velocity. Figure 4.8 shows the vertical surface used to integrate the magnetic flux $\Phi(t) = \int \mathbf{dS} \cdot \mathbf{B}$, that extends from the O-point of one of the current sheets (shown in black, corresponding to negative values of $j(x, y)$), to the X-point of the other (shown in white). Both the O-point and the X-point are stagnation points of the flow. Using equation (2.30) it is straightforward to show that

$$\phi(t) = \int \mathbf{dS} \cdot \mathbf{B} = a_{max} - a_{min} \tag{4.15}$$

The reconnection rate $r(t)$ is the variation of this magnetic flux per unit time, i.e. $r(t) = d\phi(t)/dt$.

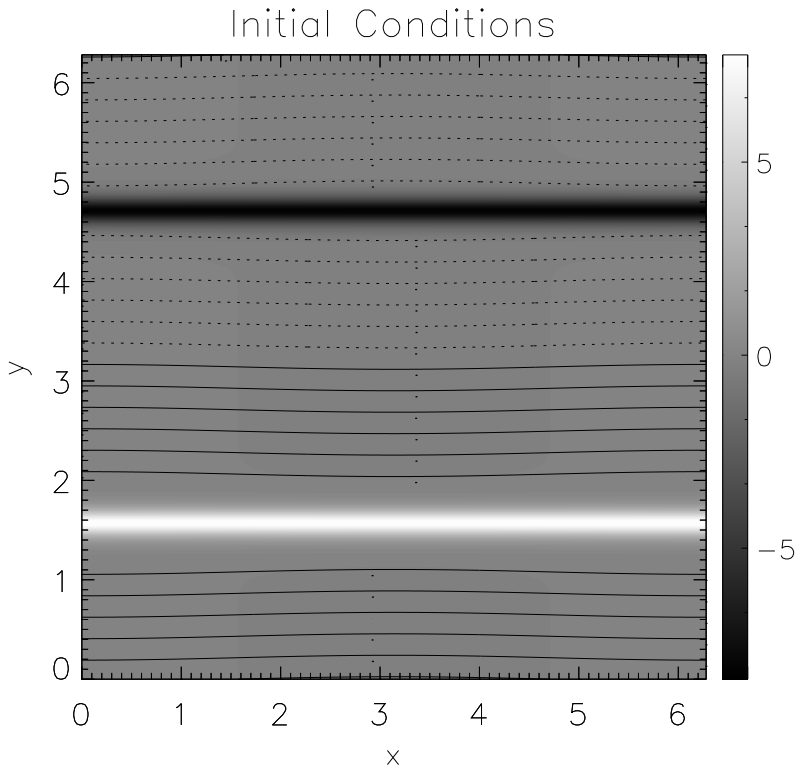

FIGURE 4.3: The images (in grayscale) show the spatial distribution of current density $j(x, y)$ at $t = 0.0$, for the integration box (see Figure 4.8). Contour levels of $a(x, y)$ are superimposed (solid and dashed black lines for $a > 0$ and $a < 0$, respectively).

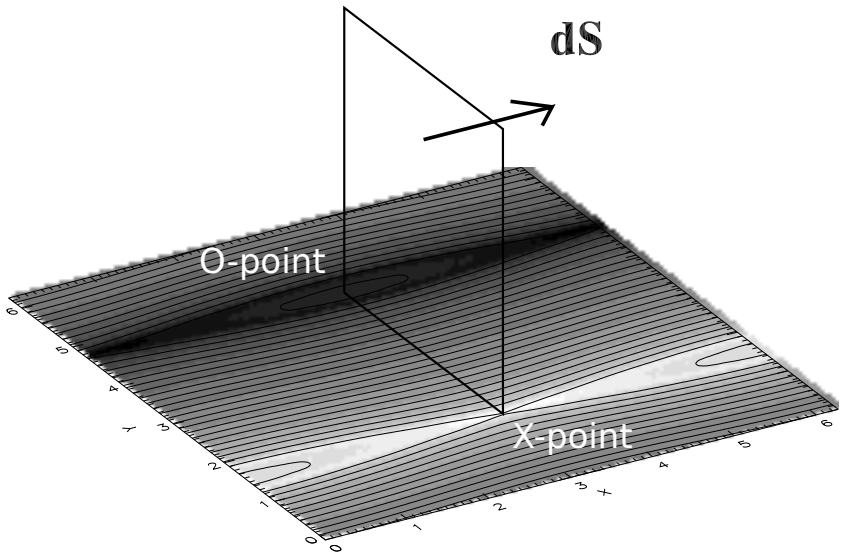

FIGURE 4.4: Schematic configuration for the calculation of the reconnection rate. The horizontal plane shows the distribution of $j(x, y)$ for the full box, contour levels of $a(x, y)$ are superimposed.

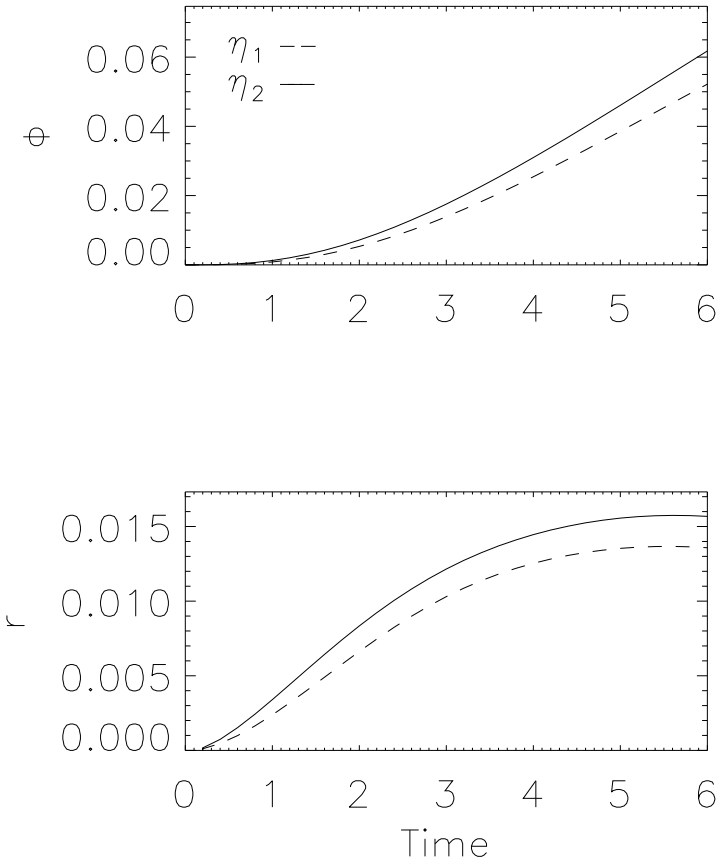

FIGURE 4.5: Reconnected flux and reconnection rate as a function of time for $\eta_1 = 0.015$ (dashed line) and $\eta_2 = 0.03$ (solid line). The two runs correspond to MHD simulations.

Figure 4.5 shows the reconnected flux and reconnection rate as a function of time. The reconnection rate $r(t)$ is calculated using second order finite central differences from the time series of the flux $\phi(t)$. The two curves correspond to MHD runs using η_1 (dashed line) and η_2 (solid line). In the case of $\eta_1 = 0.015$, we obtain a maximum reconnection rate of 0.0136 at $t \sim 5.4$, while for $\eta_2 = 2\eta_1$, we get a maximum reconnection rate of 0.0157 at $t \sim 5.4$. As expected, when we duplicate the magnetic resistivity, the maximum reconnection rate increases by a factor $\sim 2^{-1/2}$.

4.2 Collisionless magnetic reconnection: the effect of electron inertia

Kinetic plasma effects such as Hall and electron inertia, introduce new spatial and temporal scales into the theoretical one-fluid description. In a two-fluid description of a plasma with isotropic pressure tensors, only two kinetic effects are able to break magnetic field lines and give rise to reconnection: magnetic resistivity and electron inertia. For instance, if the resistive scale is larger than the ion inertial length, the resistive MHD model is a valid description for a collisional plasma. Most if not all of the fluid descriptions listed in the literature include electric resistivity. In fact, at least a small amount of numerical resistivity is originated in the computational scheme used to calculate the spatial derivatives. However, in a truly collisionless regime magnetic reconnection should be driven solely by electron inertia.

Our goal is to study magnetic reconnection exclusively due to electron inertia, by completely suppressing the action of magnetic resistivity. We use a pseudo-spectral scheme to compute the spatial derivatives, which converges exponentially fast as the number of grid points is increased. As a result, we can run simulations with zero resistivity and/or viscosity, and check that we are not spuriously adding numerical resistivity simply by monitoring the energy conservation for each run. As energy is conserved with a precision consistent with round-off errors, we are certain that reconnection in our simulations arises exclusively as a result of finite electron inertia, and not because of the presence of physical or numerical resistivity. For spatial scales below of the electron skin-depth the terms of electron inertia are dominant, and the electrons can no longer be frozen-in to the magnetic field lines [Vasyliunas, 1975]. As it was discussed in the Introduction, the electron inertia (with isotropic pressures) is the only mechanism responsible for the observed

changes in the magnetic field topology.

Next, we performed various sets of numerical simulations with spatial resolutions of 512^2, 1024^2, 1536^2 and 2048^2 grid points. The initial condition are the same used in the previous section. For all these cases we use a Hall parameter $\lambda_H = 0.1$ and a value of mass ratio $m_e/m_p = 0.015$. In addition, we made 3 runs with high spatial resolution (1024^2, 1536^2 and 2048^2 grid points) and a realistic ratio of electron to proton mass, i.e. $m_e/m_p = 1/1836$.

To test the accuracy of our results, we focused our attention on the spatial resolution of our simulations. For this purpose, we made different runs for several spatial resolutions, starting from the same initial condition. More specifically, we performed 2.5D runs with the following numbers of grid points: 512^2, 1024^2, 1536^2 and 2048^2. For each spatial resolution, we calculated the reconnected flux and we plotted it as a function of time (see Figure 4.6). As expected, for the ideal MHD and HMHD cases, the curve for the reconnected flux converges to zero as the spatial resolution is increased (line color scale is progressively darker). Therefore, as the number of grid points increases, the reconnection rate approaches zero, both in the ideal one-fluid MHD and HMHD cases. In the case of EIHMHD, since we expect the electrons to break the frozen-in condition, the reconnected flux converges to a value different from zero, as the number of grid points increases.

4.3 Reconnected flux and reconnection rate

Within the framework of EIHMHD, we have study the collisionless magnetic reconnection problem considering $\lambda = 0.1$ and a realistic value of the electron mass ($m_e/m_p = 1/1836$). Using the same initial conditions described in Section 4.1, we performed simulations with progressively higher spatial resolution (1024^2, 1536^2 and 2048^2). Figure 4.7 shows the reconnected flux and reconnection rate, for each

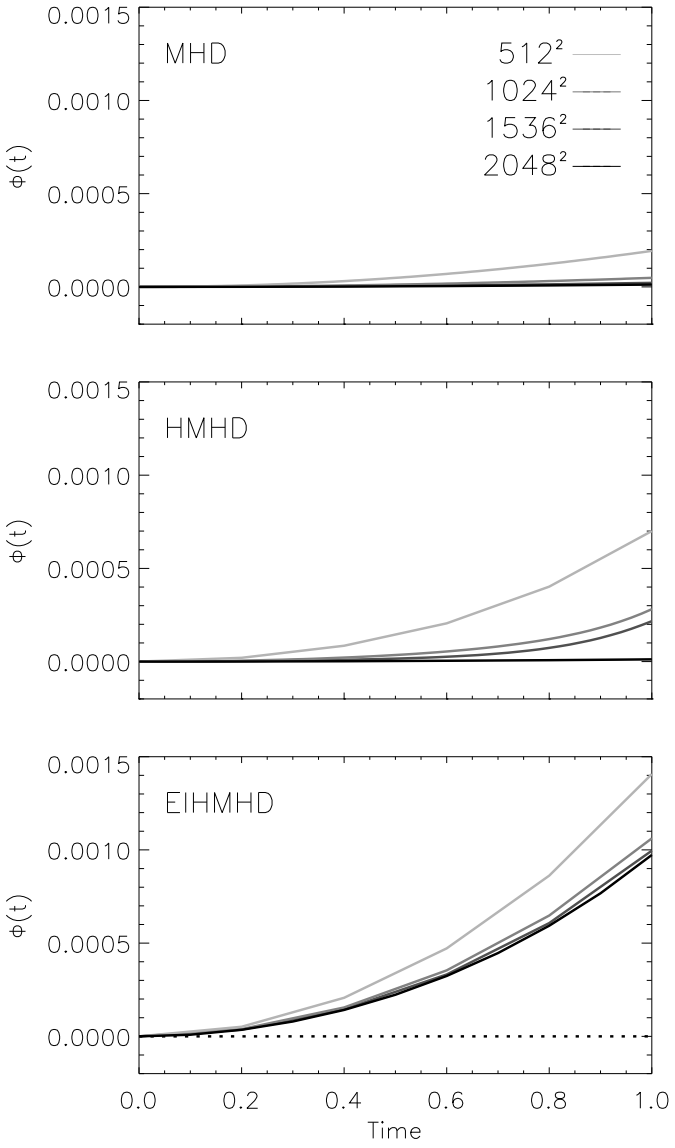

FIGURE 4.6: Reconnected flux versus time. Each panel corresponds to a different case, as labelled. Different spatial resolutions: 512^2, 1024^2, 1536^2, and 2048^2 correspond to progressively darker traces.

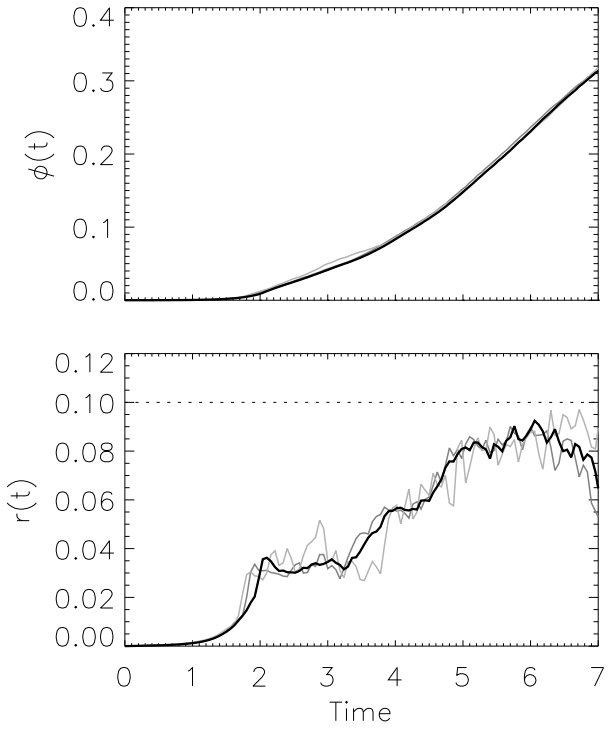

FIGURE 4.7: Reconnected flux and reconnection rate as a function of time for 1024^2 (light gray line), 1536^2 (dark gray line) and 2048^2 (black line) grid points. The three runs correspond to $\lambda = 0.1$ and a realistic mass ratio ($m_e/m_p = 1/1836$).

spatial resolution, as a function of time. As expected, we obtain essentially the same curve for the three spatial resolutions in agreement with the results shown in Figure 4.6. In particular, we get a maximum reconnection rate reaching values close to 0.1, which corresponds to inflow velocities approaching a fraction of the Alfvén speed. This result is consistent with those reported in the literature, in particular with PIC simulation results [Zenitani et al., 2011, Fujimoto, 2011] and the GEM Challenge [Birn et al., 2001]. In particular, using a partially implicit PIC code, Zenitani et al. [2011] found a reconnection rate approaching $0.1v_A$. It is worth mentioning that we obtained a reconnection rate comparable to the one reported by Birn et al. [2001], because we used a similar set of initial conditions and parameter values. Nevertheless, the reconnection rate is expected to depend on the Hall parameter [Smith et al., 2004, Morales et al., 2005, 2006]. In the

next section, we study how the reconnection rate changes as the Hall parameter is increased. Other authors considered cases were the reconnection event takes place in presence of a background turbulence. In those cases, they found that the reconnection rate also depends on the amplitude of fluctuations δB [Smith et al., 2004].

Finally, we compared the reconnected flux and reconnection rate for the same initial conditions and different electron to proton mass ratios. In particular, we compared the results for $m_e/m_p = 0.015$ and $m_e/m_p = 1/1836$. We obtain the same trend for both the reconnected flux and the reconnection rate. In agreement with PIC simulations [Zenitani et al., 2011] and resistive HMHD simulations [Birn et al., 2001], we find that the reconnection rate is insensitive to the electron to proton mass ratio.

4.4 Magnetic reconnection rate scaling

4.4.1 Theoretical scaling of magnetic reconnection rate

In the context of collisionless magnetic reconnection, the reconnection region develops a multi-scale structure in which the ion and electron inertial lengths $\lambda_{i,e}$ play a role [Biskamp et al., 1997]. As we discussed in the Introduction, ions can be considered approximately static and electrons are the ones to carry most of the electric current. Also, at these scales the terms of electron inertia become dominant, and the electrons can no longer be frozen-in to the magnetic field lines [Vasyliunas, 1975]. Therefore, at this level of description, a change in the topology of the magnetic field lines which is exclusively due to electron inertia, becomes possible.

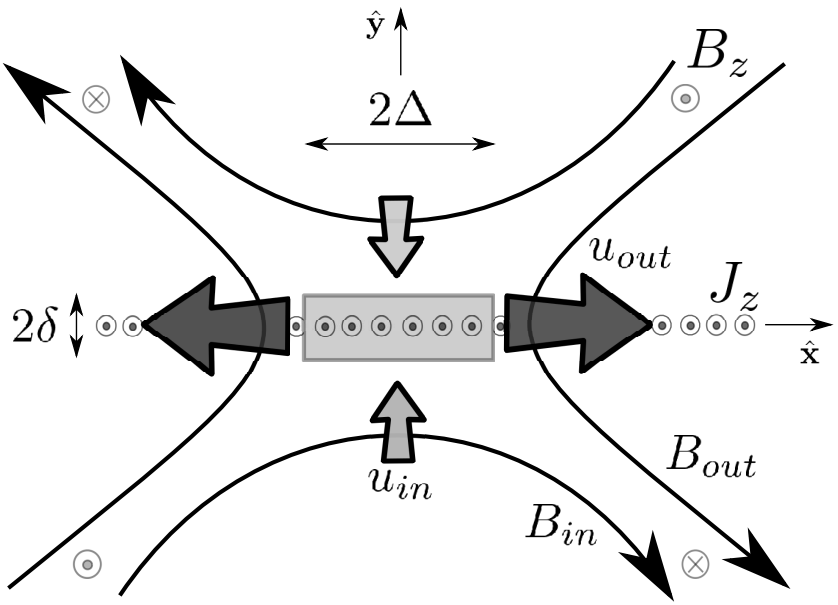

FIGURE 4.8: Schematic 2.5D reconnection region.

Within scales near the X-point, where $|\mathbf{u}_i| << |\mathbf{J}/en|$, we obtain a scaling for the reconnection rate as a function of λ and μ which are the main parameters of the problem. We consider a rectangular reconnection region with a width 2δ and a length 2Δ (see Figure 4.8). By definition, the reconnection rate in a 2D configuration is the out-of-plane component of the electric field (i.e., E_z) at the X-point. The electric field can be obtained from the ideal equation of motion for the electrons (2.16) as

$$\mathbf{E} = -\frac{m_e}{e}\left[\frac{\partial \mathbf{u}_e}{\partial t} + \mathbf{u}_e \times (\boldsymbol{\omega}_e + \frac{e}{m_e c}\mathbf{B}) + \boldsymbol{\nabla}\left(\frac{u_e^2}{2} + \frac{p_e}{m_e n}\right)\right]. \tag{4.16}$$

Under the assumption of quasi-stationarity (i.e., $\partial_t \sim 0$) for a 2.5D setup (i.e., $\partial_z \sim 0$), the out-of-plane component of the electric field (the $\hat{\mathbf{z}}$ direction) reduces to

$$E_z = -\frac{m_e}{e}\,\hat{\mathbf{z}} \cdot \mathbf{u}_e \times \boldsymbol{\omega}_e = \frac{m_e}{e^3 n^2}\,\hat{\mathbf{z}} \cdot \mathbf{J} \times (\boldsymbol{\nabla} \times \mathbf{J}) \tag{4.17}$$

where we have assumed $\mathbf{u}_e \sim -\mathbf{J}/en$.

In view of the sketch shown in Figure 4.8, close to the X-point is $\partial_x \sim \Delta^{-1}$, $\partial_y \sim \delta^{-1}$ and $J_z = cB_{in}/4\pi\delta$, where B_{in} is the magnetic field at the edge of the reconnection region in the inflow direction. Therefore,

$$E_z = \frac{m_e}{e}\left(\frac{c}{4\pi ne}\right)^2 \frac{B_z B_{in}}{\Delta\delta^2}. \tag{4.18}$$

To estimate the out-of-plane component of the magnetic field (B_z), we consider the $\hat{\mathbf{z}}$ component of the curl of equation (4.16) (under quasi-stationary conditions), i.e.

$$\hat{\mathbf{z}} \cdot \boldsymbol{\nabla} \times \left[\mathbf{J} \times \left(\frac{e}{cm_e}\mathbf{B} - \frac{1}{en}\boldsymbol{\nabla} \times \mathbf{J}\right)\right] = 0 \tag{4.19}$$

which, in 2.5D setup leads to

$$\mathbf{B}_\perp \cdot \boldsymbol{\nabla}_\perp J_z = \left(\frac{c}{\omega_{pe}}\right)^2 \mathbf{J}_\perp \cdot \boldsymbol{\nabla}_\perp (\nabla^2 B_z) \tag{4.20}$$

and therefore

$$B_z = \frac{\omega_{pe}\delta}{c} B_{in}. \tag{4.21}$$

The $\hat{\mathbf{z}}$-component of the electric field at the X-point is then

$$E_z = \frac{c}{4\pi en}\frac{B_{in}^2}{\Delta\delta\omega_{pe}}. \tag{4.22}$$

The dimensionless reconnection rate, i.e. $r \equiv cE_z/B_0 v_A$, becomes

$$r = \frac{c}{\omega_{pM}\Delta}\frac{c}{\omega_{pe}\delta}\left(\frac{B_{in}}{B_0}\right)^2 \tag{4.23}$$

As it was discussed in the Introduction, we expect B_{in} and Δ not to depend on λ [Simakov and Chacón, 2008]. Their particular values are only determined by the boundary and initial conditions. Nevertheless, in the next section we evaluate the potential dependence of B_{in}, δ and Δ with the Hall parameter in our numerical

results.

Assuming that the thickness of the current sheet is essentially the electron inertial length, i.e. $\delta \sim c/\omega_{pe}$ and also that the typical magnetic field intensity is $B_0 = B_{in}$ and the typical length scale is $L_0 = \Delta$ we obtain

$$r = \lambda \tag{4.24}$$

Note that if $\delta \sim c/\omega_{pe}$, according to (4.21) we also obtain that (in the regime of quasi-stationary reconnection) $B_z \sim B_{in}$. Note also that the reconnection rate is independent of the mass ratio μ, as shown in Andrés et al. [2014a].

4.4.2 Quasi-stationary magnetic reconnection

Within the framework of EIHMHD, we study the collisionless magnetic reconnection problem varying the dimensionless Hall parameter λ. Using the initial conditions described in subsection 4.1, we performed ten ideal runs with a spatial resolution of 2048^2 grid points for different values of the Hall parameter. Our runs span the range $\lambda = 0.07$ to $\lambda = 0.16$, with a step of 0.01. The values of λ are sufficiently small, to minimize the potential influence of boundary conditions. In all these runs the electron to ion mass ratio corresponds to $m_e/m_i = 0.015$.

To measure the efficiency of the magnetic reconnection process, the dimensionless reconnection rate $r(t)$ is defined, which is the rate at which magnetic flux flows into the X-point. Using equation (3.7) it is straightforward to show that the total reconnected flux $\Phi(t)$ is $\Phi(t) = a_{max} - a_{min}$ [Smith et al., 2004, Andrés et al., 2014a]. Therefore, the reconnection rate $r(t)$ is the variation of the magnetic flux per unit time, i.e. $r(t) = d\Phi(t)/dt$. Figure 4.9 shows the reconnected flux (upper panel) and reconnection rate (lower panel) as a function of time, for the

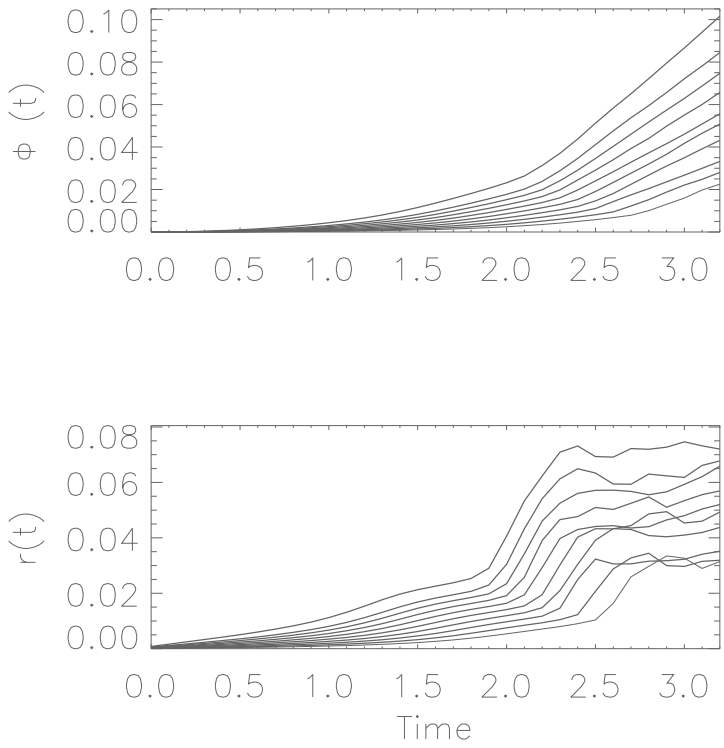

FIGURE 4.9: Reconnected flux Φ (upper panel) and reconnection rate r (lower panel) as a function of time for $\lambda = 0.07, \cdots, 0.16$ (from bottom to top). For all runs the electron to ion mass ratio is $m_e/m_i = 0.015$.

ten values of the Hall parameter. In contrast to previous claims [Shay et al., 1991, Birn et al., 2001], Figure 4.9 shows that the reconnection rate strongly depends on λ and is not a universal constant. As it can be seen, the reconnected flux monotonically increases with λ, which ultimately leads to an increment of the maximum magnitude of reconnection rate. We also note that as we increase λ, the maximum reconnection rate occurs at earlier times. Similar behavior has been reported in the literature when the Hall effect is included in Ohm's law [Smith et al., 2004, Morales et al., 2005, 2006].

From equation (4.23) we see the importance of studying whether the thickness and width of the reconnection region (δ and Δ, respectively) and the magnetic field at the edge of this region (B_{in}) change as a function of the Hall parameter. Since our scaling was performed assuming quasi-stationary conditions, we have to take this

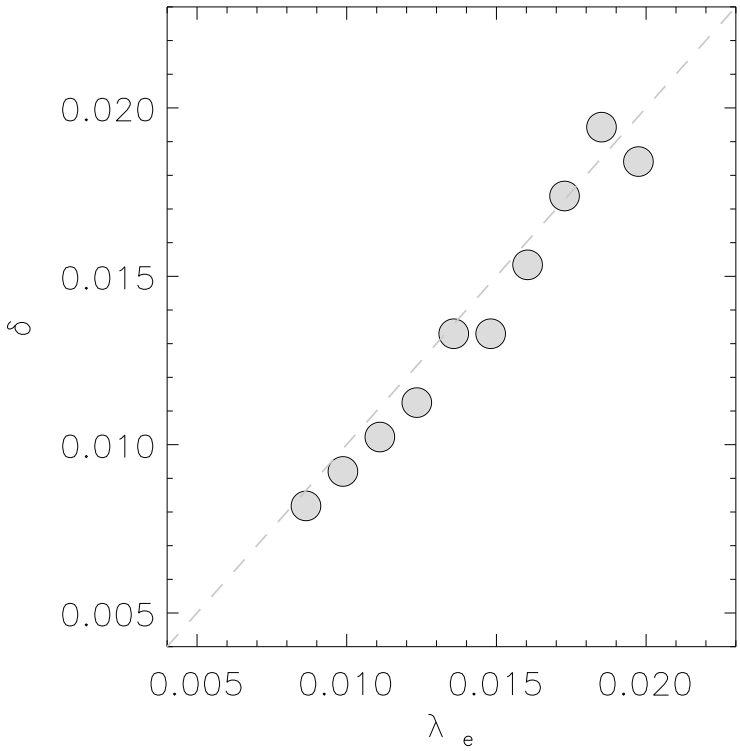

FIGURE 4.10: Quasi-stationary values of δ (gray circles) as a function of λ_e. We plot the electron inertial length λ_e in gray-dashed line for reference.

constraint into account. The width of the reconnection region δ is defined in terms of the current density profile $j(y)$ across the layer [Malyshkin, 2010]. The value of δ is obtained from a best fit of the numerical profile to a $\mathrm{sech}^2(y/\delta)$ function, which is consistent with the initial profile give by equation (4.14). To determine B_{in} we simply adopt $B_{in} = B_x(x = \pi/2, y = \pi/4 - \delta)$, since our neutral point is located at $x = \pi/2, y = \pi/4$. We assume that the system evolves in a quasi-stationary fashion during a time interval such that δ and B_{in} show approximately no temporal variations. The length of the reconnection region Δ was obtained from the outflow velocity profile $u_x(x, y = \pi/4)$ applying the incompressible condition for the plasma, i.e.

$$u_x^{(out)}(x = \frac{\pi}{2} + \Delta, y = \frac{\pi}{4}) = \frac{\Delta}{\delta}\, u_y^{(in)}(x = \frac{\pi}{2}, y = \frac{\pi}{4} - \delta). \tag{4.25}$$

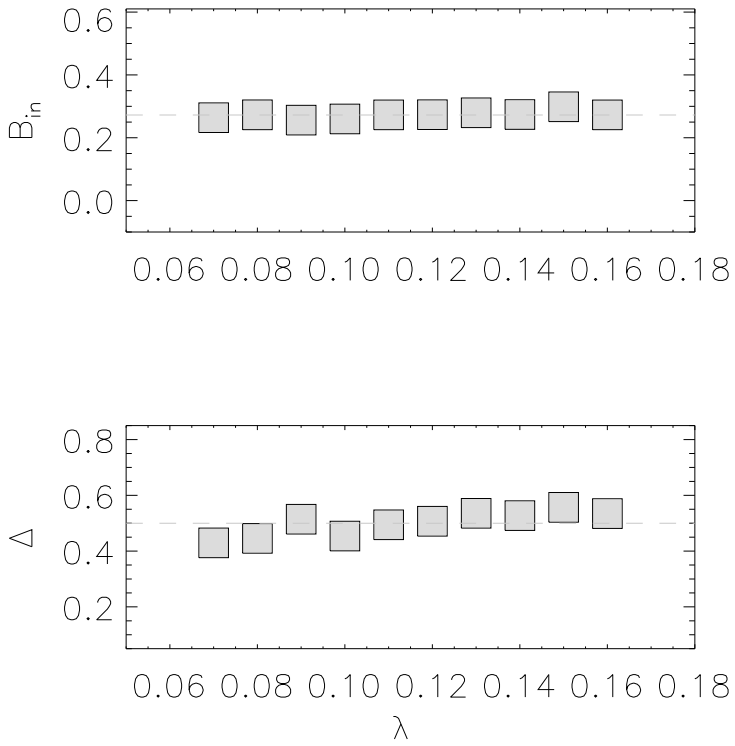

FIGURE 4.11: Quasi-stationary values of B_{in} (upper panel) and Δ (lower panel) as a function of λ. The gray-dashed line indicates the mean values of B_{in} and Δ.

Figure 4.10 shows the quasi-stationary values of δ (gray circles) as a function of λ_e. In addition, we plot λ_e in gray-dashed line. As expected, the width of the reconnection region is of the order of the electron inertial length. In particular, from a best linear-fit for $\log \delta - \log \lambda_e$ we obtain $\delta = (1.3 \pm 0.3)\ \lambda_e^{1.06 \pm 0.07}$. Therefore, we conclude that $\delta \sim \lambda_e$.

Figure 4.11 shows B_{in} (upper panel) and Δ (lower panel) as a function of λ (gray squares) for the ten values of the Hall parameter. Figure 4.11 indicates that B_{in} and Δ show approximately no dependence with the Hall parameter. This result is compatible with previous results reported in the literature [Simakov and Chacón, 2008, Wang et al., 2001].

The results displayed in Figure 4.10 ($\delta \sim \lambda_e$) and Figure 4.11 ($B_{in} \sim$ const and

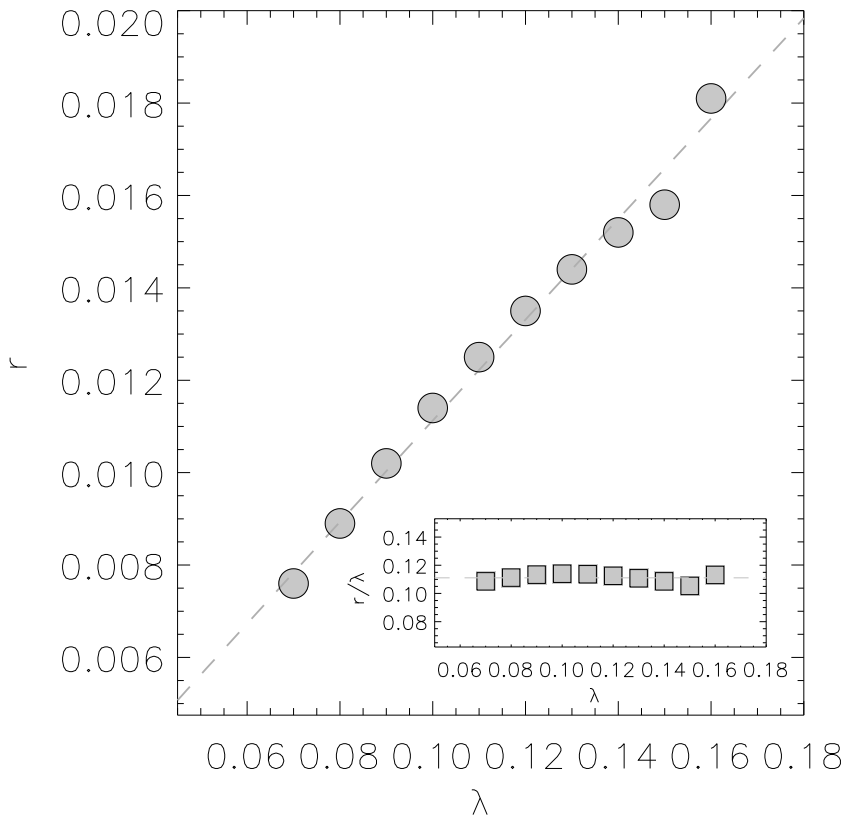

FIGURE 4.12: Quasi-stationary reconnection rate r (gray circles) as a function of the Hall parameter λ. The best linear-fit for $\log\lambda - \log r$ is shown in gray-dashed line. Inset: Ratio between quasi-stationary reconnection rates and the Hall parameter (gray squares) as a function of the Hall parameter.

$\Delta \sim$ const) lend support to the assumptions made in equation (4.23) to obtain equation (4.24), i.e. that the reconnection rate is simply proportional to the Hall parameter. Figure 4.12 shows the quasi-stationary reconnection rates (gray circles), i.e. the mean reconnection rate for the time interval determined in Section 4.4.2, as a function of the Hall parameter λ. In addition, we plot the curves corresponding to the best linear-fit for $\log\lambda - \log r$ (dashed line). The inset in Figure 4.12 shows r/λ (gray squares) as a function of λ. From the best linear-fit for $\log\lambda - \log r$ we obtain $r = (0.11 \pm 0.07)\ \lambda^{0.98\pm0.03}$. Therefore, we conclude that the reconnection rate r is compatible with a linear relation with the Hall parameter λ, as it was predicted by our analytical relation (4.24).

Finally, we also compare the quasi-stationary reconnection rate for a fixed value of the Hall parameter ($\lambda = 0.1$), and two different electron to proton mass ratios.

In particular, we compared the results for $m_e/m_i = 0.015$ and $m_e/m_i = 0.15$. In the quasi-stationary regime, we find approximately the same reconnection rate. This result is compatible with our theoretical result, which predicts that fast reconnection rate is insensitive to the electron to proton mass ratio even though it needs to be nonzero for reconnection to take place (Birn *et al.*, 2001; Zenitani *et al.*, 2011; see also Andrés *et al.*, 2014a).

4.5 Discussion

Our results show that we are able to obtain magnetic reconnection, only when the effects of electron inertia are retained, since our scheme is free from physical or numerical resistivity. As expected, for the ideal one-fluid MHD and HMHD cases, the reconnected flux converges to zero as the spatial resolution is increased, while in the case of EIHMHD the reconnected flux converges to a value different from zero, as the number of grid points increases. Therefore, we claim that considering electron inertia in a full two-fluid MHD description is a necessary physical ingredient to start the reconnection process. Note that in our pseudo-spectral scheme, numerical dissipation is essentially zero (within round-off errors). In particular, the simulations reported here correspond to zero viscosity and resistivity, and the total energy is conserved by the numerical scheme with an error $\Delta E/E < 10^{-8}$. The ion and electron helicities were initially zero, and throughout their evolution differ from zero in less than 10^{-15}. It is clear that numerical dissipation remains close to the round-off errors.

For high spatial resolution simulations we find a reconnection rate that is quantitatively compatible with the one found by Birn et al. [2001], when we use parameter values and initial conditions similar to theirs. We note however, that the reconnection rate might still depend on the value of the Hall parameter λ or on the level

of fluctuations δB. In particular, within the framework of two-fluid MHD and assuming stationary conditions, we obtain a theoretical scaling for the reconnection rate. Our numerical results confirm our assumptions that the thickness of the current sheet is essentially the electron inertial length, i.e. $\delta \sim \lambda_e$, and that B_{in} and Δ do not depend on the Hall parameter [Simakov and Chacón, 2008]. More importantly, our numerical results also confirm the predicted linear dependence of the reconnection rate r with the Hall parameter λ (i.e. $r \propto \lambda$).

Within the context of incompressible HMHD, Simakov and Chacón [2008] presented a quantitative analysis of reconnection valid for the resistive, HMHD and EMHD regimes. Their study concentrated on the reconnection region, without considering any particular external driving force. In the resistive MHD limit, the authors recover the standard resistive result [Parker, 1957]. In the limit of EMHD, the authors find that the reconnection rate does not explicitly depend on the dissipation coefficients and features a strong dependence on the Hall parameter. In particular, they confirm an earlier result and find that $r = \sqrt{2}\lambda/\Delta$ [Chacón et al., 2007], which is consistent with our scaling. Malyshkin [2008] also calculated the rate of quasi-stationary, 2.5D magnetic reconnection within the framework of incompressible HMHD. The author find that the dimensionless reconnection rate is independent of the electrical resistivity and equal to λ/L, where L is the scale length of the external magnetic field in the upstream region outside the electron layer. This result is also compatible with our theoretical results [see also Malyshkin, 2009]. In a different direction, Wang et al. [2000] reported a similar linear dependence with λ and noted that B_{in} is determined by the functional form of the boundary conditions, while Δ depends on a external time-dependent driving force. For a particular model of external driving, Wang et al. [2001] calculated the scaling of the reconnection rate within the framework of resistive HMHD. The authors found a $\lambda^{1/2}$ dependence for the reconnection rate. This particular scaling

is not comparable with our results, since in our simulations we do not consider any external driving force.

4.6 Resumen en castellano

En este Capítulo presentamos los resultados y discusiones referidos al proceso de reconexión magnética.

En la sección 4.1, presentamos el cálculo detallado del modelo resistivo de Sweet-Parker para estudiar reconexión magnética. Presentamos condiciones iniciales para estudiar numéricamente el problema de reconexión magnética. Además, presentamos resultados numéricos confirmando las predicciones del modelo de Sweet-Parker.

En la sección 4.2, estudiamos la reconexión magnética no-colisional (es decir, cuando las resistividad es cero). Presentamos los resultados numéricos que indican que la reconexión magnética en el modelo de dos fluidos MHD es debida a la inercia electrónica.

En la sección 4.3, estudiamos la tasa de reconexión y el flujo magnético reconectado. Nuestros resultados indican que, aunque la inercia electrónica es un condimento necesario para que el proceso de reconexión no-colisional tenga lugar, la eficiencia con la cual las líneas de campo magnético son reconectadas no depende de la masa del electron.

En la sección 4.4, dentro del contexto de dos fluidos MHD, bajo condiciones estacionarias, calculamos teoricamente la tasa de reconexión. Además, confirmamos numéricamente nuestra predicción teórica.

Finalmente, en la sección 4.5, presentamos las discusiones y conclusiones del Capítulo.

Chapter 5

ULF wave foreshock boundary

... but some day the piecing together of dissociated knowledge will open up such terrifying vistas of reality, and of our frightful position therein, that we shall either go mad from the revelation or flee from the deadly light into the peace and safety of a new dark age.

The Call of Cthulhu. H. P. Lovecraft.

The interaction between ions backstreaming ions from the bow shock and the incoming solar wind gives rise to plasma instabilities from which ULF waves can grow. This region upstream from the shock populated with ULF waves is limited by the ULF wave foreshock boundary (UWFB). In the present Chapter, we present several ULF wave examples in Saturn's foreshock. Using Cluster and Cassini data, we study the statistical properties of Saturn's and the Earth's UWFB. We also examine the possible connexion between the observed foreshock boundary properties, the theoretical model for the UWFB and the ion acceleration mechanisms discussed in Section 2.5.

5.1 Overview of observations

As we discussed in the Introduction, the solar wind offers a unique opportunity to study collisionless plasma processes directly, which can not be achieved at Earth's laboratories. In this section, we briefly review the observations from Cluster and Cassini used to study both UWFB. In addition, we present a few particular examples of ULF wave activity in Saturn's foreshock.

The Cluster mission consists of four spacecrafts and it was designed to determined the three-dimensional and time-dependent characteristics of small-scale processes in the near Earth space plasma [Balogh et al., 1997]. The Cluster observations used in the present thesis consist of magnetic field and solar wind velocity vectors as well as plasma densities obtained upstream from the Earth's bow shock. These data were gathered during the first three years of Cluster's orbital data, i.e. from February 2001 through December 2003. We have used a cadence of 5 s^{-1} of magnetic field data from the flux gate magnetometer (FGM) on-board Cluster to investigate the presence of ULF waves upstream from the Earth's bow shock. The particle data used are from the Cluster Ion Spectrometer (CIS) experiment. For a more extensive description of FGM and CIS Cluster experiments see Balogh et al. [1997] and Rème et al. [2001], respectively. Finally, we extracted these observations from the Cluster Active Archive [1] and the CLWeb data base[2].

The main objectives of the Cassini-Huygens mission is an understanding of Saturn system. The observations used for the present study consist of the three components of magnetic field, measured by the Cassini dual magnetometer, obtained upstream from the Kronian bow shock during the first fifteen months of Cassini's orbital data, i.e. from June 2004 through August 2005. The Cassini dual magnetometer investigation consists of a vector helium magnetometer (VHM) and a

[1] *http* : *//caa.estec.esa.int*
[2] *http* : *//clweb.cesr.fr/*

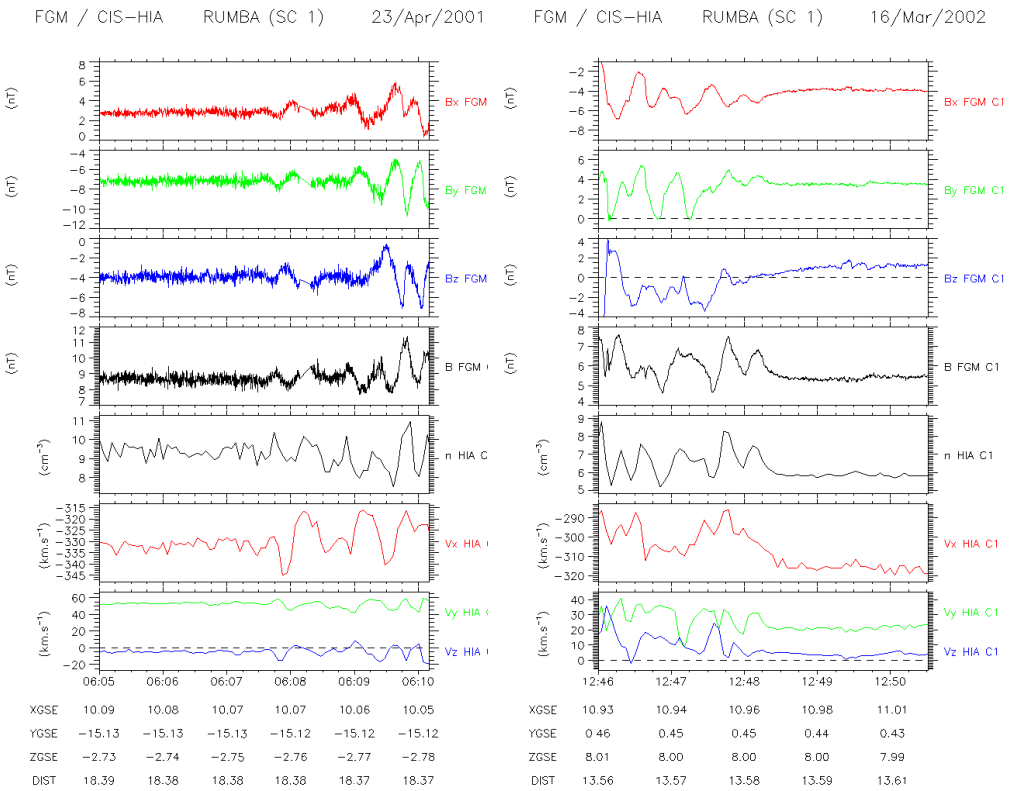

FIGURE 5.1: Left: Cluster is entering into the ULF wave region on 23 April, 2001. Right: a ULF wave region crossing (ending) made by Cluster on 16 March, 2002.

FGM which provide redundant, fast vector measurements of the ambient magnetic field over a wide range. The VHM provides accurate vector measurements with a resolution of 2 s^{-1} over a range of ± 256 nT, whereas FGM samples the magnetic field over a larger range (± 65655 nT) and at higher frequency (32 s^{-1}). This dual technique is extensively described in Dougherty et al. [2004]. For the purpose of our study, we only consider the data provided by the VHM. Unfortunately, Cassini plasma spectrometer (CAPS) could not be used in this study due to the absence of periods with adequate pointing to the incoming solar wind flow. Therefore, for the case of Saturn we only have magnetic field measurements. These measurements can be obtained from the Cassini web page[3].

During Cluster and Cassini excursions into the solar wind, we looked for intervals displaying patterns of ULF waves in the magnetic field components. For the

[3] *http : //saturn.jpl.nasa.gov/*

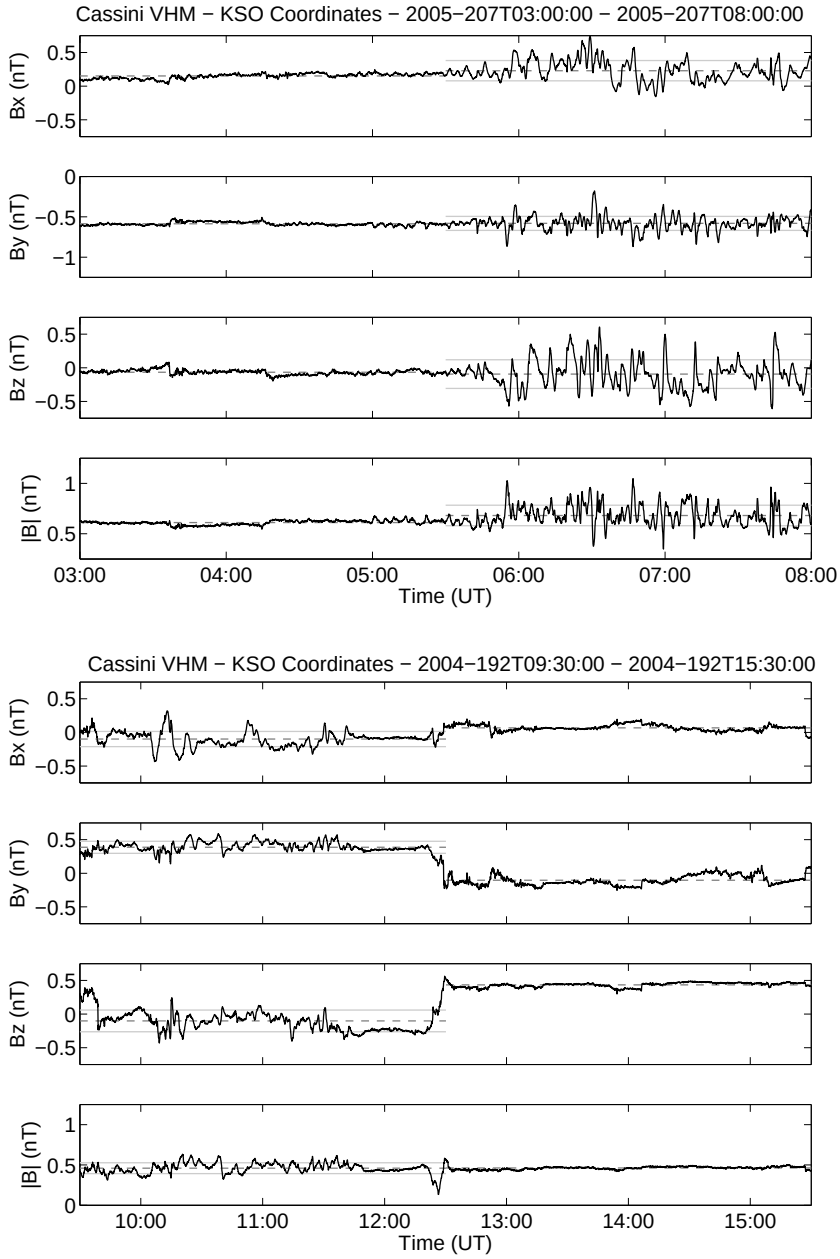

FIGURE 5.2: Examples of two crossing of the UWFB as detected by the VHM magnetometer on board Cassini between 03:00:00 UT and 08:00:00 UT on 26 July (day 207) 2005 (upper panel) and 09:30:00 UT and 15:30:00 UT on 10 July (day 192) 2004 (lower panel). Average values in the wave zone and in the zone without waves are in dashed-gray line. The solid-gray lines correspond to the average values plus/minus one standard deviation.

determination of these crossings, we made no distinction regarding the type of magnetic field fluctuations, requiring only that the transition from (or to) the wave region would be clearly apparent. Figures 5.1 and 5.2 show two ULF wave region crossing at Earth and Saturn, respectively. On one hand, Cassini's measurements are in Kronian Solar Orbital (KSO) coordinates, which are centered on Saturn and where the $\hat{\mathbf{x}}_{\text{kso}}$ axis points to the Sun, the $\hat{\mathbf{y}}_{\text{kso}}$ axis is anti-parallel to Saturn's orbital velocity and the $\hat{\mathbf{z}}_{\text{kso}}$ axis points towards the north pole of the Ecliptic. On the other hand, the Cluster data is in Geocentric Solar Ecliptic (GSE) system, which has the same definitions than the KSO system but is centered in the Earth.

A complete characterization of ULF waves on Earth (or Saturn) foreshock is beyond the scope of the present thesis. However, we present a brief characterization of the Kronian waves studied. In the case of the Earth, a complete classification and characterization of different ULF waves in the foreshock can be found in Eastwood et al. [2005] and references therein. Figure 5.3 and figure 5.4 show two examples of the types of wave events found on Saturn's ULF wave foreshock. For all the wave events, we made a characterization (polarization and frequency) in the spacecraft frame. As a result of this study, we find two distinct types of oscillations with different properties, depending on whether their frequencies are below or above the local proton cyclotron frequency ($\Omega_{ci} = eB_0/m_i c$). We also studied their polarization and propagation with respect to the ambient magnetic field using the Minimum Variance Analysis (MVA) [Sonnerup and Scheible, 1998]. The MVA consists in building the variance matrix in terms of the measured magnetic field components for a given time interval and finding the three eigenvalues and corresponding eigenvectors. The eigenvector corresponding to the smallest eigenvalue λ_3 (the maximum and intermediate eigenvalues are respectively λ_1 and λ_2) is used as an estimate of the direction of propagation of a plane wave. Note that the eigenvector set of the variance matrix provides a convenient natural coordinate

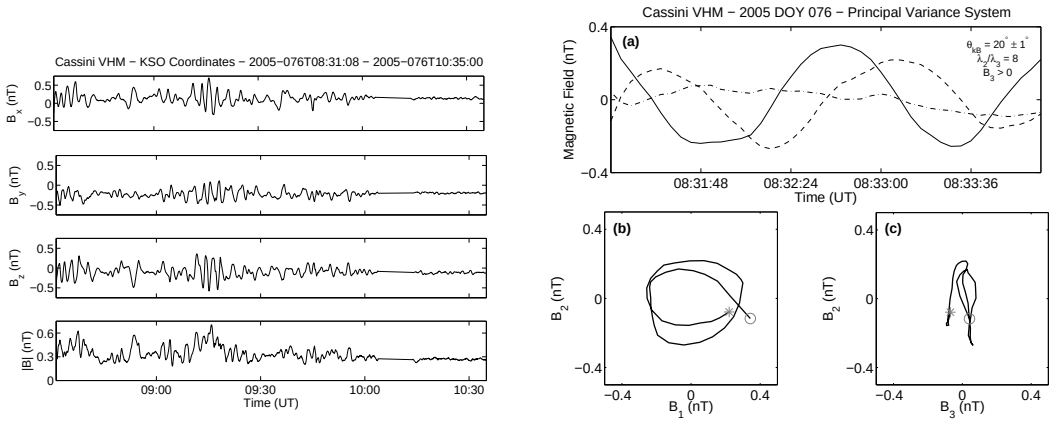

FIGURE 5.3: Left: Example of a wave train detected by the VHM on board Cassini on 17 March (day 076) 2005 between 08:35:00 UT and 10:35:00 UT. Right: (a) Magnetic field components along the maximum (solid line), intermediate (dashed line) and minimum variance direction (dot-dashed line). (b) Hodogram showing the magnetic field in the intermediate-minimum variance plane and (c) in the maximum-intermediate variance plane. The circle and the asterisk indicate the beginning and the end of the hodogram, respectively.

system in which to display and analyse the data.

Figure 5.3 (left panel) shows an example of waves detected by Cassini between 08:31:08 UT and 10:35:00 UT on 17 March (day 076) 2005. We obtained that these waves are approximately quasi-monochromatic and steepened with frequencies above $\Omega_{\rm ci}$. In the spacecraft frame, these waves have periods of the order of 60 s. According to the ambient magnetic field magnitude (∼0.3 nT), the period is significantly lower than the local proton cyclotron period $T_{ci} \sim 300$ s. On the right panel, Figure 5.3 shows the MVA results for a quasi-monochromatic wave packet shown in interval 08:31:12-08:34:04 UT. Panel (a) shows the components of the magnetic field along the maximum, intermediate and minimum variance direction. Panels (b) and (c) show the projection of the wave magnetic field (hodograms) on the maximum-intermediate and the minimum-intermediate variance planes, respectively. The circle and the asterisk indicate the beginning and the end of the hodogram, respectively. A large ratio between the intermediate and minimum eigenvalues of the variance matrix ($\lambda_2/\lambda_3 \approx 10$) shows a clear minimum variance

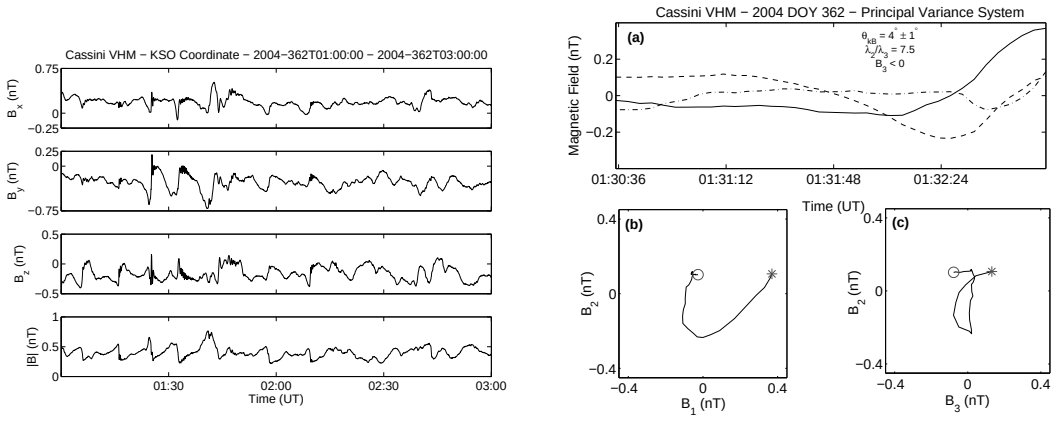

FIGURE 5.4: Left: Example of a wave train detected by the VHM on board Cassini on 27 December (day 362) 2004 between 01:00:00 UT and 03:00:00 UT. This wave event corresponds to a non linear packet. Right: MVA results in the same format as Figure 5.3

direction. The hodogram in panel (c) shows that the polarization on the minimum variance plane is circular right-handed with respect to the mean magnetic field ($B_3 > 0$). The angle between the mean magnetic field and the minimum variance eigenvector is $\theta_{kB} = 20° \pm 1°$, revealing that these waves propagate in a slightly oblique direction with respect to the ambient magnetic field.

Figure 5.4 (left panel) shows another example of a wave train seen by Cassini VHM between 01:00:00 UT and 03:00:00 UT on 27 December (day 362) 2004. We obtained that this kind of waves are phase steepened with frequencies smaller than Ω_{ci}. These waves have periods of the order of 5 to 10 min in the spacecraft frame, and they were the most frequently observed. According to the ambient magnetic field, 2 to 3 times the local proton cyclotron period for an IMF magnitude between 0.35 nT and 0.5 nT. In several cases, we observed a steepening front located at the right of waves with a higher frequency wave packet attached to it. We note a decrease in amplitude and in the period of these oscillations with increasing distance from the steepening front. The right panel from Figure 5.4 shows the results of the MVA applied on one period of these waves between 01:30:36 UT and 01:33:00 UT. From left to right, it can be seen how an early linear polarization

is followed by a circular polarization toward the end of the interval. The angle between the minimum variance vector and the mean magnetic field suggests that the propagation of these waves is quasi-parallel ($\theta_{kB} = 4° \pm 1°$) to the ambient magnetic field. The hodogram in Figure 5.4 shows that the magnetic field rotation around the minimum variance direction is left-handed with respect to the ambient magnetic field ($B_3 < 0$). It is worth noticing that we identified the same two categories previously identified by Bertucci et al. [2007], from a much bigger Cassini MAG's data set.

5.2 Solar Foreshock Coordinates

To identify the UWFB independently from the changes in the IMF or the location of the bow shock, we employed the so-called solar foreshock coordinates (SFC) introduced by Greenstadt and Baum [1986]. First, we construct the foreshock geometry based on the bow shock shape. This bow shock shape is axially symmetric about the planet-Sun direction, and has the following functional form,

$$r = \frac{L}{1 + e\cos\theta} \tag{5.1}$$

where r is the distance from the planet to a point on the shock surface, θ is the corresponding polar coordinate angle with respect to the symmetry axis, L is the semilatus rectum (size parameter) and e is the eccentricity.

As it was discussed in the Introduction, in the case of the Earth we have a physical model based on the solar wind ram pressure [Farris et al., 1991]. According to this model, the size parameter varies as the inverse one-sixth power of the dynamic

pressure [Binsack and Vasyliunas, 1968],

$$L = \left(\frac{p}{p_0}\right)^{-\frac{1}{6}} L_0 \tag{5.2}$$

where p is the ram pressure and p_0 is a reference ram pressure. The Farris model uses a fixed eccentricity $e = 0.81 \pm 0.02$ (ellipsoidal model), a nominal parameter size $L_0 = (24.8 \pm 0.2)\ R_E$ with a reference ram pressure $p_0 = 1.8$ nPa and a nominal zero focus position. For the Earth case, there are numerous bow shock models available in the literature and their reliability is parameter-dependent [Merka et al., 2005]. Our choice [Farris et al., 1991] is dictated by its simplicity since it only depends on the solar wind ram-pressure. It is clear from equation (5.2) that in-situ solar wind density and velocity measurements are necessary to accurately determine the location and shape of the bow shock.

On the other hand, in the case of Saturn we do not have any reliable bow shock model. However, Masters et al. [2008] presented an empirical fit (not a model!) using measurements from Cassini spacecraft. In particular, they found an eccentricity of $e = 1.05 \pm 0.09$ (hyperboloid model) and a nominal parameter size $L_0 = (51 \pm 2)\ R_S$. Therefore, for each crossing (in or out of the Saturn's ULF wave region) we used the eccentricity $e = 1.05 \pm 0.09$ and kept it constant throughout our study. However, we estimate the value of L using equation (5.1) and the location of the nearest bow shock crossing. For this purpose, we used the list of times and locations of Cassini's bow shock crossings between 27 June (day 027) 2004 and 12 August (day 224) 2005 published by Masters et al. [2008].

Once we have the determine the shape of the bow shock (i.e., L and e), we can define the SFC coordinate system. In this particular coordinate system, the $\hat{\mathbf{x}}$ axis points toward the Sun (it is parallel to $\hat{\mathbf{x}}_{\text{gse}}$), and the $\hat{\mathbf{x}}$-$\hat{\mathbf{y}}$ plane is the $\mathbf{v}_{\text{sw}}$-$\mathbf{B}$ plane which contains the location of the spacecraft at a given crossing of the UWFB.

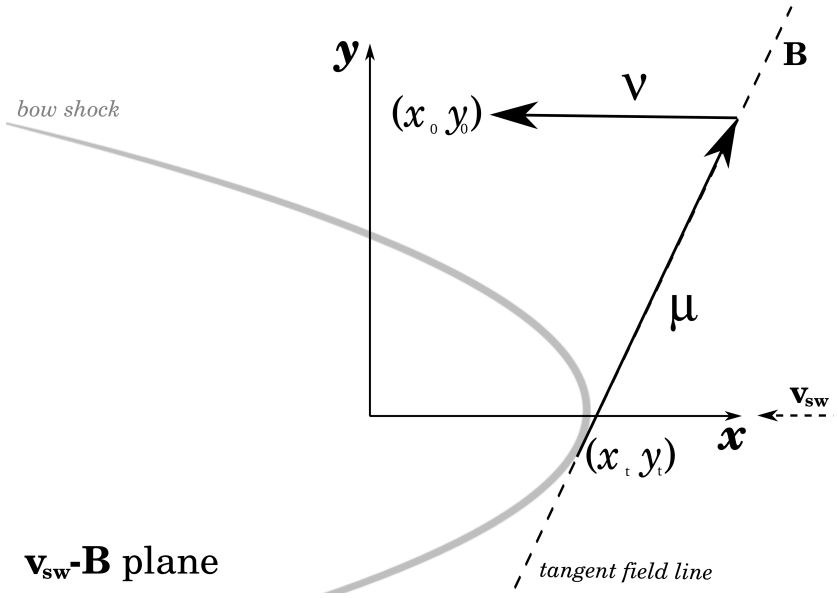

FIGURE 5.5: Schematic representation of the Solar Foreshock Coordinates (SFC).

The position of each boundary crossing is fixed by calculating the SFC coordinates μ and ν (see Figure 5.5).

$$\mu = \frac{(y_o - y_t)}{\sin\theta_{\mathrm{Bx}}} \tag{5.3}$$

$$\nu = \frac{(y_o - y_t)}{\tan\theta_{\mathrm{Bx}}} + x_t - x_o \tag{5.4}$$

where θ_{Bx} is the IMF cone angle, (x_t, y_t) is the contact point between the IMF tangent line and the bow shock, while (x_o, y_o) is the observation point. The coordinate μ is the distance along the tangent magnetic field line between the tangent point and the observation point. The coordinate ν is the distance along the $\hat{\mathbf{x}}_{\mathrm{gse}}$ direction between the tangent magnetic field line and the observation point. In this sense, the coordinate ν indicates how far downstream from the IMF tangent line is the UWFB.

5.3 Criteria for UWFB crossings

The ULF wave foreshock boundary (UWFB) is a surface embedded in the foreshock region. The UWFB can be observed only under quasi-stationary IMF conditions. Therefore, we have to consider only those crossings in which the spacecraft was entering or leaving the wave region under steady IMF conditions. For this purpose, we defined two identification criteria: one based on the level of the wave amplitude and another based on the level of rotation of the IMF direction.

Our criterion relies on the amplitude of the waves observed. By definition, the region *downstream* from the UWFB is the one that displays ULF wave activity, while the region *upstream* does not. For each component of the magnetic field ($j = x, y, z$), if the difference between the average values in downstream region ($B_{dw,j}$) and in the zone with no waves ($B_{up,j}$) is smaller than the standard deviation in the wave zone ($\sigma_{dw,j}$), we consider that the spacecraft crossed a stationary UWFB. Figure 5.2 (upper panel) shows an example in which the criterion is fulfilled. If any of the three components did not satisfy this condition, the event was discarded from our analysis, as illustrated by the example in the lower panels of Figure 5.2.

Our second criterion relies on the level of rotation of the IMF direction. We decided to test this criterion, which was discussed by Meziane et al. [2004a], to compare its predictions with ours. Therefore, if we define the angle α as,

$$\cos\alpha \equiv \frac{\mathbf{B}_{up} \cdot \mathbf{B}_{dw}}{B_{up} B_{dw}} \tag{5.5}$$

it is possible to quantitatively analyze the degree of IMF rotation as the spacecraft passes from the upstream to the downstream region. In equation (5.5), $\mathbf{B}_{up}$ ($\mathbf{B}_{dw}$) is the mean magnetic field in the upstream (downstream) region, meanwhile B_{up} (B_{dw}) corresponds to its absolute value. Then, as long as α remains small we are able to investigate the quasi-stationary scenario and consequently the UWFB. In

Figure 5.1, the left panel shows an example of Cluster entering to the wave region with $\alpha = 2° \pm 1°$. In contrast, the right panel shows an example of Cluster leaving the wave region on 2002 March 16 at 1248:17 UT with $\alpha = 24° \pm 1°$.

5.4 Statistical results

5.4.1 Saturn's UWFB

Using the first fifteen months of Cassini's VHM data, we identified a total of 59 beginnings or endings of intervals in which the magnetometer detected ULF waves. Following the selective criterion based on the wave amplitude, we reduced the original data set of 59 crossings to only 21 quasi-stationary crossings of the wave region. The average values for each component of the magnetic field in the wave zone and in the zone with no waves were the mean values of the observations over two hours before (and after) each apparent crossing. We found that this particular time interval is sufficiently long to obtain values representative of the mean magnetic field, because the longest wave periods found are 10 minutes long. In this sense, we are taking into account approximate ten long wave periods.

For these 21 stationary crossings considered in Section 5.3, we have calculated their locations in terms of the coordinate set (μ, ν) described in Section 5.2. At the Earth, the location of the UWFB was found to strongly depend on the IMF cone angle [Greenstadt and Baum, 1986, Andrés et al., 2015a]. For this reason, we analyzed two separate sets of data, one with $\theta_{\mathrm{Bx}} < 45^o$ and the other with $\theta_{\mathrm{Bx}} > 45^o$, i.e. for small and large cone angles. We performed a scatter plot of the 21 UWFB crossings considered. Figure 5.6 shows the cases with $\theta_{Bx} > 45^o$ in black circles and those with $\theta_{Bx} < 45^o$ in gray circles, and the straight line is our best linear fit (black line) for all our crossings. The small cone angle cases (gray

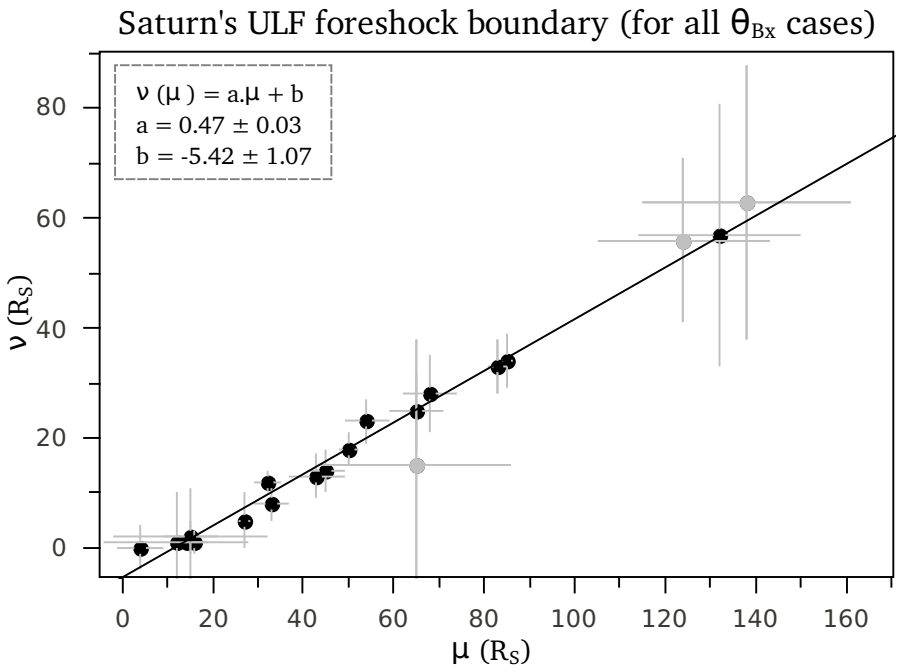

FIGURE 5.6: UWFB for $\theta_{Bx} > 45^o$ (dark circles) and $\theta_{Bx} < 45^o$ (gray squares). If we only consider the $\theta_{Bx} > 45^o$ cases, our best fit yields $\nu(\mu) = a.\mu + b$ ($a = 0.47 \pm 0.04$; $b = -5.65 \pm 1.36$), which is indistinguishable from the best fit displayed in this Figure.

circles) correspond to tangent lines close to the asymptote of the hyperbola ($\theta_\infty = \cos^{-1}(1/e) \approx 18^o$), and therefore have relatively large error bars. However, our best fit considering only the $\theta_{\rm Bx} > 45^o$ cases, yields $\nu(\mu) = a.\mu + b$ ($a = 0.47 \pm 0.04$; $b = -5.39 \pm 1.10$), which is indistinguishable from the result displayed in Figure 5.6.

For each crossing studied, we extend the straight magnetic field line and check for connection to the bow shock fit. If we find that Cassini is connected to the shock by straight magnetic field lines, we identify the intersection point on the bow shock fit and calculate the angle shock angle, θ_{Bn}. As we expect, in all the wave events that we identified we find that the magnetic field line intersects the bow shock fit, i.e. Cassini was in the region magnetically connected to the bow shock. In particular, we find that the increment in wave activity is associated to foreshock regions for which $\theta_{Bn} < 45°$. In fact, 12 out of the 21 crossings have

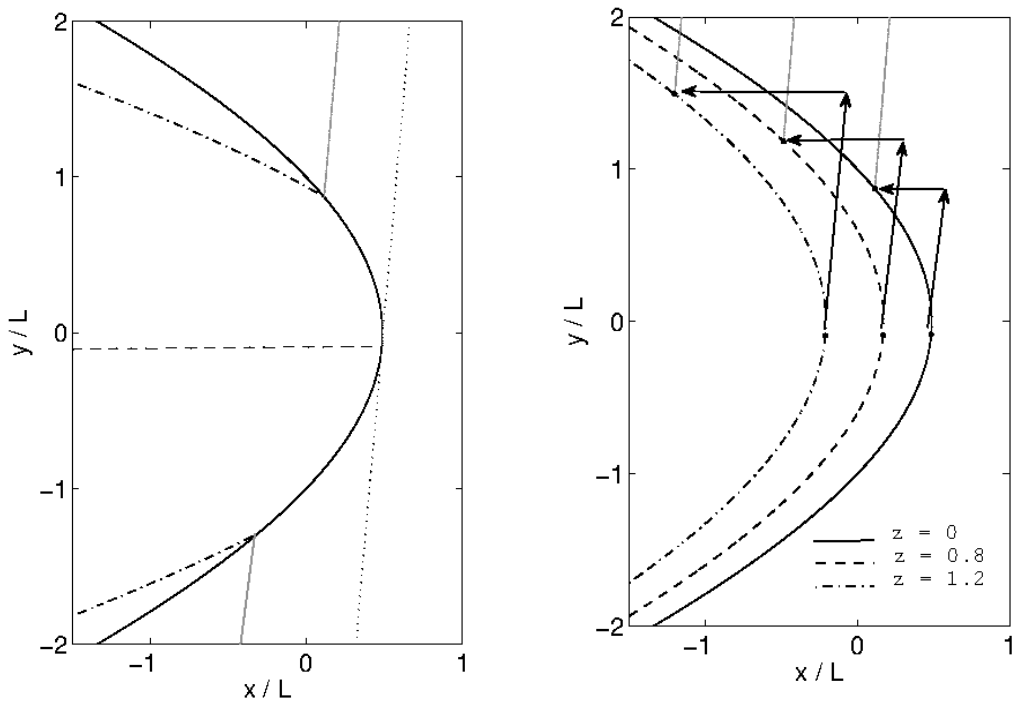

FIGURE 5.7: Left: The curves of $\theta_{Bn} = 45°$ (dot-dashed line) and $\theta_{Bn} = 90°$ (dashed line). In the $\mathbf{v}_{sw}$-$\mathbf{B}$ plane $z = 0$, the average bow shock fit (in units of L), the tangent field line for $\theta_{Bx} = 85°$ (point line), and the magnetic field line corresponding to $\theta_{Bn} = 45°$ (solid line). Right: The (μ,ν) pair for the location of points satisfying $\theta_{Bn} = 45°$ at different (parallel) $\mathbf{v}_{sw}$-$\mathbf{B}$ planes for $\theta_{Bx} = 85°$ and parameter size $L = 51\ R_S$. The distance of each plane to the planet is labeled in units of L.

$\theta_{Bn} = 45° \pm 5°$, while the remaining 9 crossings have θ_{Bn} within the range between 35° and 55°. If we consider the 21 crossings, the average value is $\theta_{Bn} = 42°$ and the standard deviation is $\sigma_{\theta_{Bn}} = 9°$.

It is important to emphasize that $\theta_{Bn} = 45°$ constitutes a natural and conventional separation between quasi-parallel and quasi perpendicular shocks. For a given magnetic field orientation and parameter size, there are two lines on the hyperboloidal shock surface, for which $\theta_{Bn} = 45°$. In Figure 5.7 (left panel) we show a schematic view of the bow shock (in units of L) and the lines corresponding to $\theta_{Bn} = 45°$ (dot-dashed lines) and $\theta_{Bn} = 90°$ (dashed lines), where the field lines are tangent to the hyperboloidal shock. The **x**-**y** plane in Figure 5.7 is parallel to the magnetic field lines and contains the planet in $(x, y) = (0, 0)$. Within this

context, we claim that the set of magnetic field lines that cross the shock on the $\theta_{Bn} = 45°$ curves will determine the UWFB. On other hand, an identification of the UWFB is given by the best fit of crossings on the μ-ν plane [Greenstadt and Baum, 1986].

Therefore, we decided to study the consistency of our linear best fit in the μ-ν plane and the curve corresponding to $\theta_{Bn} = 45°$. Assuming a constant θ_{Bx} (the magnetic field lines lay in the **x**-**y** plane) and parameter size $L = 51\ R_S$, we computed the (μ,ν) pair for the location of the point that satisfies $\theta_{Bn} = 45°$ at different (parallel) $\mathbf{v}_{sw}$-**B** planes (see Figure 5.7, right panel). The corresponding distance of each plane (in units of L) to the planet is labeled. We can clearly see in Figure 5.7 (right panel) an approximate proportionality between the μ-ν coordinates at any given plane. This implies that if Cassini crossed right at the intersection between the bow shock and the $\theta_{Bn} = 45°$ field line, we should expect a straight line passing through the origin in the μ-ν plane (see Figure 5.6). The fact that Cassini crosses that very field line necessarily at a distance from that intersection toward the upstream direction, causes a systematic increase in the value of μ, leaving ν essentially unchanged. The distance from the bow shock measured along field lines range between 0.1 R_S and 17 R_S for the 21 crossings considered. On the one hand, this effect will reduce the quality of the linear fit, and on the other hand it will shift the line on the μ-ν plane to the right (negative intercept), exactly as observed in Figure 5.6. Therefore, we concluded that the appearance of waves tend to occur at θ_{Bn} values of $\sim 45°$. This constant θ_{Bn} loci map on the μ-ν plane as points lying along a straight line. As a result, we find that there is an equivalence between the UWFB determined by $\theta_{Bn} \sim 45^o$ and the best fit in the μ-ν plane [Greenstadt and Baum, 1986]. They are in fact two alternative ways to determine the same spatial region within the foreshock.

According to the specular reflection mechanism described in Section 2.5, the ions

bounce off the shock potential reversing their velocity component along the shock normal $\hat{n}$, while maintaining their component of velocity parallel to the shock's surface. In particular, Schwartz et al. [1983] found that after interacting with the shock, the reflected ions can travel upstream without further interactions with the shock for $\theta_{Bn} < 39.9°$. In the range $39.9° < \theta_{Bn} < 45°$ they found that particles have a positive upstream guiding center motion. However, their gyration motion brings them back to the shock and further interactions occur. For $\theta_{Bn} > 45°$, specularly reflected ions always re-encounter the bow shock with sufficient energy to penetrate into the downstream region. In the absence of Cassini plasma observations (that could confirm the presence of backstreaming ions giving rise to an ion foreshock region), we cannot observationally associate the presence of waves with specific ion distributions. However, if the mechanism of generation of these waves is local, i.e. the wave growth rate γ is sufficiently large, we could think that specular reflection could be a plausible origin for the ions responsible for the waves, since this model discriminates the dynamic properties of particles based on θ_{Bn}. In this case, for quasi-parallel geometries, the reflected ions can go upstream from the bow shock and be detected with ULF wave activity.

5.4.2 The Earth's UWFB

From February 2001 through December 2003, we have identified 192 ULF wave/no-wave transitions. For the purpose of the present study, we find that the optimal time interval to compute mean values of the $\mathbf{B}$, $\mathbf{v}_{sw}$ and n_{sw} lies between three and six wave periods at each side of the boundary, which is sufficiently long to be representative of the mean magnetic field in that region. Figure 5.8 shows a distribution of these transitions with respect to the α angle. As it can be seen, the histogram displays a strong peak at small values of α, in particular for the most frequently value at 5°. The histogram corresponds to a non-symmetric and

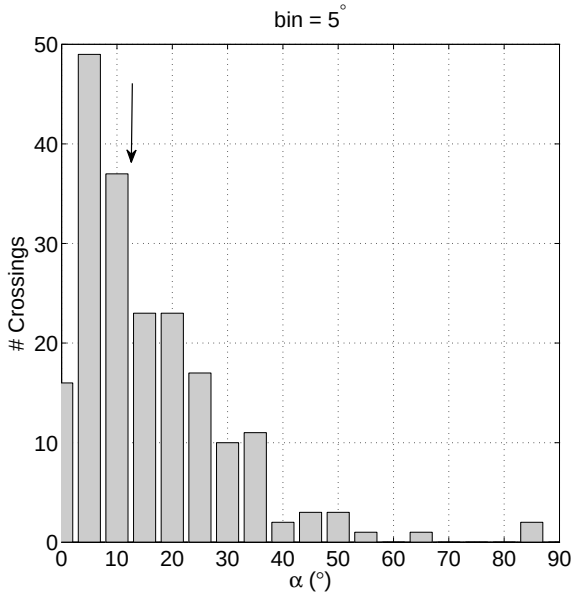

FIGURE 5.8: Histogram of α for the 192 identified crossings. The arrow is located at $\alpha = 12.5°$, which is the upper limit adopted for the stationary UWFB.

positively skewed distribution. Fifty percent of the crossings occur for $\alpha < 12°$ (i.e. 12° corresponds to the median value of the distribution) and 78% of the events occur for angles less than the mean value of 16°. For a better determination of the boundary location, only wave crossings with $\alpha < 12.5°$ (black arrow in Figure 5.8) were considered, which includes 102 events. The UWFB is defined for a given IMF orientation. Following the wave amplitude criterion, we found that 127 of the 192 crossings correspond to quasi-stationary crossings. In this sense, we conclude that the criterion based on the IMF rotation (see Section 5.3) is more restrictive than the criterion based on the wave amplitude.

Figure 5.9 shows the cone angle (θ_{Bx}) distribution corresponding to the 102 quasi-stationary events. There is no indication that boundary crossings occur for a particular IMF direction other than the Parker's prediction, since the distribution is consistent with the IMF spiral orientation at 1 AU.

Results of our statistical survey is performed using 10° bins for the θ_{Bx}. The, Figure 5.10 shows a scatter plot of the UWFB crossings in SFC for two particular

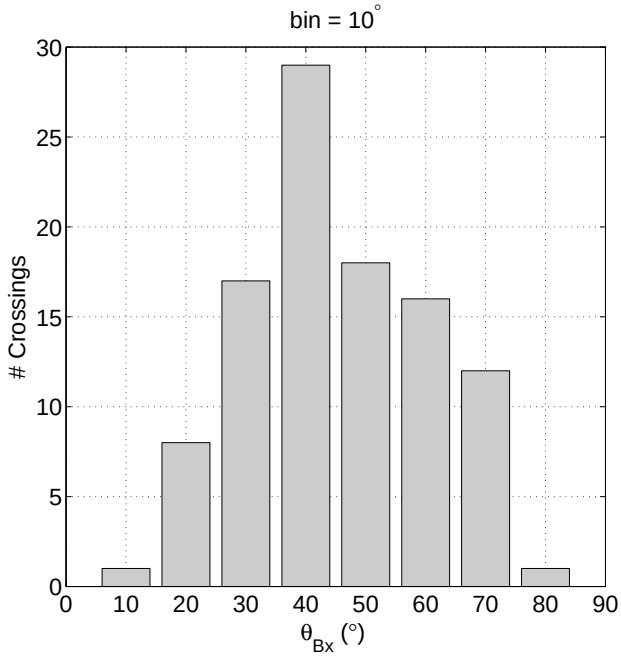

FIGURE 5.9: Histogram of the cone angle θ_{Bx} for the 102 identified crossings with $\alpha < 12.5°$ correspond to the upstream region.

cases: $20° < \theta_{\rm Bx} < 30°$ (in the left panel) and $40° < \theta_{\rm Bx} < 50°$ (in the right panel). In these Figures, the best linear fit corresponds to the blue solid line. The uncertainties in the determination of the three magnetic field components, the three solar wind velocity components and the solar wind density are dominated by the statistical error given by the corresponding standard deviation from the mean values. For the determination of the error bars in Figure 6, we propagated these statistical errors. For reference, we included Meziane and D'Uston [1998] (dashed red line) and Greenstadt and Baum [1986] (dot-dashed line) results. It is worth mentioning the very good agreement between our results and those reported in previous works.

Table 5.1 (upper block) shows the parameters of the μ-ν regression line ($\nu = a\mu + b$) of the UWFB for different θ_{Bx} ranges, using the Farris et al. [1991] bow shock model. For comparison, the results reported by Meziane and D'Uston [1998] and Greenstadt and Baum [1986] also indicated in the lower box. Except for the range $30° < \theta_{\rm Bx} < 40°$, our determination of the slope of the UWFB line is in

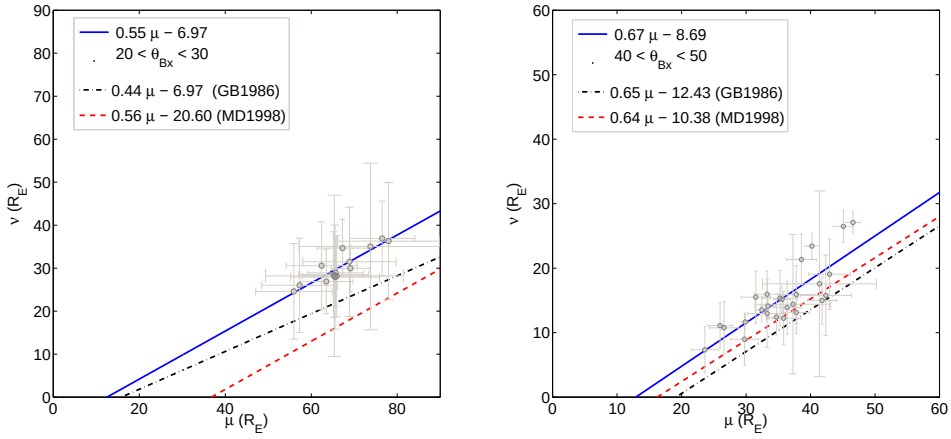

FIGURE 5.10: Best linear fit (solid line) of UWFB crossings in SFC, for cone angles $40° < \theta_{\rm Bx} < 50°$ and $20° < \theta_{\rm Bx} < 30°$. For reference, we included Meziane and D'Uston [1998] (dashed line) and Greenstadt and Baum [1986] (dot-dashed line) results.

TABLE 5.1: Parameters of the μ-ν regression line of the UWFB for different θ_{Bx} ranges, using Farris et al. [1991] bow shock model. The coefficients reported by Meziane and D'Uston [1998] and Greenstadt and Baum [1986] are included for comparison.

θ_{Bx} (°)	a	b	r
20-30	0.56 ± 0.08	-6.97 ± 5.21	0.8937
30-40	0.55 ± 0.08	-6.43 ± 3.66	0.8510
40-50	0.67 ± 0.09	-8.69 ± 3.48	0.8192
50-60	0.77 ± 0.10	-10.40 ± 3.14	0.8737
60-70	0.65 ± 0.24	-5.54 ± 6.05	0.6278

θ_{Bx} (°)	a_{MD}	b_{MD}	a_{GB}	b_{GB}
20-30	0.56 ± 0.02	-20.60 ± 2.45	0.44 ± 0.03	-6.97 ± 3.88
30-40	0.71 ± 0.03	-20.22 ± 1.48	-	-
40-50	0.64 ± 0.02	-10.38 ± 0.68	0.65 ± 0.04	-12.43 ± 1.56
50-60	0.66 ± 0.02	-9.23 ± 0.61	-	-
60-70	0.67 ± 0.03	-8.48 ± 0.64	-	-

good agreement with those obtained by Meziane and D'Uston [1998] (when the errors are taken into account). On the other hand, our results for the range $20° < \theta_{\rm Bx} < 30°$ differ significantly from those reported by Greenstadt and Baum [1986]. Also, based on numerical values listed in Table 5.1, an increase of the UWFB line slope with θ_{Bx} in the SFC plane cannot be ruled out. However, the values of a reported in Meziane and D'Uston [1998] are in general larger than those obtained in the present study. We suspect that the difference is due to the

TABLE 5.2: The η angle between the UWFB and the $\hat{\mathbf{x}}_{\rm gse}$, the P value, the angles θ_{Bn} and θ_{Vn} and the shock normalized velocity in the plasma reference frame P_s. For the calculation of these expressions see Appendix A.

θ_{Bx} (°)	η (°)	P	θ_{Bn} (°)	θ_{Vn} (°)	P_s
20-30	50.66 ± 0.29	1.78 ± 0.49	53 ± 5	28 ± 6	1.46 ± 0.18
30-40	64.86 ± 0.64	1.81 ± 0.41	52 ± 3	18 ± 3	1.54 ± 0.10
40-50	86.99 ± 6.00	1.49 ± 0.21	47 ± 4	4 ± 3	1.46 ± 0.10
50-60	103.50 ± 2.13	1.29 ± 0.88	42 ± 3	14 ± 3	1.30 ± 0.06
60-70	104.10 ± 4.20	1.53 ± 3.50	38 ± 7	27 ± 6	1.13 ± 0.12

TABLE 5.3: Predicted velocities (normalized to the incident solar wind) for the main shock emission mechanisms, i.e. magnetosheath particle leakage, adiabatic reflection and specular reflection.

θ_{Bx} (°)	$(u_\parallel/u_i)_{m.l.}$	$(u_\parallel/u_i)_{a.r.}$	$(u_\parallel/u_i)_{s.r.}$
20-30	1.46 ± 0.18	2.92 ± 0.36	1.06 ± 0.13
30-40	1.54 ± 0.10	3.08 ± 0.20	1.17 ± 0.08
40-50	1.46 ± 0.10	2.92 ± 0.20	1.36 ± 0.10
50-60	1.30 ± 0.06	2.60 ± 0.12	1.44 ± 0.07
60-70	1.13 ± 0.12	2.26 ± 0.24	1.40 ± 0.15

different bow shock models used in these studies. Meziane and D'Uston [1998] used a hyperboloid shape with constant parameters, while in the present work the parameters of the elliptical bow shock are adjusted according to plasma data for each boundary crossing.

We examine the possible connexion between the UWFB properties and the ion emission mechanisms at the shock discussed in section 2.5. In Appendix A we show that the normalized velocity P (in the plasma frame) of an ion propagating along the UWFB is directly related to the slope of the boundary. The third column in Table 5.2 lists the numerical values of the normalized velocity P. This last value is compared to the normalized shock speed $P_s \equiv \cos(\theta_{Vn})/\cos(\theta_{Bn})$ given in the last column of Table 5.2. The first column in Table 5.2 shows the η angle between the UWFB and the $\mathbf{x}_{gse}$.

On the other hand, Table 5.3 summarizes the numerical values for each emission mechanism for each interval in θ_{Bx}. Table 5.3 clearly indicates that the ions

propagating along the boundary are fast enough to escape upstream ($P \geq P_s$ for all θ_{Bx} values). The numerical values of P and P_s also indicate that the observations are in very good agreement with the magnetosheath leakage model only for $\theta_{Bx} = 45°$ and $\theta_{Bx} = 55°$ cases. On the other hand, the specular reflection model seems to be inadequate model. This strongly suggests that backstreaming gyrating ion distributions resulting from specular reflection are not likely a source for wave excitation, a result which is consistent with previous studies [Mazelle et al., 2003]. Finally, the boundary velocity P is underestimated compared to the one obtained from the hypothesis of adiabatic reflection.

5.5 Discussion

Using a well defined, accurate and robust criterion we present a new determination of the boundary for ULF waves in the Earth's and Saturn's foreshocks. All the wave events reported in the present Chapter show evidence of magnetic connectivity to the corresponding bow shock, respectively. This is a clear indication that these waves are associated with the foreshock.

Using Cassini's data from June 2004 through August 2005, we conducted a detailed survey and analysis of ULF waves upstream from Saturn's bow shock. According to their frequencies, we observe two different types of oscillations. Waves with frequencies below Ω_{ci} are the most frequently observed, they are phase steepened with periods of the order of 5 to 10 minutes in the spacecraft frame. The angle between the minimum variance vector and the mean magnetic field suggests that the propagation of these waves is quasi-parallel. The magnetic field rotation around the minimum variance direction is left-handed with respect to the IMF direction. As it is discussed in Bertucci et al. [2007], these signatures suggest that these waves are ion/ion resonant right-hand (fast magnetosonic) mode waves. This is

also compatible with the destabilization of our whistler branch, according to our three-fluid description (see Section 2.4). We also observe waves with frequencies above Ω_{ci}, which are either quasi-monochromatic or steepened, with periods of the order of 60 s (significantly lower than the local proton cyclotron period $T_{ci} \sim 300$ s). At the Earth's foreshock, there is a particular type of ULF waves, the so-called 30 s (period) waves which are quasi-monochromatic [e.g. Le and Russell, 1992]. This kind of waves are found always near to the ULF wave foreshock boundary. In our study we did not find quasi-monochromatic waves next to the Saturnian ULF wave foreshock boundary. A more detailed statistical study might shed some light about the nature of this second group of waves and whether they are the Saturnian equivalent of the 30 s modes found at the Earth's foreshock.

One one hand, we identified 21 stationary crossings inbound (and outbound) from the Saturn's ULF wave foreshock region. We calculated their solar foreshock coordinates in the $\mathbf{v}_{sw}$-$\mathbf{B}$ plane and for the first time we have identified Saturn's ULF wave foreshock boundary. In the μ-ν plane we do not find a clear dependence between the foreshock boundary and the IMF cone angle. We also found that the presence of waves is associated with the change in θ_{Bn} to quasi-parallel geometries. Moreover, we find that our determination of the ULF wave foreshock boundary as the surface given by $\theta_{Bn} = 45°$, is indeed consistent with the linear fit in the μ-ν plane, first proposed by Greenstadt and Baum [1986] for the Earth's ULF wave foreshock.

On the other hand, we have identified 192 ULF wave/no-wave transitions at the Earth's foreshock. For a correct determination of the UWFB, only wave crossings with $\alpha < 12.5°$ were considered, which includes 102 events. We do not find any indication that boundary crossings occur for a particular IMF direction other than the Parker's prediction. Table 5.1 shows the parameters of the μ-ν regression line of the Earth's UWFB for different θ_{Bx} ranges. Except for the range $30° < \theta_{Bx} < 40°$,

our determination of the slope of the UWFB line is in good agreement with those obtained by Meziane and D'Uston [1998] (within the error bars of both studies). Also, based on numerical values listed in Table 5.1, an increase of the UWFB line slope with θ_{Bx} in the SFC plane cannot be ruled out. However, the values of a (slope in the best linear fit) reported in MD98 are in general larger than those obtained in the present study. We suspect that the difference is due to the different bow shock models used in these studies. MD98 used a hyperboloidal shape with constant parameters, while in the present work the parameters of the elliptical bow shock are adjusted according to plasma data for each boundary crossing.

Theoretical investigations on the ULF foreshock boundary are noticeably few. To the best of our knowledge, Skadron et al. [1988] reports the only self-consistent spatio-temporal study involving the interaction between energetic protons backstreaming pre-existing and hydromagnetic waves in the Earth's ion foreshock. Using a parabolic fit to the bow shock, they found the boundary for the region of compressional waves (corresponding to different IMF orientations) using a criterion based on the compressional component of the magnetic fluctuations. In this regard, for $\theta_{\mathrm{Bx}} = 45°$ the Earth's UWFB forms an angle of $87° \pm 6°$ with respect to the $\hat{\mathbf{x}}_{\mathrm{GSE}}$. The observed UWFB is located downstream to the predicted theoretical boundary (78°), in agreement with the theoretical prediction [Skadron et al., 1988]. We speculate that this difference might be due to the fact that Skadron's criterion is based on the compressive component of the fluctuations, where the amplitude of the waves may be smaller than the ones that we observe.

We examined the speed of ions propagating along the different UWFB and compared the obtained results with the known particle acceleration mechanisms (see Section 2.5). We find that the specularly reflected ions fail to provide the necessary energy for the wave excitation. Moreover, the hypothesis of adiabatic reflection predicts ion speeds that are larger than those associated with the UWFB.

One possible explanation for this behavior is suggested: that the difference may be due to momentum exchange between the incident solar wind population and the backstreaming particles through the wave-particle interaction resulting from a beam-plasma instability [Andrés et al., 2015a]. On the other hand, on Saturn's foreshock we suggest that the specularly reflected ions could be associated with the ULF waves, since their occurrences are also limited to $\theta_{Bn} \lesssim 40°$ [Andrés et al., 2013]. The predominance of different acceleration mechanisms in the different planets is a possibility worth considering. Of course, different acceleration mechanisms will have observable consequences on the physical characteristic of the ULF waves being detected.

5.6 Resumen en castellano

En este Capítulo presentamos los resultados y discusiones referidos a la generación y distribución de ondas ULF en el *foreshock* (pre-choque) de Saturno y la Tierra.

En la sección 5.1, presentamos las observaciones utilizadas en el análisis de datos. Además, presentamos y caracterizamos (en frecuencia y polarización) algunos ejemplos de ondas ULF detectadas por Cassini en la región anterior al choque de Saturno.

En la sección 5.2, presentamos las denominadas coordenadas del foreshock (*solar foreshock coordinates*, SFC). Éstas coordendas son las adecuadas para estudiar la distribución de ondas ULF en foreshocks planetarios, como es el caso de Saturno o la Tierra.

En la sección 5.3, presentamos los dos criterios de selección de cruces de la frontera de ondas ULF (*ULF waves foreshock boundary*, UWFB) utilizados. En particular, el primer criterio está basado en la amplitud del campo magnético al atravesar la frontera, y el segundo está basado en el grado de rotación del campo magnético al atravesar la frontera.

En la sección 5.4, presentamos los principales resultados obtenidos a traves del análisis estadístico realizado en Saturno y la Tierra. Además, estudiamos la relación existente entre los distintos mecánismos de aceleración en el choque y las propiedades de cada UWFB.

Finalmente, en la sección 5.5, presentamos las discusiones y conclusiones del Capítulo.

Chapter 6

Conclusions

Es curioso, pero vivir consiste en construir futuros recuerdos...

El Túnel. Ernesto Sabato.

As discussed in the Introduction, one way to describe the state of space plasmas is the particle description, according to which we give the positions and velocities of all the particles, plus the electric and magnetic fields at each point in space. Nevertheless, the use of this description becomes prohibitive as the number of particles is increased. An alternative description is kinetic theory, which is a statistical approach to describe space plasmas, that takes advantage of the undistinguishability of the plasma particles. In particular, the solutions from the kinetic equations (for instance, the Vlasov equation) provide a full description of the phase-space distribution function at all times. However, it is still computationally very demanding to solve these kinetic equations. On the other hand, the much simpler one-fluid MHD approximation adequately describes phenomena at sufficiently larger temporal and spatial scales. More specifically, one-fluid MHD has been a remarkably successful model to describe interplanetary plasmas, as shown for instance by Parker's model of the solar wind [Parker, 1963], the large-scale

orientation of the IMF [Parker, 1958], or the turbulent nature of the small-scale structure of the solar wind [Belcher and Davis, 1971].

However, over the last decades, the sustained increase in the spatial and temporal resolution of space missions has shown a number of small-scale phenomena that cannot be described within the framework of the one-fluid MHD. In this context, we have investigated three important processes taking place in the interplanetary medium, which require an extension of standard one-fluid approximation. For this task, we adopted a multi-fluid approach, which is somewhat more that one-fluid MHD, but considerably simpler than kinetic theory. One of the drawbacks, however, is that certain kinetic effects, such as Landau damping, are not described within this theoretical framework.

Therefore, using a multi-fluid description, we theoretically described small-scale plasma processes observed in different regions of the interplanetary medium. More specifically, we extended the traditional one-fluid MHD framework and incorporated kinetic effects using a two-fluid or even a three-fluid description. In particular, we studied three important processes where kinetic effects may play a role. More specifically, we focused our attention on the turbulent nature of the solar wind, collisionless magnetic reconnection, and the generation and distribution of ULF waves in planetary foreshocks.

In Chapter 2, we described the theoretical framework to be applied throughout the subsequent Chapters, and summarized some of its properties. In Chapter 3 we numerically described the externally driven turbulent regime of full two-fluid plasmas, and obtained power laws for the magnetic energy spectrum. We also showed that the slopes corresponding to the different spectral regions in the spectrum, are consistent with those observed in the solar wind [Andrés et al., 2014b, Sahraoui et al., 2009]. This full two-fluid MHD model incorporates the Hall effect and electron inertia, thus allowing electrons to acquire a finite kinetic

energy and introducing a new range in the energy spectrum. The breaking points in the spectra occur at new physical scales, namely, the ion inertial length and then the electron inertial length. The new nonlinear terms present in our equations (see equations 3.9 - 3.12), redistribute the energy differently among scales. As a result, we can expect also differences in other aspects of the turbulent flow (intermittency, its overall dynamics or its dissipation) on scales where we can not treat the plasma as a single fluid. In summary, we have taken a first step toward understanding turbulence in a full two-fluid model and leave the path open for further studies on this system.

The numerical results presented in Chapter 4 confirm that we are able to obtain fast magnetic reconnection when the effects of electron inertia are retained. At spatial scales of the order of the length of electron inertia, electrons can no longer be frozen-in to the magnetic field lines [Vasyliunas, 1975]. Therefore, only at this level of description, a change in the topology of the magnetic field lines exclusively due to electron inertia (i.e. including the mass of the electron explicitly) becomes possible. Since our scheme is free from physical or numerical resistivity, for the cases of ideal one-fluid MHD and Hall-MHD, we showed that it is not possible to have magnetic reconnection. In summary, we found that within the framework of a full two-fluid MHD model, finite electron inertia is a necessary physical ingredient to drive a fast reconnection process, even though the reconnection rate is largely insensitive to the numerical value of the mass ratio m_e/m_p [Andrés et al., 2014a]. Even though the fact that electron inertia enables magnetic reconnection is well known, to the extent of our knowledge this is the first time that this feature is confirmed with results from a non-dissipative fluid simulation. Furthermore, we derived a theoretical scaling for the reconnection rate as a function of the Hall parameter, which is confirmed by our numerical results and is also compatible with previous results in the literature [Andrés et al., 2015b, Simakov and Chacón,

2008, Malyshkin, 2010].

As mentioned in Chapter 5, the precise location of planetary UWFB can only be determined under quasi-stationary IMF conditions. The foreshock geometry critically depends on the IMF direction. One possible picture to explain the origin of the foreshock ULF waves assumes a stationary IMF and ion beams generated at the bow shock (by different theoretical particle acceleration mechanisms) and backstreaming along magnetic field lines. It is worth mentioning that it is not possible to theoretically explain this picture from a one-fluid MHD description. Further still, plasma instabilities can only be achieved from a three-fluid MHD description, in which a cold tenuous beam of protons interacts with a much denser background made of protons and massless electrons. Our results are consistent with a scenario in which these backstreaming beam traveling along stationary field lines are the ultimate cause of ULF waves. Once generated, these ULF waves propagate downstream. Within this general framework, we observationally studied the spatial distribution of UWFB under conditions that can be regarded as stationary and related to the theoretical emission mechanisms at the bow shock. On Saturn's foreshock we suggest that the specularly reflected ions could be associated with the ULF waves, since their occurrences are also limited to $\theta_{Bn} \lesssim 40°$ [Andrés et al., 2013]. However, on the Earth's foreshock we found that the specularly reflected ions fail to provide the necessary energy for the wave excitation. This strongly suggests that backstreaming ion distributions resulting from specular reflection are not a likely source for wave excitation, a result which is consistent with previous studies [Mazelle et al., 2003]. Finally, our analysis indicated that the observations are in very good agreement with the magnetosheath leakage model only for $\theta_{Bx} = 45°$ and $\theta_{Bx} = 55°$ cases [Andrés et al., 2015a].

6.1 Resumen en castellano

Usando una descripción de multi-fluidos, describimos teoricamente procesos de pequeña-escala en distintaas regiones del medio interplanetario. En particular, estudiamos tres importantes procesos en los cuales efectos cinéticos podrían jugar cierto rol. Nos concentramos en la naturaleza turbulenta del viento solar, la reconexión magnética no-colisional y la generación y distribución de ondas de ultra-baja frequencia en foreshock planetarios.

En el Capítulo 2, describimos el modelo teórico que aplicamos durante los siguientes Capítulos, y resumimos sus propiedades.

En el Capítulo 3, describimos numericamente el regimen de turbulencia externamente impulsado en un plasma de dos-fluidos, y obtuvimos teoricamente leyes de escala para el espectro de energía magnética. También, mostramos que las pendientes halladas corresponden con distintas regiones en el espectro, las cuales son consistentes con las observadas en el viento solar [Andrés et al., 2014b, Sahraoui et al., 2009]. Este modelo de dos-fluidos MHD incorpora el efecto Hall y la inercia de electrones, permitiendo que los electrones adquieran energía cinética y puedan introducir nuevos rangos en el espectro de enrgía. Los puntos de quiebre ocurren a nuevas escalas caracteristicas del modelo llamadas, *ion inertial length* y *electron inertial length*. Los nuevos térmimos no-lineales en las ecuaciones (ver ecuaciones 3.9 - 3.12), redistribuyen la energía entre las distintas escalas. Como resultado, podemos esperar diferencias en el flujo turbulento, intermitencia y la dinámica general del flujo, en regiones donde al plasma no lo podemos considerar como un fluido. En resumen, hemos dado el primer paso hacia el entendimiento de la turbulencia en el modelo de dos-fluidos y hemos dejado abierto el camino para más estudios sobre este sistema.

Los resultados numéricos presentados en el Capítulo 4 muestran que es posible obtener reconexión magnética rápida cuando los efectos de inercia electrónica son tenidos en cuenta. A escalas espaciales del orden del *electon inertial length*, los electrones no viajan más congelados a la líneas de campo magnético. Entonces, solo a este nivel de descripción, un cambio en la topología de las líneas de campo magnético debido a la inercia de los electrones es posible. Ya que nuestro esquema está libre de resistividad numérica espuria, mostramos que en los casos de un fluido ideal MHD y Hall-MHD, la reconexión no es posible. En resumen, encontramos que en el modelo de dos-fluidos MHD, la inercia electrónica es un condimento necesario para impulsar la reconexión magnética rápida, aunque la tasa de reconexión no dependa explicitamente del valor de m_e/m_i [Andrés et al., 2014a]. Pese al hecho de que la inercia electrónica permite la reconexión magnética, hasta donde sabemos esta es la primera vez que se confirma con simulaciones libres de disipación numérica. Más aún, hemos derivado teoricamente un escaleo para la tasa de reconexión, la cual fue confirmada por nuestros resultados numéricos [Andrés et al., 2015b, Simakov and Chacón, 2008, Malyshkin, 2010].

Como mencionamos en el Capítulo 5, la posición de la frontera de ondas puede ser determinada sólo bajo campos magnéticos estacionarios. La geometría del foreshock depende criticamente de la dirección del campo magnético interplanetario (IMF). La imagen clásica del origen de las ondas ULF en el foreshock asume un IMF estacionario y un haz de iones generado en el choque (por distintos mecánismo de aceleración) que viaja en dirección contraria al viento solar incidente a lo largo de las líneas de el IMF. Es importante remarcar que no es posible obtener esta esquema a través de una descripción de un-fluido MHD. Más aún, inestabilidades de plasma sólo pueden emerger en una descripción de tres-fluidos, en la cual un haz frío de protones viaja en un medios mucho más denso de protones y electrones (sin masa). Nuestros resultados son consistentes con este escenario. Dentro de este

marco, estudiamos observacionalmente la distribución espacial de la frontera de ondas bajo condiciones estacionarias. Además, estudiamos la relación entre esta frontera y los distintos mecánismos de aceleración en el choque. En el foreshock de Saturno, encontramos que la reflexión especular de iones podría estar asociada con la frontera de las ondas, ya que este proceso esta limitado a choques paralelos $\theta_{Bn} \lesssim 40°$ [Andrés et al., 2013]. En el caso de la Tierra, nuestros resultados muestran que el proceso favorecido es el *magnetosheath leakage model* para ángulos $\theta_{Bx} = 45°$ y $\theta_{Bx} = 55°$ [Andrés et al., 2015a].

Appendix A

Particle parallel velocity P

The guiding center velocity $\mathbf{u}_{gc}$ in the spacecraft frame is the sum of its velocity parallel to the magnetic field $\mathbf{u}_{\parallel}$ and the convection (or drift) velocity $\mathbf{u}_D$, where, $u_D = u_i \sin\theta_{Bx}$ and $u_{\parallel} = P_{iB} u_i$ (P_{iB} is a multiplicative factor and θ_{Bx} is the cone angle, see Figure A.1). We can also express the guiding center velocity modulus as $u_{gc} = P_{gc} u_i$. Since,

$$|\mathbf{u}_{gc}| = |\mathbf{u}_{\parallel} + \mathbf{u}_D| \tag{A.1}$$

we deduce that

$$P_{gc}^2 = P_{iB}^2 + \sin^2\theta_{Bx} \tag{A.2}$$

From Figure A.1, the guiding center velocity $\mathbf{u}_{gc}$ of a backstreaming particle in the upstream region of the foreshock in the spacecraft frame is

$$\mathbf{u}_{gc} = P u_i \mathbf{b} + \mathbf{u}_i \tag{A.3}$$

where $P u_i$ is the particle parallel velocity in the solar wind frame, $\mathbf{b} = \mathbf{B}/B$ and $\mathbf{u}_i$ is the incident solar wind velocity. Multiplying (A.3) by $\mathbf{b}$, it is straightforward to show

$$P = P_{iB} + \cos\theta_{Bx} \tag{A.4}$$

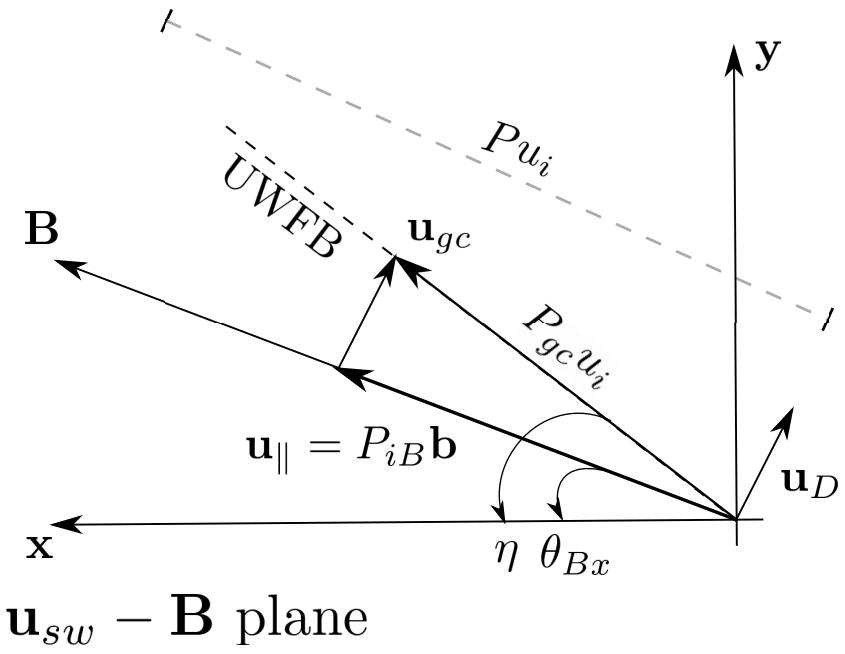

FIGURE A.1: Schematic decomposition of the guiding center velocity $\mathbf{u}_{gc}$ of a backstreaming particle in the foreshock.

Combining equations (A.2) and (A.5) we obtain

$$P_{gc}^2 = 1 + P - 2P\cos\theta_{Bx} \tag{A.5}$$

On the other hand, from Figure A.1 we see that

$$\tan(\eta - \theta_{Bx}) = |\mathbf{u}_D|/|\mathbf{u}_{\parallel}| = \sin\theta_{Bx}/P_{iB}. \tag{A.6}$$

Using trigonometric identities we obtain

$$\tan\eta = \frac{P\sin\theta_{Bx}}{P\cos\theta_{Bx} - 1} \tag{A.7}$$

where η is the slope of the UWFB in the $\mathbf{u}_{sw}$-$\mathbf{B}$ plane. Using the SFC (5.3) we can show that

$$\tan\eta = \frac{\sin\theta_{Bx}}{\cos\theta_{Bx} - p} \tag{A.8}$$

where p is the slope of the UWFB in the μ-ν plane. Finally, from combining equations (A.7) and A.9 we can obtain the normalized velocity for an hypothetic ion which travel along the UWFB

$$P = \frac{\tan\eta}{\tan\eta\cos\theta_{Bx} - \sin\theta_{Bx}}. \tag{A.9}$$

Note that $\tan\eta$ can be obtained from the observations.

Appendix B

Publications related with this Thesis

The main results of this Thesis is a paper published in or submitted to a peer-review journal.

- Chapter 3
  (a) *Energy power spectra in two-fluid turbulence including electron inertia.*
  Andrés, N., Gonzalez, C., Martin, L. N., Dmitruk, P. and Gómez, D. O., Physics of Plasmas, 21, 122305 (2014).

- Chapter 4
  (b) *The influence of the Hall effect and electron inertia in collisionless magnetic reconnection.*
  Andrés, N., Dmitruk P. and Gómez, D. O., Physics of Plasmas (submitted).
  (c) *Effects of electron inertia in collisionless magnetic reconnection.*
  Andrés, N., Martin, L. N., Dmitruk, P. and Gómez, D. O., Physics of Plasmas, 21, 072904 (2014).

- Chapter 5
  (d) *The ULF wave foreshock boundary: Cluster observations.*
  Andrés, N., Meziane, K., Mazelle, C. X., Bertucci, C. and Gómez, D. O., Journal of Geophysical Research, Vol. 120, 4181-4193 (2014).
  (e) *Saturn's ULF wave foreshock boundary: Cassini observations.*
  Andrés, N., Gómez, D. O., Bertucci, C., Mazelle C. X. and Dougherty, M. K., Planetary and Space Science, Vol. 79-80, 64-75 (2013).

References

Alexandrova, O., Saur, J., Lacombe, C., Mangeney, A., Mitchell, J., Schwartz, S. J., and Robert, P. *Phys. Rev. Lett.*, 103:165003, 2009.

Andrés, N., Gómez, D. O., Bertucci, C., Mazelle, C., and Dougherty, M. K. *Planetary and Space Science*, 79-80(0):64–75, 2013.

Andrés, N., Martin, L. N., Dmitruk, P., and Gómez, D. O. *Phys. Plasmas*, 21: 072904, 2014a.

Andrés, N., Gonzalez, C., Martin, L. N., Dmitruk, P., and Gómez, D. O. *Phys. Plasmas*, 21:122305, 2014b.

Andrés, N., Dmitruk, P., and Gómez, D. O. *submitted to Phys. Plasmas*, 2015b.

Andrés, N., Meziane, K., Mazelle, C., Bertucci, C., and Gómez, D. *J. Geophys. Res.*, 00:1–13, 2015a.

Balogh, A., Dunlop, M. W., Cowley, S. W. H., Southwood, D. J., Thomlinson, J. G., Glassmeier, K. H., Musmann, G., Lühr, H., Buchert, S., Acuña, M. H., Fairfield, D. H., Slavin, J. A., Riedler, W., Schwingenschuh, K., and Kivelson, M. G. *Space Sci Rev*, 79:65–91, 1997.

Belcher, J. W. and Davis, L. *J. Geophys. Res.*, 76:3534, 1971.

Bertucci, C., Achilleos, N., Mazelle, C., Hospodarsky, G. B., Thomsen, M., Dougherty, M. K., and Kurth, W. *J. Geophys. Res.*, 112(A09):219, 2007.

Bhattacharjee, A. *Annual Review of Astronomy and Astrophysics*, 42(1):365–384, 2004.

Binsack, J. H. and Vasyliunas, V. M. *J. Geophys. Res.*, 73:429, 1968.

Birn, J., Shay, J. F. D. M. A., Hesse, N. R. E. D. M., Kuznetsova, M., Ma, Z. W., Bhattacharjee, A., Otto, A., and Pritchett, P. L. *Journal of Geophysical Research*, 106:3715–3719, 2001.

Biskamp, D. *Physics of Fluids*, 29(5):1520–1531, 1986.

Biskamp, D. *Magnetic Reconnection in Plasmas*. Cambridge Univ. Press, 2000.

Biskamp, D., Schwarz, E., and Drake, J. F. *Phys. Plasmas*, 4(4):1002, 1997.

Biskamp, D., Schwarz, E., Zeiler, A., Celani, A., and Drake, J. F. *Phys. Plasmas*, 6:751, 1999.

Braginskii, S. *Rev. Plasma Phys.*, 1:205, 1965.

Bruno, R. and Carbone, V. *Living Rev. Solar Phys.*, 10:2, 2013.

Chacón, L., Simakov, A. N., and Zocco, A. *Phys. Rev. Lett.*, 99:235001, Dec 2007.

de Hoffman, F. and Teller, E. *Phys. Rev.*, 80:692–703, 1950.

Dougherty, M. K., Kellock, S., Southwood, D. J., Balogh, A., Smith, E. J., Tsurutani, B. T., Gerlach, B., Glassmeier, K. H., Gleim, F., Russell, C. T., Erdos, G., Neubauer, F. M., and Cowley, S. W. H. *Space Sci Rev.*, 114:331–383, 2004.

Dungey, J. *Reconnection of Magnetic Fields: Magnetohydrodynamics and Collisionless Theory and Observations*. Cambridge University Press, Cambridge, 2000.

Dungey, J. W. *Phys. Rev. Lett.*, 6:47, 1961.

Eastwood, J. P., Balogh, A., Lucek, E. A., Mazelle, C., and Dandouras, I. *Ann. Geophys.*, 21:1457–1465, 2003.

Eastwood, J. P., Lucek, E. A., Mazelle, C., Meziane, K., Narita, Y., Pickett, J., and Treumann, R. A. *Space Sci Rev.*, 118:41–94, 2005.

Edmiston, J. P., Kennel, C. F., and Eichler, D. *Geophys. Res. Lett.*, 9:531–534, May 1982.

Edwards, A. W., Campbell, D. J., Engelhardt, W. W., Fahrbach, H. U., Gill, R. D., Granetz, R. S., Tsuji, S., Tubbing, B. J. D., Weller, A., Wesson, J., and Zasche, D. *Phys. Rev. Lett.*, 57:210–213, Jul 1986.

Farris, M. H., Petrinec, S. M., and Russell, C. T. *Geophysical Research Letters*, 18(10):1821–1824, 1991.

Frisch, U. *Turbulence: The Legacy of A. N. Kolmogorov*. Cambridge Univ. Press, 1995.

Fujimoto, K. *Physics of Plasmas (1994-present)*, 18(11):–, 2011.

Fujisawa, A., Itoh, K., Shimizu, A., Nakano, H., Ohshima, S., Iguchi, H., Matsuoka, K., Okamura, S., Minami, T., Yoshimura, Y., Nagaoka, K., Ida, K., Toi, K., Takahashi, C., Kojima, M., Nishimura, S., Isobe, M., Suzuki, C., Akiyama, T., Nagashima, Y., Itoh, S.-I., and Diamond, P. H. *Phys. Rev. Lett.*, 98:165001, Apr 2007.

Fuselier, S. A., Gurnett, D. A., and Fitzenreiter, R. J. *J. Geophys. Res.*, 90(3935), 1985.

Galtier, S. J. *Phys. Plasma*, 72:721, 2006.

Gary, S. P. *Theory of Plasma Microestabilities*. Cambridge Univ. Press, New York, 1993.

Ghosh, S., Siregar, E., Roberts, D. A., and Goldstein, M. L. *J. Geophys. Res.*, 101 (A2):2493–2504, 1996.

Goldstein, M. L., Roberts, D. A., and Fitch, C. A. *J. Geophys. Res.*, 99:11519, 1994.

Gómez, D. O., Mahajan, S. M., and Dmitruk, P. *Physics of Plasmas*, 15(10): 102303, October 2008.

Greenstadt, E. and Baum, L. *J. Geophys. Res.*, 91(A08):9001–9006, 1986.

Jackson, J. D. *Classical Electrdynamics*. John Wiley & Sons, Inc., 1999.

Kivelson, M. G. and Russell, C. T. *Introduction to Space Physics*. Cambridge Univ. Press, 1995.

Kolmogorov, A. *Akademiia Nauk SSSR Doklady*, 30:301, 1941.

Krishan, V. and Mahajan, S. M. *J. Geophys. Res.*, 109:A11105, 2004.

Le, G. and Russell, C. T. *Planet. Space. Sci.*, 40(9):1215–1225, 1992.

Leamon, R. J., Smith, C. W., Ness, N. F., Matthaeus, W. H., and Wong, H. K. *J. Geophys. Res.*, 103:4775, 1998.

Leamon, R. J., Matthaeus, W. H., Smith, C. W., Zank, G. P., Mullan, D. J., and Ougthton, S. *ApJ*, 537:1054, 2000.

Malyshkin, L. M. *Phys. Rev. Lett.*, 101:225001, 2008.

Malyshkin, L. M. *Phys. Rev. Lett.*, 103:235004, 2009.

Malyshkin, L. M. *Phys. Scr.*, T142:8, 2010.

Masters, A., Achilleos, N., Dougherty, M. K., Slavin, J. A., Hospodarsky, G. B., Arridge, C. S., and Coates, A. J. *J. Geophys. Res.*, 113,(A10):210, 2008.

Matthaeus, W. and Goldstein, M. L. *J. Geophys. Res.*, 87:6011, 1982.

Mazelle, C., Meziane, K., Le Quéau, D., Wilber, M., Eastwood, J. P., Rème, H., Sauvaud, J. A., Bosqued, J. M., Dandouras, I., McCarthy, M., Kistler, L. M., Klecker, B., Korth, A., Bavassano-Cattaneo, M. B., Pallocchia, G., Lundin, R., and Balogh, A. *Planet. Space Sci.*, 51:785–795, 2003.

Merka, J., Szabo, A., Slavin, J. A., and Peredo, M. *Journal of Geophysical Research (Space Physics)*, 110:A04202, April 2005.

Meziane, K. and D'Uston, C. *Annales Geophysicae*, 16:125–133, feb 1998.

Meziane, K., Mazelle, C., Wilber, M., LeQuéau, D., Eastwood, J. P., Rème, H., Dandouras, I., Sauvaud, J. A., Bosqued, J. M., Parks, G. K., Kistler, L. M., McCarthy, M., Klecker, B., Korth, A., Bavassano-Cattaneo, M.-B., Lundin, R., and Balogh, A. *Annales Geophysicae*, 22:2325–2335, 2004a.

Morales, L. F., Dasso, S., Gómez, D. O., and Mininni, P. *Journal of Atmospheric and Solar-Terrestrial Physics*, 67:1821–1826, December 2005.

Morales, L. F., Dasso, S., Gómez, D. O., and Mininni, P. D. *Advances in Space Research*, 37:1287–1291, 2006.

Narita, Y., Glassmeier, K. H., Schaffer, S., Motschmann, U., Sauer, K., Dandouras, I., Formacon, K. H., Georgescu, E., and H., R. 30:1710, 2003.

Øieroset, M., Phan, T. D., Fujimoto, M., Lin, R. P., and Lepping, R. P. *Nature*, 412:414–417, 2007.

Parker, E. *Phys. Fluids*, 1:171–189, 1958.

Parker, E. N. *J. Geophys. Res.*, 62:509–520, December 1957.

Parker, E. N. *Astrophys. J.*, 128:664, 1958.

Parker, E. N. *Interplanetary Dynamical Processes*. New York: Wiley-Inter-science, 1963.

Petschek, H. E. *NASA Special Publication*, 50:425, 1964.

Priest, E. and Forbes, T. *Magnetic Reconnection, MHD Theory and Applications*. Cambridge Univ. Press, 2000.

Rème, H., Aoustin, C., Bosqued, J. M., Dandouras, I., Lavraud, B., Sauvaud, J. A., Barthe, A., Bouyssou, J., Camus, T., Coeur-Joly, O., Cros, A., Cuvilo, J., Ducay, F., Garbarowitz, Y., Medale, J. L., Penou, E., Perrier, H., Romefort, D., Rouzaud, J., Vallat, C., Alcaydé, D., Jacquey, C., Mazelle, C., D'Uston, C., Möbius, E., Kistler, L. M., Crocker, K., Granoff, M., Mouikis, C., Popecki, M., Vosbury, M., Klecker, B., Hovestadt, D., Kucharek, H., Kuenneth, E., Paschmann, G., Schöler, M., Sckopke, N., Seidenschwang, E., Carlson, C. W., Curtis, D. W., Ingraham, C., Lin, R. P., McFadden, J. P., Parks, G. K., Phan, T., Formisano, V., Amata, E., Bavassano-Cattaneo, M. B., Baldetti, P., Bruno, R., Chionchio, G., di Lellis, A., Marcucci, M. F., Pallocchia, G., Korth, A., Daly, P. W., Graeve, B., Rosenbauer, H., Vasyliunas, V., McCarthy, M., Wilber, M., Eliasson, L., Lundin, R., Olsen, S., Shelley, E. G., Fuselier, S., Ghielmetti, A. G., Lennartsson, W., Escoubet, C. P., Balsiger, H., Friedel, R., Cao, J.-B., Kovrazhkin, R. A., Papamastorakis, I., Pellat, R., Scudder, J., and Sonnerup, B. *Annales Geophysicae*, 19:1303–1354, October 2001.

Sahraoui, F., Goldstein, M. L., Robert, P., Yu.,, and Khotyaintsev, V. *Phys. Rev. Lett.*, 102:231102, 2009.

Schwartz, S. J., Thomsen, M. F., and Gosling, J. T. *J. Geophys. Res.*, 88(A03): 2039–2047, 1983.

Shay, M. A., Drake, J. F., and Rogers, B. N. *Geophys. Res. Lett.*, 26:2163–2166, 1991.

Sigsbee, K., Kletzing, C. A., Gurnett, D. A., Pickett, J. S., Balogh, A., and Lucek, E. *Ann. Geophys.*, 22:2337–2344, 2004a.

Sigsbee, K., Kletzing, C. A., Gurnett, D. A., Pickett, J. S., Balogh, A., and Lucek, E. *Geophys. Res. Lett.*, 31(L07):805, 2004b.

Simakov, A. N. and Chacón, L. *Phys. Rev. Lett.*, 101:105003, Sep 2008.

Skadron, G., Holdaway, R. D., and Lee, M. A. *J. Geophys. Res.*, 93:11354–11362, October 1988.

Smith, C. W., Mullan, D. J., Ness, N. F., Skoug, R. M., and Steinberg, J. *J. Geophys. Res.*, 106:18625, 2001.

Smith, D., Ghosh, S., Dmitruk, P., and Matthaeus, W. H. *Geophysical Research Letters*, 31(2):L02805, 2004.

Sonnerup, B. U. O. *J. Geophys. Res.*, 74(5):1301–1304, 1969.

Sonnerup, B. U. O. and Scheible, M. Minimum and Maximum Variance Analysis, in:. pages 185–220. Analysis Methods for Multi-Spacecraft Data. Int. Space Sci. Inst, Bern, Switzerland(Eds), Int. Space Sci. Inst., Bern, Switzerland, 1998. Analysis Methods for Multi-Spacecraft Data.

Sweet, P. A. *The Observatory*, 78:30–32, February 1958.

Tanaka, M., Goodrich, C. C., Winske, D., and Papadopoulos, K. *J. Geophys. Res.*, 88:3046–3054, April 1983.

Taylor, G. I. *Proc. R. Soc. Lond.*, 164 (919):476–490, 1938.

Thomsen, M. F., Schwartz, S. J., and Gosling, J. T. *J. Geophys. Res.*, 88:7843, 1983.

Treumann, R. A. *Astron. Astrophys. Rev.*, 17:409–535, 2009.

Tsurutani, B. T. and Rodriguez, P. *J. Geophys. Res.*, 86(4317), 1981.

Turner, L. *IEEE Trans. Plasma Science*, 14:849, 1986.

Vasyliunas, V. M. *Reviews of Geophysics*, 13(1):303–336, 1975.

Wan, M., Matthaeus, W. H., Karimabadi, H., Roytershteyn, V., Shay, M., Wu, P., Daughton, W., Loring, B., and Chapman, S. C. *Phys. Rev. Lett.*, 109:195001, Nov 2012.

Wang, A., Bhattacharjee, A., and Ma, Z. W. *J. Geophys. Res.*, 105:27633, December 2000.

Wang, A., Bhattacharjee, A., and Ma, Z. W. *Phys. Rev. Lett.*, 87:265003, December 2001.

Yamada, M. *Phys. Plasmas*, 18:111212, 2011.

Zenitani, S., Hesse, M., Klimas, A., Black, C., and Kuznetsova, M. *Phys. Plasmas*, 18(12), 2011.